INVESTIGATION OF ELECTROCHEMICAL INTERFACES FOR THE DEVELOPMENT OF NOVEL ELECTRODES FOR BIOMIMETIC ENERGY CONVERSION AND HYDROGEN FUEL CELLS

By

Christopher James Faulkner

Dissertation

Submitted to the Faculty of the

Graduate School of Vanderbilt University

in partial fulfillment of the requirements for the degree of

DOCTOR OF PHILOSOPHY

in

Chemical Engineering

May, 2010

Nashville, Tennessee

Approved:

G. Kane Jennings

David E. Cliffel

Scott A. Guelcher

Paul E. Laibinis

Bridget R. Rogers

To my wife, Devon, who has been infinitely supportive

ACKNOWLEDGEMENTS

I would first like to thank my advisor, Prof. Kane Jennings, of whom I have the utmost respect. He is a mentor in every sense of the word, and I am appreciative for his oversight of my professional development. It has truly been an honor to work in his lab. I would also like to thank the faculty members that served on my Ph.D. committee: Prof. David Cliffel, Prof. Scott Guelcher, Prof. Paul Laibinis, and Prof. Bridget Rogers. I appreciate each committee member for their insightful discussions that helped make this work more complete.

I would also like to thank my co-workers, Dr. Bradley Berron, Brandon Booth, Peter Ciesielski, Angeline Cione, Juan Carlos Tuberquia, and Steven Vilt for their helpful discussions and willingness to lend a hand. I am grateful for my fellow graduate students that have made my experience at Vanderbilt more enjoyable. I am also grateful to the undergraduates that have contributed to this work: Remington Fischer, Fred Hijazi, Andrew Payne, and Alex Trzeciak.

I appreciate Prof. Rogers for the use of the spectroscopic ellipsometer and x-ray photoelectron spectrometer, Prof. Cliffel for the use of the electrochemical workstation, and the Vanderbilt Institute of Nanoscience and Engineering for providing access to many of the instruments used in completing this work.

I thank all my friends and family for their love and support. I would like to extend a special thank you to my parents for the sacrifices they made to help me get here. I would also like to thank the Crigler and Bobo families for their faith in me and for the

special memories they have provided during my time in Tennessee. I would like to thank Fairlane Church for being such a loving and encouraging church family.

I am most grateful for my wife as she has given me infinite support as I pursue my career goals. I thank her for her care, patience, and understanding throughout my time at Vanderbilt, and I look forward to our future together.

I am appreciative of the funding agencies that made this project possible. This project was funded by in part by the Department of Energy (ER46239) and the National Research Initiative of the USDA Cooperative State Research, Education, and Extension Service (2005-35603-15303). I am also thankful to Vanderbilt University for the awarded scholarship.

TABLE OF CONTENTS

Page

LIST OF TABLES

LIST OF FIGURES

CHAPTER I

INTRODUCTION

Heightened awareness in global warming and an increasing demand in energy consumption, projected to be ~40 TW by 2050[1], have generated a surging interest in creating sustainable alternative energy sources. One of the major challenges of incorporating these alternative technologies, such as solar cells and fuel cells, into societal infrastructure is their cost. To reduce the cost of these technologies, either they must be made more efficient or a fundamental rethink of current designs is necessary. Currently, silicon-based photovoltaics have an efficiency of ~20%;[2] however, the expense of their processing has kept photovoltaics from being commercially competitive.[1] Fuel cells are currently limited by improper processing during membrane electrode assembly, where membranes and electrodes are literally pasted together to achieve 2-D interfaces that provide limited contact area for power generation. These shortcomings can also underutilize rare and precious metal catalysts, raising the cost and inefficiency of the fuel cell. An essential component of both of these energy conversion technologies is the interfacial charge transfer from the cells to an external circuit. The research presented herein seeks to address interfacial issues in both a biomimetic solar energy conversion platform and also a 3-D architecture for potential improvements in fuel cell processing and performance and is discussed in two parts: (I) the development of dense, protein films on electrode surfaces for use in biomimetic solar energy conversion

and (II) the bottom-up growth of ionomer films on both 2-D and 3-D electrode architectures for use in proton exchange membrane fuel cells (PEM-FC).

Part I discusses the incorporation of the light harvesting complex, Photosystem I, into electrochemical systems. The Earth is bombarded with ~178,000 TW of solar radiation, providing a huge capacity to meet present and future energy demands.[3] Plants and some bacteria take advantage of this abundant energy source through photosynthesis, Nature's ~90 TW solar energy conversion process.[4] PSI, one of the major protein complexes responsible for photosynthesis, exhibits photodiode properties transferring an electron across the thylakoid membrane upon absorption of a photon with a quantum efficiency of 0.97.[5] For nearly every photon absorbed, PSI produces charge separation within 15 ps, inducing a potential drop of 1.1 V across the membrane.[5] These remarkable properties exhibited by PSI make it a prime candidate for use in biologically inspired solar energy conversion, in both solid-state photo-electrochemical devices and "wet" photo-electrochemical cells.[6-8]

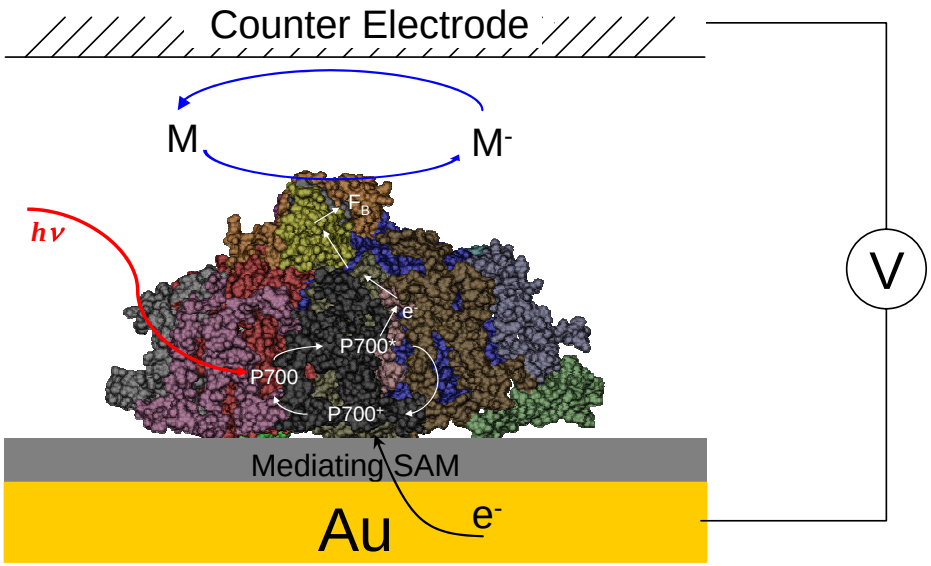

Figure 1.1. Schematic of PSI incorporated into a photoelectrochemcical cell.

To circumvent some of the problems in maintaining PSI in the dry, solid-state environment of a device, we focus here on the incorporation of highly stable PSI, extracted from spinach, into a "wet" photoelectrochemical cell through bottom-up, self-assembly processing. As an example of a "wet" photoelectrochemical cell, Figure 1.1 shows a schematic of PSI oriented near an electrode surface and exposed to a solution that contains a freely diffusing electrochemical mediator. Upon light-induced electron transfer across PSI, the mediator is reduced at the acceptor site of PSI and can then discharge its current at an anode, while the $P700^{+}$ reaction center must draw an electron from the metal electrode (cathode) to enable further photon capture. The advantages of using electrochemical mediators rather than a hard-wired, solid state device are that the process more closely mimics photosynthesis with the mediator exhibiting a parallel function as ferredoxin does in the plant and the protein complex is stable in an aqueous environment. The research proposed herein will focus on PSI assembly into dense monolayer and multilayer films, as well as PSI activity and performance in a photoelectrochemical cell.

In order to effectively incorporate PSI into a solar energy conversion device, PSI must be: 1) isolated from the thylakoid membrane while maintaining its functionality, 2) assembled into dense films at an electrode with general orientation of its electron transfer vector normal to the electrode surface, and 3) interfaced with efficient electron transfer mediators to transfer charged species between PSI and an opposing electrode of the device. Much work has been done in order to isolate PSI from its natural environment without losing its unique properties and functionality[9-12], and our work has built from

those studies. Current methods for incorporating PSI into photovoltaics and electrochemical cells primarily include adsorption of extracted PSI from solution onto self-assembled monolayers (SAMs) atop gold electrodes through physical or electrostatic interactions.[8, 13-18] PSI has also been successfully tethered to a gold electrode through genetic mutation of specific subunits or residues.[6, 7, 19] However, these approaches can be labor intensive and may require many hours to achieve dense PSI layers that are effective in solar energy conversion.

Chapters IV and V discuss the development of PSI/Au electrodes for solar energy conversion. This work developed a simple, fast method to assemble PSI on a surface while maintaining functionality and performance, and these chapters discuss the effects of the attachment scheme on electron transfer at the PSI/Au electrode. In Chapter V, we discuss the expansion of the PSI monolayer assembly process to prepare dense multilayer films of PSI. Further, the enhanced photocurrent observed for a multilayered PSI film over that of a monolayer PSI film is described and discussed.

Part II describes the development of new surface-initiated ionomer films and electrode architectures to enhance performance and efficiency of PEM-FC. The power of a PEM-FC is determined by the reaction of oxygen with protons on Pt catalyst sites. Thus, films that facilitate oxygen and proton transport to the Pt catalyst on the cathode of the fuel cell would improve the performance and lower the cost of current technologies. Current fabrication approaches[20, 21] for proton exchange membrane (PEM) fuel cells are highly empirical and utilize poorly controlled coating and processing methods. As an example of a common integration of catalyst layers within a fuel cell, a microscopically ill-defined mixture of catalyst and ionomer is sprayed or brushed onto a Nafion®

membrane, and the resulting structure is pressed against a carbon cloth.[21] Due to the poor control of this method, a significantly thicker catalyst layer must be prepared to assure complete coating of the membrane, leading to waste of expensive materials. Coupled with the empirical nature of the mixing process, this overly thick catalyst layer will result in poor utilization of catalyst since many catalyst particles are not directly wired to the electron- or proton-conductive elements and are therefore inactive in the electrode reaction.[22] In addition, the haphazard mixing of these processes leads to poor reproducibility and the inability to compare results from different laboratories.

As fuel cell interfaces evolve from nearly 2-D to highly porous, 3-D systems,[23] the ability to grow ionomer from the electrode surface, monomer by monomer, is essential to ensure the appropriate integration of ionomer with electrode/catalyst. Presynthesized bulk ionomer would be restricted from entering small pores, leading to inaccessibility of the expensive catalyst in those pores to the transport of reactants. Here, we employed the surface-initiated ring opening metathesis polymerization of 5-(perfluoro-n-alkyl)norbornenes (NBFn), followed by sulfonation of their olefinic groups,[24] as a route towards ultrathin ionomer coatings to enhance oxygen and proton transport to the "triple interface" as discussed in Chapters VI-IX.

References

1. Lewis, N. S.; Nocera, D. G., Powering the Planet: Chemical Challenges in Solar Energy Utilization. *Proc. Nat. Acad. Sci. USA* **2006,** 103, 15729-15735.

2. Chopra, K. L.; Paulson, P. D.; Dutta, V., Thin-film solar cells: an overview. *Prog. Photovolt: Res. Appl.* **2004,** 12, 69-92.

3. Kruse, O.; Rupprecht, J.; Mussgnug, J. H.; Dismukes, G. C.; Hankamer, B., Photosythesis: a blueprint for solar energy capture and biohydrogen production technologies. *Photochem. Photobiol. Sci.* **2005,** 4, 957-969.

4. Alivisatos, P.; Cummings, P.; Yoreo, J. D.; Fichthorn, K.; Gates, B.; Hwang, R.; Lowndes, D.; Majumdar, A.; Makowski, L.; Michalske, T.; Murray, C.; Sibener, S.; Teague, C.; Williams, E. *Nanoscience Research for Energy Needs: Report of the National Nanotechnology Initiative Grand Challenge Workshop*; 2004.

5. Nelson, N.; Yocum, C. F., Structure and Function of Photosystems I and II. *Annu. Rev. Plant Biol.* **2006,** 57, 521-565.

6. Das, R.; Kiley, P. J.; Segal, M.; Norville, J.; Yu, A. A.; Wang, L.; Trammell, S. A.; Reddick, L. E.; Kumar, R.; Stellacci, F.; Lebedev, N.; Schnur, J.; Bruce, B. D.; Zhang, S.; Baldo, M., Integration of Photosynthetic Protein Molecular Complexes in a Solid-State Electronic Device. *Nano Letters* **2004,** 4, 1079-1083.

7. Frolov, L.; Rosenwaks, Y.; Carmeli, C.; Carmeli, I., Fabrication of a Photoelectric Device by Direct Chemical Binding of Photosynthetic Reaction Center Protein to Metal Surfaces. *Advanced Materials* **2005,** 17, 2434-2437.

8. Lee, I.; Lee, J. W.; Greenbaum, E., Biomolecular electronics: Vectorial arrays of photosynthetic reaction centers. *Phys. Rev. Lett.* **1997,** 79, 3294-3297.

9. Reeves, S. G.; Hall, D. O., Higher plant chloroplasts and grana general preparative procedures excluding high carbon dioxide fixation ability chloroplasts. *Methods in Enzymology* **1980,** 69, 85-94.

10. Shiozawa, J. A.; Alberte, R. S.; Thomber, J. P., P700-chlorophyll a-protein - isolation and some characteristics of complex in higher plants. *Arch. Biochim. Biophys.* **1974,** 165, 388-397.

11. Owens, T. G.; Webb, S. P.; Alberte, R. S.; Mets, L.; Fleming, G. R., Antenna size dependence of fluorescence decay in the core antenna of photosystem-I - etimates of charge separation and energy-transfer rates. *Proc. Nat. Acad. Sci. USA* **1987,** 84, 1532-1536.

12. Lee, J. W.; Zipfel, W.; Owens, T. G., Quenching of chlorophyll excited-states in photosystem-I by quinones - stern-volmer analysis of fluorescence and photochemical yield. *Journal of Luminescence* **1992,** 51, 79-89.

13. Lee, I.; Lee, J. W.; Stubna, A.; Greenbaum, E., Measurement of electrostatic potentials above oriented single photosynthetic reaction centers. *Journal of Physical Chemistry B* **2000,** 104, 2439-2443.

14. Ko, B. S.; Babcock, B.; Jennings, G. K.; Tilden, S. G.; Peterson, R. R.; Cliffel, D., Effect of Surface Composition on the Adsorption of Photosystem I onto Alkanethiolate Self-Assembled Monolayers on Gold. *Langmuir* **2004,** 20, 4033-4038.

15. Ciobanu, M.; Kincaid, H. A.; Lo, V.; Dukes, A. D.; Jennings, G. K.; Cliffel, D. E., Electrochemistry and Photoelectrochemistry of Photosystem I Adsorbed on Hydroxyl-terminated Monolayers. *Journal of Electroanalytical Chemistry* **2007**, 599, 72-78.

16. Munge, B.; Das, S. K.; Ilagan, R.; Pendon, Z.; Yang, J.; Frank, H. A.; Rusling, J. F., Electron Transfer Reactions of Redox Cofactors in Spinach Photosystem I Reaction Center Protein in Lipid Films on Electrodes. *Journal of American Chemical Society* **2003,** 125, 12457-12463.

17. Terasaki, N.; Yamamoto, N.; Hiraga, T.; Sato, I.; Inoue, Y.; Yamada, S., Fabrication of Novel Photosystem I - Gold Nanoparticle Hybrids and their Photocurrent Enhancement. *Thin Solid Films* **2006**, 153-156.

18. Kincaid, H. A.; Niedrinhaus, T.; Ciobanu, M.; Cliffel, D. E.; Jennings, G. K., Entrapment of Photosystem I within Self-Assembled Films. *Langmuir* **2006,** 22, 8114-8120.

19. Carmeli, I.; Frolov, L.; Carmeli, C.; Richter, S., Photovoltaic Activity of Photosystem I - Based Self-Assembled Monolayer. *Journal of American Chemical Society* **2007,** 129, 12352-12353.

20. Carrette, L.; Friedrich, K. A.; Stimming, U., Fuel Cells: Principles, Types, Fuels, and Applications. *ChemPhysChem* **2000,** 1, 162-193.

21. Lister, S.; McLean, G., PEM Fuel Cell Electrodes. *Journal of Power Sources* **2004,** 130, 61-76.

22. Cha, S. Y.; Lee, W. M., Performance of Proton Exchange Membrane Fuel Cell Electrodes Prepared by the Direct Deposition of Ultrathin Platinum on the Membrane Surface. *J. Electrochem. Soc.* **1999,** 146, 4055-4060.

23. Middelman, E., Improved PEM Fuel Cell Electrodes by Controlled Self-Assembly. *Fuel Cells Bulletin* **2002,** November, 9-12.

24. Berron, B. J.; Payne, P. A.; Jennings, G. K., Sulfonation of Surface-Initiated Polynorbornene Films. *Industrial & Engineering Chemistry Research* **2008,** 47, 7707-7714.

CHAPTER II

BACKGROUND

Photosystem I (PSI)

Photosystem I (PSI), a ~500 kDa protein with an ~80 nm^2 footprint, is one of two photosynthetic reaction centers essential in the photosynthesis process found in higher order plants and some bacteria.[1-3] The primary light driven reactions in photosynthesis are catalyzed by four protein complexes: Photosystem II (PSII), cytochrome b_6f, Photosystem I (PSI), and an ATP-synthase (Figure 1).[3, 4] Upon photo-excitation, PSII enables the oxidation of water. The cytochrome complex facilitates proton and electron transfer between PSII and PSI. Upon photo-excitation, PSI reduces ferrodoxin to enable production of NADPH. The ATP-synthase generates ATP. Photosystem I produces the largest potential drop upon absorbing light, and captures 20% more photons than PSII.[5-8] Spinach-derived PSI is considered to be a macromolecule comprised of 16 protein subunits, 2 phylloquinones, 3 Fe_4S_4 clusters, and many chlorophyll light harvesting complexes (the amount of chlorophylls per PSI is dependent upon extraction methods used, usually ~100) (Figure 2.1).[3, 9, 10]

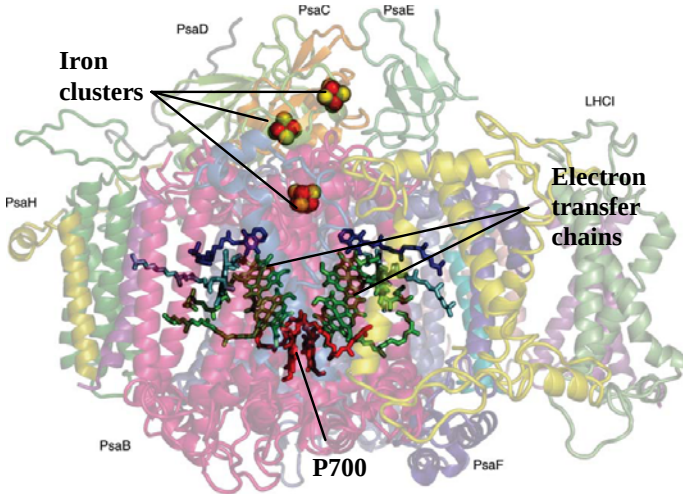

Figure 2.1. Structure of PSI with the P700 reaction center, electron transfer chains, and iron complexes highlighted. This figure has been adapted from Nelson and Yocum.[3]

Upon absorbing photons through light harvesting complexes, PSI generates excited electrons that travel unidirectionally from the reaction center, P700, to the ferredoxin docking sites, F_A/F_B, at the stromal side of the protein using one of two electron pathways. Upon exposure to light PSI behaves as a diode and achieves a 1.1 V potential drop from P700, with an E_o of +440 mV vs. NHE, to the F_A/F_B cofactor, with an E_o of -540 mV vs NHE. In plants and cyanobacteria, the P700 reaction center is reduced by plastocyanin. The quantum efficiency of PSI is near unity and electron transfer occurs in approximately 15 ps.[10, 11]

Self-Assembled Monolayers and PSI Adsorption

Self-assembled monolayers (SAMs) have been utilized effectively in the modification of surfaces in order to immobilize many biological species, including peptides,[12] DNA,[12, 13] proteins,[14-18] and cells.[15-17] In particular, ω-terminated alkyl thiols are widely used because of their commercial availability and the dense 2-D sheet of

surface functionality that results from their assembly. Greenbaum et al. demonstrated that PSI readily adsorbs onto hydroxyl- and carboxyl-terminated SAMs, presumably through hydrogen bonding and electrostatic interactions, respectively.[19, 20] By characterizing their films with scanning tunneling spectroscopy, they were able to distinguish the orientation of the PSI complexes on the SAM surfaces. They report that ~70% of the PSI complexes orient with the electron transfer vector normal to the surface on hydroxyl-terminated SAMs, whereas ~80% of PSI complexes orient parallel to the substrate atop carboxyl-terminated SAMs. Terasaki et al. utilized 3-mercapto-1-propanesulfonic acid SAMs to preferentially attach PSI to gold nanoparticles with the F_B site proximal to the surface,[21] and Rusling et al. investigated bacterial PSI adsorbed onto a polycationic layer atop a thin, negatively charged SAM on gold.[22] Previously, our group has demonstrated that PSI does not adsorb to low energy surfaces from solution.[23] We were able to control PSI adsorption by patterning substrates with high and low energy moieties, such as hydroxyl- and methyl-terminated alkanethiols.[24] However, these methods do not directly attach PSI to the substrate. By taking advantage of a thiol group's affinity for gold, Das et al.[25] and Frolov et al.[26, 27] have mutated PSI subunits to contain cysteine residues that enabled PSI to have a direct linkage to a gold surface. Both groups claim that through the cysteine mutation they are able to control the orientation of PSI complexes on the surface.

The approaches mentioned above are limited due to only a monolayer of PSI being used. In its natural environment, PSI resides within the lipid bylayer of thylakoid stacks located in the chloroplasts of the cell. Since, the thylakoid membranes are in stacks, each plant cell is able to absorb more light. Thus, translating this principle to PSI-

modified electrodes, multiple layers of PSI would be able to convert more light into chemical or electrical energy than monolayer PSI films. Recently, Carmeli and Frolov described a method in which they prepared a multilayer PSI film through layer-by-layer deposition.[28] They mutated PSI to include a cysteine residue to preferentially bind the protein to the electrode surface. Then depositing Pt to the F_B site, they repeated PSI monolayer deposition taking advantage of sulfur's affinity for Pt, creating stacked layers of PSI. This technique is tedious and cumbersome, requiring many steps to create the multilayered protein film. In Chapter V a facile method for the formation of multilayer PSI films will be discussed.

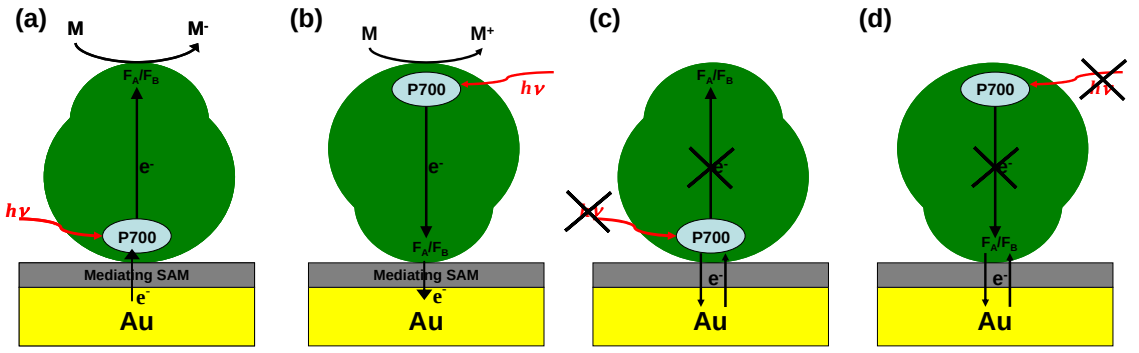

Figure 2.2. The orientation of PSI impacts the type of current produced upon photo-excitation: cathodic (a) or anodic (b). Direct electrochemical measurements of P700 (c) and F_B (d) are possible by inhibiting light exposure.

PSI behaves as a photodiode, such that, upon exposure to light, electrons are transferred unidirectionally across the protein complex from P700 to F_B. Thus, the orientation of PSI affects the type of photo-induced current produced. If the P700 is proximal to the electrode, a cathodic current is produced by electrons transferring from the gold substrate to P700 (Figure 2.2(a)). However, if the F_A/F_B clusters are near the electrode surface, electrons are transferred from F_B to the electrode, producing an anodic

photo-current (Figure 2.2(b)). Random PSI adsorption on an electrode surface would yield little or no net photo-current due to the competing cathodic and anodic currents produced. Therefore, controlled orientation of PSI on the electrode surface is essential in the development of PSI photoelectrochemical cells and devices.

Electron Mediators

In plants, the primary electron mediators that interact with PSI are plastocyanin and ferredoxin. Upon photo-excitation, P700 is excited to $P700^*$ sending an electron across the protein to the iron complexes F_A/F_B, so that P700* becomes $P700^+$. Ferredoxin then oxidizes F_A/F_B. In order to repeat the cycle, plastocyanin must reduce $P700^+$ back to P700. However, artificial redox mediators can be used to reduce and oxidize $P700^+$ and F_A/F_B, respectively. x,y-Dipyridyl salts, such as methyl viologen (MV, E_o = -0.44 V vs NHE) and 2,6 dichloroindophenol (DCIP, E_o = +0.22 V vs. NHE), and low-potential quinones, such as anthraquinone sulfonates (E_o ~ -0.2 V vs. NHE), are able to accept electrons from F_A/F_B.[29] Electron donors of P700 are the reduced form of DCIP ($DCIPH_2$) and sodium ascorbate (NaAs, E_o = +0.06 V vs. NHE); however, other mediators (diaminodurene, phenazine methosulfate, and N,N,N,N-tetramethyl-p-phenylenediamine) can also reduce $P700^+$ if present in high concentrations.[29] We will primarily be using MV, DCIP, $DCIPH_2$, and NaAs as redox mediators (Figure 2.3).

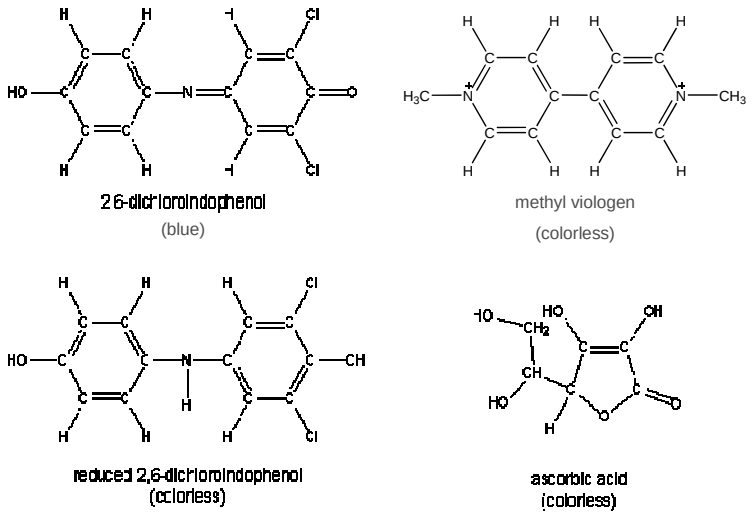

Figure 2.3. Common electron acceptors (top) and donors (bottom) of PSI.

Fuel Cells

Fuel cells are electrochemical cells that capitalize on the oxygen reduction reaction with hydrogen to generate power. Figure 2.4 displays a schematic of a typical proton exchange membrane fuel cell (PEM-FC). In PEM-FCs, the hydrogen source gas is split into electrons and protons at the anode. The electrons flow through an external circuit toward the cathode, whereas the protons are transported to the cathode using an ionomer membrane as electrolyte. The ionomer doubles as a barrier to the feed gases between the electrodes. The electrochemical circuit is completed at the catalyst-coated cathode where the protons combine with oxygen and electrons to form water. The efficiency of a PEM-FC is dependent on the integration of the ionomer membranes, feed gases, and catalysts sites, also known as the “three-phase” interface in a FC.

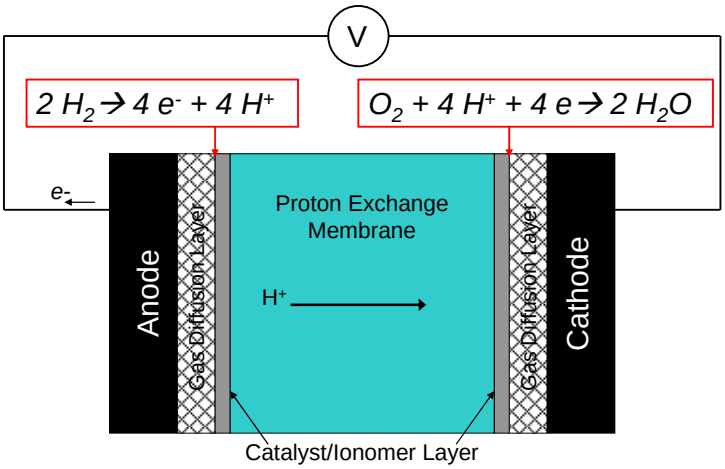

Figure 2.4. Schematic of a typical proton exchange membrane assembly.

Current PEMs are generally doped with either sulfonate or phosphonic acid groups to promote proton transport to the cathode of a FC. Nafion 117, a perfluorosulfonate polymer created by Du Pont, is the predominant ionomer studied due to its chemical, mechanical, and thermal stability and high proton conductivity at moderate temperatures, ~80° C. The proton conductivity of these polymers increases with the degree of sulfonation. However, Nafion membranes suffer from degradation in mechanical stability at sulfonation levels > 60% and complete solubility in water at levels > 80%. To circumvent these issues, more rigid and mechanically robust ionomer membranes are being investigated. In particular, polybenzimidazole-based PEMs are being developed as the cyclic structures that comprise the back-bone of the ionomer are stiff and introduce mechanical stability.[30] This class of ionomers is more thermally stable than Nafion and is applicable to higher temperature FCs that operate from 150° – 200° C.[30]

Chapters VI-IX discuss the development of novel cathode interfaces by designing a new ionomer film to facilitate the ORR on planar and porous supports. The ionomer materials introduced here are comprised of a series of sulfonated poly(perfluoro-n-

alkyl)norbornenes, structure shown in Figure 2.5. In general, polynorbornenes exhibit excellent thermal and chemical stability,[31] and the asymmetry of the structure proposed here, considering the hydrophobicity of the fluorocarbon sidechain, should promote self-organization to promote formation of a hydrophobic matrix for good gas transport along with SO_3^- lined channels for proton transport. A notable advantage of these polynorbornenes is that they can be grown from surfaces at low temperature using a controlled ring-opening metathesis polymerization (ROMP) to produce well-defined thin films on surfaces of any geometry.[32]

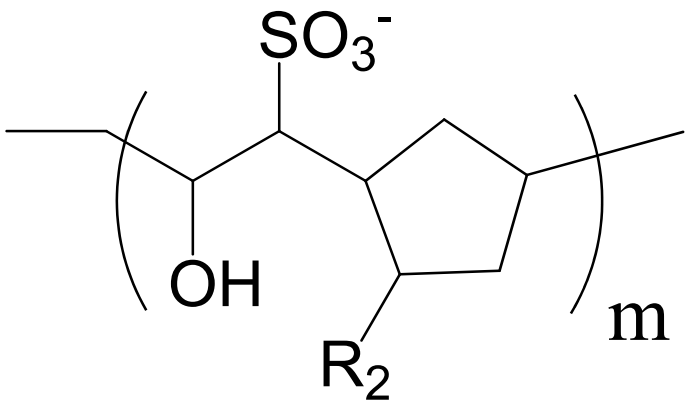

Figure 2.5. Chemical structure of sulfonated poly(5-(perfluoro-n-alkyl)norbornenes) where R_2 = C_4F_9, C_6F_{13}, C_8F_{17}, $C_{10}F_{21}$.

Surface-Initiated Polymerization

Surface-initiated polymerization (SIP) is a commonly used method for coating complex, three dimensional substrates.[33-36] Conformal polymer coatings on irregular surfaces cannot be obtained using spin-coating or solution-casting methods due to the topical nature of these deposition techniques. Traditional polymerization techniques such as ionic, living radical, and ring-opening polymerizations are applicable as surface-initiated approaches. However, in SIP, a bottom-up approach is used in which the monomer reacts with a surface-tethered initiator or polymerization catalyst, resulting in

the growth of a polymer chain from the surface. SIPs offer rapid film growth,[37] improved adhesion due to a chemical attachment of the initiator/polymer chain to the substrate, the ability to prepare uniform, conformal coatings on objects of any shape,[38] excellent control over film thickness,[39] from a few nanometers up to the micron level,[37] tunable grafting densities,[34] and good control over depth-dependent composition by enabling the growth of additional blocks to prepare copolymer films.[40-42] These films are already used in applications traditionally dominated by spin coating and solution casting, such as polymer dielectric layers,[37] etch resists for lithography,[43, 44] responsive polymer films,[45, 46] and membrane separations.[47, 48]

Highly Porous Electrodes

Nanoporous Gold Leaf

The current measured by an electrode scales with its electrochemically active area, and thus, the fabrication and modification of highly porous conductive substrates is an active area of research. These porous electrodes can be fabricated using casting and etching methods involving colloidal dispersions[49] or block copolymers,[50, 51] the anodization of oxides, such as alumina,[52] and electrochemical acid treatments of silicon.[53] The latter two methods require additional processing to increase their conductivity to function as electrodes. Porous gold electrodes are advantageous for their chemical stability, wide active electrochemical window, and ease of surface modification with thiols[54] and disulfides.[55] However, there are few simple methods available to synthesize nanoporous metallic structures. One such method is the dealloying of gold/silver leaf alloy reported by Erlebacher et al.[53] to create a mesoporous gold substrate, shown in

Figure 2.6. As the leaf is inserted into nitric acid, the acid selectively etches the silver from the alloy. The remaining gold tends to cluster into mesh-like islands that allow the dissolution front to move further into the material, leaving behind nanoporous gold mesh structures.[56, 57] This process occurs rapidly (< 5 min) for thin sheets ~100 nm thick. The average mesh size of the nanoporous gold structure is tunable through additional annealing time, which allows the gold structure to coarsen and lowers the specific surface area while increasing ligament and pore size.[56]

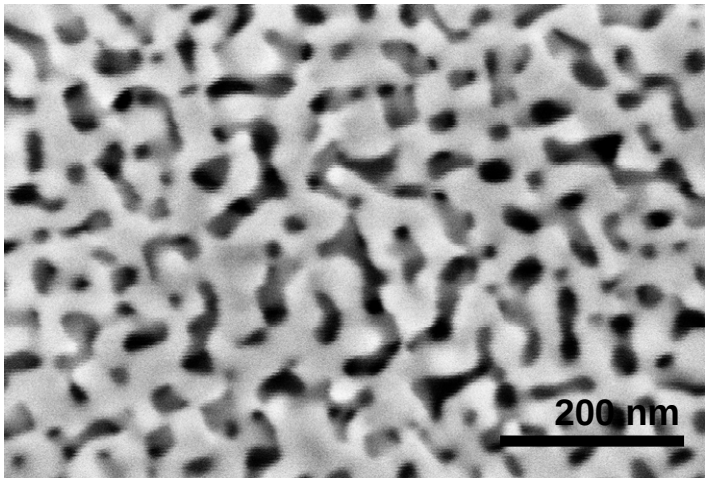

Figure 2.6. Scanning electron micrograph of nanoporous gold leaf prepared by exposing a gold/silver leaf to nitric acid for 4 h.

Modified Carbon Electrodes

Functionalized carbon electrodes have widespread applications in sensing,[58, 59] analytical electrochemistry,[60] and fuel cell designs.[61] In particular, carbon electrodes coated with thin polymer membrane films can selectively mitigate the transfer of desired species, thereby enhancing the signal for chemical[62] and biological sensing[63] or enhancing catalytic reactions. These membranes can be discretionary using molecule size, charge, or chemical affinity. A notable example is the perfluorinated ionomer

Nafion which has been used as a barrier against anionic species while facilitating transport of hydrophobic cations. Moussy et al. were able to fabricate a carbon electrode modified with a membrane film comprised of porphyrin and Nafion that enhances the selectivity of NO over NO_2^- such that concentrations as low as 10 nM of NO could be detected.[64]

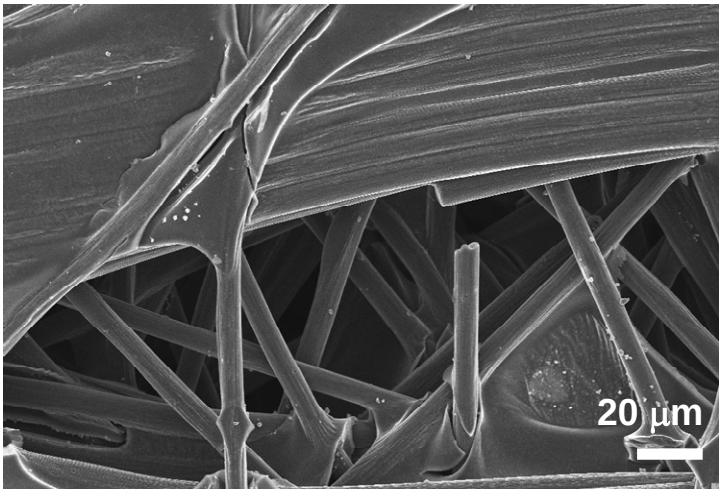

Figure 2.7. Scanning electron micrograph of unmodified carbon paper.

Carbon paper (Figure 2.7) is an attractive substrate as it provides a 3-D, high surface area porous electrode at reasonable cost. Polymerization initiators are attached to carbon electrodes by either reductive or oxidative methods. Reduction of chemical moieties onto the carbon surface is primarily carried out electrochemically using aryldiazonium salts.[65, 66] Non-electrochemical methods include the use of chemical reducing agents, such as H_3PO_2, to covalently attach salt cations to the carbon substrate.[67] In contrast to reductive techniques, oxidative modifications can erode the carbon surface. Typical oxidation processes include O_2 plasma[68, 69] or concentrated acid washes[69-71] as well as electrochemical,[72, 73] or high temperature[69] treatments of the carbon. Upon

oxidation, the carbon electrodes are further modified using appropriate chemistry to attach the desired ligand to the surface. In Chapter IX, we describe the SIP of 5-(perfluorohexyl)norbornene on carbon paper.

References

1. Amunts, A.; Drory, O.; Nelson, N., The structure of a plant photosystem I supercomplex at 3.4 angstrom resolution. *Nature* **2007,** 447, 58-63.

2. Ben-Shem, A.; Frolov, F.; Nelson, N., Crystal structure of plant photosystem I. *Nature* **2003,** 426, 630-635.

3. Nelson, N.; Yocum, C. F., Structure and Function of Photosystems I and II. *Annu. Rev. Plant Biol.* **2006,** 57, 521-565.

4. Kruse, O.; Rupprecht, J.; Mussgnug, J. H.; Dismukes, G. C.; Hankamer, B., Photosythesis: a blueprint for solar energy capture and biohydrogen production technologies. *Photochem. Photobiol. Sci.* **2005,** 4, 957-969.

5. Albertsson, P. A.; Andreasson, E., The domain organization of the plant thylakoid membrane. *FEBS* **1990,** 273, 36-40.

6. Albertsson, P. A., A quantitative model of the domain structure of the photosynthetic membrane. *Trends Plant Science* **2001,** 6, 349-358.

7. Joliot, P.; Joliot, A., Cyclic electron transfer in plant leaf. *Proc. Nat. Acad. Sci. USA* **2002,** 99, 10209-10214.

8. Joliot, P.; Joliot, A., Quantification of cyclic and linear flows in plants. *Proc. Nat. Acad. Sci. USA* **2005,** 102, 4913-4918.

9. Schubert, W.; Klukas, O.; Krauss, N.; Saegner, W.; Fromme, P.; Witt, H., Photosystem I of Synechoccus Elongatus at 4 Angstrom Resolution: Comprehensive Structure Analysis. *J. Mol. Biol.* **1997,** 272, 741-769.

10. Ben-Shem, A.; Frolow, F.; Nelson, N., Crystal structure of plant photosystem I. *Nature* **2003,** 426, 630-635.

11. Horton, R. C.; Herne, T. M.; Myles, D. C., *Journal of American Chemical Society* **1997,** 119, 12980-12981.

12. Riepl, M.; Enander, K.; Liedberg, B.; Schaferling, M.; Kruschina, M.; Ortigao, F., Functionalized Surfaces of Mixed Alkanethiols on Gold as a Platform for Oligonucleotide Microarrays. *Langmuir* **2002,** 18, 7016-7023.

13. Culha, M.; Stokes, D.; Allain, L. R.; Vo-Dinh, T., Surface-Enhanced Raman Scattering Substrate Based on a Self-Assembled Monolayer for Use in Gene Diagnostics. *Analytical Chemistry* **2003,** 75, 6196-6201.

14. Lopez, G. P.; Biebuyck, H. A.; Horter, R.; Kumar, A.; Whitesides, G. M., *Journal of American Chemical Society* **1993,** 115, 10774-107781.

15. Mrksich, M.; Whitesides, G. M., Patterning self-assembled monolayer using microcontact printing- a new technology for biosensors. *TIBTECH* **1995,** 13, 228-235.

16. Mrksich, M.; Whitesides, G. M., Using self-assembled monolayers to understand the interactions of man-made surfaces with proteins and cells. *Annu. Rev. Biophys. Biomol. Struc.* **1996,** 25, 55-78.

17. Ostuni, E.; Yan, L.; Whitesides, G. M., The interaction of proteins and cells with self-assembled monolayers of alkanethiolateson gold and silver. *Colloids and Surfaces B: Biointerfaces* **1999,** 15, 3-30.

18. Wagner, P.; Kernen, P.; Hegner, M.; Ungewickell, E.; Semenza, G., Covalent anchoring of proteins onto gold-directed NHS-terminated self-assembled monolayers in aqueous bufffers: SFM images of clathrin cages and triskelia. *FEBS* **1994,** 356, 267-271.

19. Lee, I.; Lee, J. W.; Greenbaum, E., Biomolecular electronics: Vectorial arrays of photosynthetic reaction centers. *Phys. Rev. Lett.* **1997,** 79, 3294-3297.

20. Lee, I.; Lee, J. W.; Stubna, A.; Greenbaum, E., Measurement of electrostatic potentials above oriented single photosynthetic reaction centers. *Journal of Physical Chemistry B* **2000,** 104, 2439-2443.

21. Terasaki, N.; Yamamoto, N.; Hiraga, T.; Sato, I.; Inoue, Y.; Yamada, S., Fabrication of Novel Photosystem I - Gold Nanoparticle Hybrids and their Photocurrent Enhancement. *Thin Solid Films* **2006**, 153-156.

22. Munge, B.; Das, S. K.; Ilagan, R.; Pendon, Z.; Yang, J.; Frank, H. A.; Rusling, J. F., Electron Transfer Reactions of Redox Cofactors in Spinach Photosystem I Reaction

Center Protein in Lipid Films on Electrodes. *Journal of American Chemical Society* **2003,** 125, 12457-12463.

23. Ko, B. S.; Babcock, B.; Jennings, G. K.; Tilden, S. G.; Peterson, R. R.; Cliffel, D., Effect of Surface Composition on the Adsorption of Photosystem I onto Alkanethiolate Self-Assembled Monolayers on Gold. *Langmuir* **2004,** 20, 4033-4038.

24. Ciobanu, M.; Kincaid, H. A.; Jennings, G. K.; Cliffel, D. E., Photosystem I patterning imaged by scanning electrochemical microscopy. *Langmuir* **2005,** 21, 693-698.

25. Das, R.; Kiley, P. J.; Segal, M.; Norville, J.; Yu, A. A.; Wang, L.; Trammell, S. A.; Reddick, L. E.; Kumar, R.; Stellacci, F.; Lebedev, N.; Schnur, J.; Bruce, B. D.; Zhang, S.; Baldo, M., Integration of Photosynthetic Protein Molecular Complexes in a Solid-State Electronic Device. *Nano Letters* **2004,** 4, 1079-1083.

26. Frolov, L.; Rosenwaks, Y.; Carmeli, C.; Carmeli, I., Fabrication of a Photoelectric Device by Direct Chemical Binding of Photosynthetic Reaction Center Protein to Metal Surfaces. *Advanced Materials* **2005,** 17, 2434-2437.

27. Carmeli, I.; Frolov, L.; Carmeli, C.; Richter, S., Photovoltaic Activity of Photosystem I - Based Self-Assembled Monolayer. *Journal of American Chemical Society* **2007,** 129, 12352-12353.

28. Frolov, L.; Wilner, O.; Carmeli, C.; Carmeli, I., Fabrication of oriented multilayers of photosystem I proteins on solid surfaces by auto-metallization. *Advanced Materials* **2008,** 20, 263-266.

29. Izawa, S., Acceptors and Donors for Chloroplast Electron Transport. *Methods in Enzymology* **1980,** 69, 413-434.

30. Li, Q.; Jensen, J. O.; Savinell, R. F.; Bjerrum, N. J., High temperature proton exchange membranes based on polybenzimidazoles for fuel cells. *Progress in Polymer Science* **2009,** 34, 449-477.

31. Muhlebach, A.; van der Schaaf, P. A.; Hafner, A.; Setiabudi, F., Thermal stability and degradation of hydrocarbon metathesis polymers. *Journal of Molecular Catalysis a-Chemical* **1998,** 132, 181-188.

32. Buchmeiser, M. R.; Sinner, F.; Mupa, M.; Wurst, K., Ring-Opening Metathesis Polymerization for the Preparation of Surface-Grafted Polymer Supports. *Macromolecules* **2000,** 33, 32-39.

33. Jennings, G. K.; Brantley, E. L., Physicochemical properties of surface-initiated polymer films in the modification and processing of materials. *Adv. Mater.* **2004,** 16, 1983-1994.

34. Jordi, M. A.; Seery, T. A. P., Quantitative determination of the chemical composition of silica-poly(norbornene) nanocomposites. *J. Am. Chem. Soc.* **2005,** 127, 4416-4422.

35. Yang, Q.; Wang, L.; Xiang, W. D.; Zhou, J. F.; Tan, Q. H., *Journal of Polymer Science Part a-Polymer Chemistry* **2007,** 45, 3451-3459.

36. Buchmeiser, M. R., Metathesis polymerizations to and from surfaces. In *Surface-Initiated Polymerization I*, Springer: Berlin, 2006; Vol. 197, pp 137-171.

37. Rutenberg, I. M.; Scherman, O. A.; Grubbs, R. H.; Jiang, W.; Garfunkel, E.; Bao, Z., Synthesis of Polymer Dielectric Layers for Organic Thin Film Transistors via Surface-Initiated Ring-Opening Metathesis Polymerization. *Journal of the American Chemical Society* **2004,** 126, 4062-4063.

38. Jennings, G. K.; Brantley, E. L., Physicochemical properties of shurface-initiated polymer films in the modification and processing of materials. *Adv. Mater.* **2004,** 16, 1983-1994.

39. Kim, N. Y.; Jeon, N. L.; Choi, I. S.; Takami, S.; Harada, Y.; Finnie, K. R.; Girolami, G. S.; Nuzzo, R. G.; Whitesides, G. M.; Laibinis, P. E., Surface-Initiated Ring-Opening Metathesis Polymerization on Si/SiO2. *Macromolecules* **2000,** 33, 2793-2795.

40. Matyjaszewski, K.; Miller, P. J.; Shukla, N.; Immaraporn, B.; Gelman, A.; Luokala, B. B.; Siclovan, T. M.; Kickelbick, G.; Vallant, T.; Hoffmann, H.; Pakula, T., Polymers at interfaces: Using atom transfer radical polymerization in the controlled growth of homopolymers and block copolymers from silicon surfaces in the absence of untethered sacrificial initiator. *Macromolecules* **1999,** 32, 8716-8724.

41. Boyes, S. G.; Brittain, W. J.; Weng, X.; Cheng, S. Z. D., Synthesis, haracterization, and Properties of ABA Type Triblock Copolymer Brushes of Styrene and

Methyl Acrylate Prepared by Atom Transfer Radical Polymerization. *Macromolecules* **2002,** 35, 4960-4967.

42. Kim, J. B.; Huang, W.; Bruening, M. L.; Baker, G. L., Synthesis of Triblock Copolymer Brushes by Surface-Initiated Atom Transfer Radical Polymerization. *Macromolecules* **2002,** 35, 5410-5416.

43. Zhou, F.; Liu, W. M.; Hao, J. C.; Xu, T.; Chen, M.; Xue, Q. J., Fabrication of conducting polymer and complementary gold microstructures using polymer brushes as templates. *Adv. Funct. Mater.* **2003,** 13, 938-942.

44. Husemann, M.; Mecerreyes, D.; Hawker, C. J.; Hedrick, J. L.; Shah, R.; Abbott, N. L., Surface-initiated polymerization for amplification of self-assembled monolayers patterned by microcontact printing. *Angew. Chem., Int. Ed.* **1999,** 38, 647-649.

45. Bai, D. S.; Habersberger, B. M.; Jennings, G. K., pH-Responsive Copolymer Films by Surface-Catalyzed Growth. *J. Am. Chem. Soc.* **2005,** 127, 16486-16493.

46. Ayres, N.; Boyes, S. G.; Brittain, W. J., Stimuli-responsive polyelectrolyte polymer brushes prepared via atom-transfer radical polymerization. *Langmuir* **2007,** 23, 182-189.

47. Balachandra, A. M.; Baker, G. L.; Bruening, M. L., Preparation of composite membranes by atom transfer radical polymerization initiated from a porous support. *Journal of Membrane Science* **2003,** 227, 1-14.

48. Bai, D. S.; Elliott, S. M.; Jennings, G. K., pH-Responsive Membrane Skins by Surface-Catalyzed Polymerization. *Chem. Mater.* **2006,** 18, 5167-5169.

49. Xia, Y. N.; Gates, B.; Yin, Y. D.; Lu, Y., Monodispersed colloidal spheres: Old materials with new applications. *Advanced Materials* **2000,** 12, 693-713.

50. Chan, V. Z. H.; Hoffman, J.; Lee, V. Y.; Iatrou, H.; Avgeropoulos, A.; Hadjichristidis, N.; Miller, R. D.; Thomas, E. L., Ordered bicontinuous nanoporous and nanorelief ceramic films from self assembling polymer precursors. *Science* **1999,** 286, 1716-1719.

51. Templin, M.; Franck, A.; DuChesne, A.; Leist, H.; Zhang, Y. M.; Ulrich, R.; Schadler, V.; Wiesner, U., Organically modified aluminosilicate mesostructures from block copolymer phases. *Science* **1997,** 278, 1795-1798.

52. Foss, C. A.; Hornyak, G. L.; Stockert, J. A.; Martin, C. R., Template-synthesized nanoscopoic gold particles: optical spectra and the effects of particle size and shape. *Journal of Physical Chemistry* **1994,** 98, 2963-2971.

53. Levyclement, C.; Lagoubi, A.; Ballutaud, D.; Ozanam, F.; Chazalviel, J. N.; Neumannspallart, M. In *Porous-n-silicon produced by photoelectrochemical etching*, 1993; Elsevier Science Bv: 1993; pp 408-414.

54. Love, J. C.; Estroff, L. A.; Kriebel, J. K.; Nuzzo, R. G.; Whitesides, G. M., Self-Assembled Monolayers of Thiolates on Metals as a Form of Nanotechnology. *Chem. Rev.* **2005,** 105, 1103-1169.

55. Nuzzo, R. G.; Fusco, F. A.; Allara, D. L., Spontaneously Organized Molecular Assemblies. 3. Preparation and Properties of Solution Adsorbed Monolayers of Organic Disulfides on Gold Surfaces. *J. Am. Chem. Soc.* **1987,** 109, 2358-2367.

56. Ding, Y.; Kim, Y. J.; Erlebacher, J., Nanoporous gold leaf: "Ancient technology"/advanced material. *Advanced Materials* **2004,** 16, 1897-1900.

57. Zeis, R.; Mathur, A.; Fritz, G.; Lee, J.; Erlebacher, J., Platinum-plated nanoporous gold: An efficient, low Pt loading electrocatalyst for PEM fuel cells. *Journal of Power Sources* **2007,** 165, 65-72.

58. Gilmartin, M. A. T.; Hart, J. P., Sensing with chemically and biologically modified carbon electrodes. *Analyst* **1995,** 120, 1029-1045.

59. Wang, J., Carbon-nanotube based electrochemical biosensors: A review. *Electroanalysis* **2005,** 17, 7-14.

60. Murray, R. W.; Ewing, A. G.; Durst, R. A., Chemically modified electrodes - molecular design for electroanalysis. *Analytical Chemistry* **1987,** 59, A379-A390.

61. Bevers, D.; Rogers, R.; vonBradke, M., Examination of the influence of PTFE coating on the properties of carbon paper in polymer electrolyte fuel cells. *Journal of Power Sources* **1996,** 63, 193-201.

62. Heitzmann, M.; Basaez, L.; Brovelli, F.; Bucher, C.; Limosin, D.; Pereira, E.; Rivas, B. L.; Royal, G.; Saint-Aman, E.; Moutet, J. C., Voltammetric sensing of trace metals at a poly(pyrrole-malonic acid) film modified carbon electrode. *Electroanalysis* **2005,** 17, 1970-1976.

63. Emr, S. A.; Yacynych, A. M., Use of polymer-films in amperometric biosensors. *Electroanalysis* **1995,** 7, 913-923.

64. Moussy, F.; Jakeway, S.; Harrison, D. J.; Rajotte, R. V., In-vitro and in-vivo performance and lifetime of perfluorinated ionomer-coated glucose sensors afer high-temperature curing. *Analytical Chemistry* **1994,** 66, 3882-3888.

65. Kariuki, J. K.; McDermott, M. T., Nucleation and growth of functionalized aryl films on graphite electrodes. *Langmuir* **1999,** 15, 6534-6540.

66. Allongue, P.; Delamar, M.; Desbat, B.; Fagebaume, O.; Hitmi, R.; Pinson, J.; Saveant, J.-M., Covalent modification of carbon surfaces by aryl radicals generated from the electrochemical reduction of diazonium salts. *Journal of the American Chemical Society* **1997,** 119, 201-207.

67. Pandurangappa, M.; Lawrence, N. S.; Compton, R. G., Homogeneous chemical derivatisation of carbon particles: a novel method for funtionalising carbon surfaces. *Analyst* **2002,** 127, 1568-1571.

68. Yuan, L. Y.; Chen, C. S.; Shyu, S. S.; Lai, J. Y., Plasma surface-treatment on carbon-fiber. 1. Morphology and surface-analysis of plasma etched fibers. *Composites Science and Technology* **1992,** 45, 1-7.

69. Theodoridou, E.; Besenhard, J. O.; Fritz, H. P., Chemically modified carbon-fiber electrodes. 1. Bulk-functionalized carbon-fibers. *Journal of Electroanalytical Chemistry* **1981,** 122, 67-71.

70. Barriere, F.; Downard, A. J., Covalent modification of graphitic carbon substrates by non-electrochemical methods. *J. Solid State Electrochem* **2008,** 12, 1231-1244.

71. Chou, A.; Bocking, T.; Singh, N. K.; Gooding, J. J., Demonstration of the importance of oxygenated species at the ends of carbon nanotubes for their favourable electrochemical properties. *Chemical Communications* **2005**, 842-844.

72. Ishifune, M.; Suzuki, R.; Mima, Y.; Uchida, K.; Yamashita, N.; Kashimura, S., Novel electrochemical surface modification method of carbon fiber and its utilization to the preparation of functional electrode. *Electrochimica Acta* **2005,** 51, 14-22.

73. Downard, A. J., Electrochemically assisted covalent modification of carbon electrodes. *Electroanalysis* **2000,** 12, 1085-1096.

CHAPTER III

EXPERIMENTAL PROCEDURES AND CHARACTERIZATION METHODS

Experimental Procedures

Materials

Gold shot (99.99%) was obtained from J&J Materials, and silicon (100) wafers were purchased from Montico Silicon. Chromium-coated tungsten rods were obtained from R.D. Mathis. Deionized water (16.7 MΩ) was purified using a Modu-Pure filtration system, and 200 proof ethanol was used as received from Aaper. SpectraCarb carbon paper (2050-A) and Toray Teflon treated carbon paper (TGP-H-30) were purchased from fuelcellstore.com. 5-n-butylnorbornene (98%) and 5-n-decylnorbornene (98%) monomers were provided by Promerus Electronic Materials and used as received. 1H,1H,2H-perfluoro-1-dodecene (97%) was used as received from Matrix Scientific. Grubbs Catalyst - first generation (benzylidene-bis(tricyclohexylphosphine)dichlororuthenium), 4-mercapto-1-butanol (97%), Grubbs Catalyst – 2nd generation (1,3-Bis-(2,4,6-trimethylphenyl)-2-(imidazolidinylidene)(dichlorophenylmethylene), 1H, 1H, 2H-perfluoro-1-hexene (99%), 1H,1H,2H – perfluoro-1-octene (99%), 1H,1H,2H-perfluoro-1-decene (99%), hydroquinone, 1,2,4-trichlorobenzene, and 2,2,2-trifluoroethanol, 1-dodecanethiol (98%), hexane-1,6-dithiol (97%), copper (II) sulfate (99%), 11-Mercapto-1-undecanol (97%), $K_3Fe(CN)_6$ (99%), $K_4Fe(CN)_6 \cdot 3H_2O$ (99%), 2-aminoethanethiol hydrochlorate,

mercaptoacetic acid (MAA), terephthaldialdehyde, 1-octanethiol, N-hydroxysuccinimide, 1-(3-dimethylaminopropyl)-3-ethylcarbodiimide hydrochloride, sodium ascorbate, and 2,6 dichloroindophenol were used as received from Sigma-Aldrich. Norbornene (NB, 99%) was used as received from MP Biomedicals. Gold leaf (Monarch 12 Kt) was used as received from fineartstore.com. Dichloromethane (99.9%), potassium tetrachloroplatinate (II) (46.5-47% Pt), dicyclopentadiene (95%), trans-3,6-endo-methylene-1,2,3,6-tetrahydrophthaloyl chloride (97%), n-hexadecane (99%), acetic anhydride (99%), perfluorooctanoyl chloride ($C_7F_{15}COCl$, 98%), 1,2-dichloroethane, nitric acid (69.6%), Triton X-100, toluene (99.9%), $Na_4P_2O_7 \cdot H_2O$, $MgCl_2 \cdot 6H_2O$, $NaH_2PO_4 \cdot H_2O$, $MnCl_2 \cdot 4H_2O$, NaCl, acetone, sorbitol, ascorbic acid, HEPES, and tricine were used as received from Fisher Scientific. Hydroxylapatite fast-flow was purchased from Calbiochem. Sulfuric acid (95%) was used as received from EM Science and 1-Docosanetiol was purchased from Narchem. n-Decane (99%), n-dodecane (99%), and n-tetradecane (99%) were purchased and used as received from Alfa Aesar. N_2 and O_2 gas cylinders were obtained from A1 Compressed Gas.

Preparation of Gold Substrates

Silicon wafers were rinsed with ethanol and water, then dried in a nitrogen stream. Chromium (100 Å) and gold (1250 Å) were sequentially evaporated onto the silicon wafers at rates of < 2 Å s^{-1} in a diffusion-pumped chamber with a base pressure of under 5 x 10^{-6} torr. The wafers were typically cut into sample sizes of 1.5 cm x 3.5 cm.

Photosystem I Extraction

Commercial spinach leaves were used for PSI isolation using a modified procedure to that reported by Reeves and Hall.[1-4] Briefly, spinach leaves were finely cut and homogenized in grinding medium (0.33 M sorbitol, 10 mM $Na_4P_2O_7$, 4 mM $MgCl_2$, 2 mM ascorbic acid, pH 6.5) and then filtered and centrifuged to separate the chloroplast pellet. The pellet was resuspended in a resuspension buffer (0.33 M sorbitol, 2 mM EDTA, 1 mM $MgCl_2$, 1 mM $MnCl_2$, 50 mM HEPES, Triton X-100, pH 7.6) and centrifuged. The resulting suspension was loaded onto a hydroxylapatite column, washed with column buffer (10 mM phosphate buffer, pH 7), and eluted with elution buffer (0.2 M phosphate buffer, pH 7, with 1 mM Triton X-100). Chlorophyll concentration was analyzed using the methods described by Shiozawa et al.[1] and Markwell et al.[5] The P700 concentration was determined using methods described by Baba et al.[6] The final suspension containing approximately 20 μM PSI in elution buffer was stored at -80 ^{o}C. A more detailed description of the extraction procedure is given in Appendix A.

Synthesis of 5-(perfluoro-n-alkyl)norbornenes

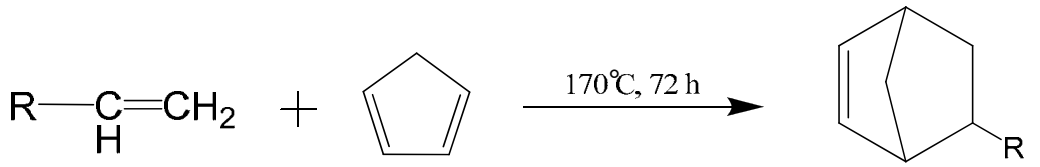

1H, 1H, 2H-perfluoroalkene Cyclopentadiene 5-(perfluoro-n-alkyl)norbornene

$R = C_nF_{2n+1}$ (n = 4, 6, 8, 10)

Figure 3.1 Schematic of the Diels-Alder reaction used to synthesize 5-(perfluoro-n-alkyl)norbornenes.

Four monomers were synthesized utilizing a Diels-Alder reaction, shown in Figure 3.1, described by Perez et al.[7]: 5-(perfluorobutyl)norbornene (NBF4), 5-

(perfluorohexyl)norbornene (NBF6), 5-(perfluorooctyl)norbornene (NBF8), and 5-(perfluorodecyl)norbornene (NBF10), with ~47%, 48%, 47%, and 50% yield, respectively. Briefly, a Parr Instruments high pressure reaction vessel was charged with 1:1 molar ratios of the 1H, 1H, 2H-perfluoro-1-alkene and dicyclopentadiene and 0.03 mol fraction of hydroquinone, as a quenching agent. The reaction was held at 170 °C for 72 h. CAUTION: Contents of reactor will be under high pressure- wait until the reaction vessel cools to room temperature before removing contents. Monomers were purified by vacuum distillation. A DRX-400 Bruker NMR spectrometer equipped with a 9.4 Tesla Oxford magnet was used to confirm the chemical structure and composition of the synthesized 5-(perfluoro-n-alkyl)norbornenes (NBFn). The reactions yielded ~3:1 ratio of endo- to exo-isomers of the NBFn as determined by ^{13}C NMR. The NMR spectra were collected using deuterated chloroform as solvent and are consistent with those reported by Perez et. al. NBF4: ^{1}H NMR ($CDCl_3$): δ 6.2, 6.0 (2H), 3.2 (1H), 3.0 (1H), 2.8 (1H), 2.0 (1H), 1.5 (1H), and 1.2-1.4 (2H). ^{19}F NMR ($CDCl_3$): δ -81.0 (s); -112.8 (m); -123.8 to -121.4 (m); -127.1 to -125.1 (m). NBF6: ^{1}H NMR ($CDCl_3$): δ 6.2, 6.0 (2H), 3.2 (1H), 3.0 (1H), 2.8 (1H), 2.0 (1H), 1.5 (1H), and 1.2-1.4 (2H). ^{19}F NMR ($CDCl_3$): δ -80.9 (s); -112.6 (m); -123.8 to -121.3 (m); -127.1 to -125.3 (m). NBF8: ^{1}H NMR ($CDCl_3$): δ 6.2, 6.0 (2H), 3.2 (1H), 3.0 (1H), 2.8 (1H), 2.0 (1H), 1.5 (1H), and 1.2-1.4 (2H). ^{19}F NMR ($CDCl_3$): δ -81.0 (s); -112.6 (m); -123.8 to -121.4 (m); -127.2 to -125.4 (m). NBF10: ^{1}H NMR ($CDCl_3$): δ 6.2, 6.0 (2H), 3.2 (1H), 3.0 (1H), 2.8 (1H), 2.0 (1H), 1.5 (1H), and 1.2-1.4 (2H). ^{19}F NMR ($CDCl_3$): δ -80.9 (s); -112.6 (m); -123.9 to -121.4 (m); -127.2 to -125.5 (m). Table 3.1 summarizes the ^{13}C NMR spectra for all monomers.

Table 3.1. Summary of ^{13}C NMR spectra for all pNBFn monomers.

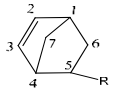

		^{13}C δ (ppm)						
Monomer	Isomer	C_1	C_2	C_3	C_4	C_5	C_6	C_7
NBF4	exo	41.1	138.2	136.2	42.3	40.6	26.7	46.3
	endo	41.9	137.2	131.7	43.5	40.8	27.4	49.6
NBF6	exo	41.1	138.1	136.2	42.3	40.6	26.7	46.2
	endo	41.9	137.1	131.6	43.5	40.7	27.4	49.5
NBF8	exo	41.2	138.2	136.3	42.4	40.6	26.7	46.3
	endo	42.0	137.2	131.7	43.6	40.7	27.5	49.6
NBF10	exo	41.1	138.1	136.2	42.3	40.6	26.7	46.2
	endo	41.9	137.1	131.6	43.5	40.9	27.4	49.5

Characterization Methods

Reflectance Absorption Infrared Spectroscopy

Reflectance absorption infrared spectroscopy (RAIRS) and polarized modulation infrared reflectance absorption spectroscopy (PM-IRRAS) are non-destructive, vibrational spectroscopic methods used to determine composition and to derive structural information from thin organic films.[8] RAIRS and PM-IRRAS involve a single reflection of an IR beam off of a reflective substrate that is coated by an organic film. The reflected radiation creates an electric field normal to the substrate. Peak positions and intensities in the IR absorption spectrum can provide compositional and structural information of the organic film. Molecular groups within the film absorb the IR radiation to yield absorbance peaks in the spectrum with intensities that depend on the concentration of those groups within the films and the orientation of their transition dipole moments relative to the electric field.[9] The observed peak for a given mode in the IR spectrum is

proportional to the square of the component of its dynamic dipole moment oriented along the surface normal, as indicated by the following equation:[10]

$$I \propto \cos^2 \theta_{mz} \tag{3-1}$$

where I represents the spectral intensity and θ_{mz} is the average angle between the transition dipole moment (m) for a particular band and the surface normal (z). Thus, a functional group with a dipole oriented mostly normal to the substrate ($\theta_{mz} \rightarrow 0°$) will have a much higher spectral intensity than a functional group oriented mostly parallel to the substrate ($\theta_{mz} \rightarrow 90°$). PM-IRRAS provides higher signal to noise ratios over RAIRS and thus, is advantageous when investigating very thin organic films, such as short-chain alkanethiolates.

Table 3.2. Correlation between protein secondary structure and IR absorbance.

Wavenumber (cm^{-1})	Secondary Structure Assignment
1616 – 1620	β-turn
1624 – 1636	β-sheet
1638 – 1645	unordered helix
1648 – 1660	α-helix
1663 – 1667	α-helix
1670 – 1676	β-sheet
1680 – 1690	β-turn
1692 – 1697	β-sheet

For a PSI film, there are two significant vibrational bands appearing in the mid-IR region corresponding to amide (N-C=O) stretching: Amide I (1600-1700 cm^{-1}) and Amide II (~1500-1600 cm^{-1}). Secondary structure of PSI can be determined by

deconvoluting the Amide I absorption peak.[11] Table 3.2 above displays the relationship between the IR absorption range and the protein structure.[11-21] PSI denaturation caused by unfolding of the protein can be determined by monitoring changes in the Amide I absorption peak. PSI interaction with the underlying SAM can also be investigated using RAIRS. Evidence of covalent attachment can be determined by the diminution (or lack thereof) of the absorbance peak for carbonyl stretching (~1680-1740 cm^{-1}) when NHS- or TPDA attachments are used (see Figure 15 (a) and (b), respectively).

For the pNBFn films, the CF_2 stretching modes absorb strongly from 1100-1400 cm^{-1}. Due to the helical structure of fluoroalkyl chains, two types of CF_2 stretching peaks are expected in the IR: those lying along the helical axis ($\nu_{ax}(CF_2)$, 1300-1400 cm^{-1}) and those perpendicular to the helical axis ($\nu_{pd}(CF_2)$, 1100-1300 cm^{-1}).[30-32] The ratio of $\nu_{pd}(CF_2)$ to $\nu_{ax}(CF_2)$ absorbance for the film, relative to the same ratio for isotropic orientation of drop-cast pNBFn films, provides information on the orientation of the fluorocarbon side chains in the polymer film relative to the surface normal.

RAIRS was performed using a Varion Excalibur FTS-3100 infrared spectrometer. The p-polarized light was incident at 80° from the surface normal. The instrument was run in single reflection mode and equipped with a universal sampling accessory. A liquid-nitrogen-cooled, narrow-band MCT detector was used to detect reflected light. Spectral resolution was 2 cm^{-1} after triangular apodization. Each spectrum was accumulated over 400 scans for polymeric films or 1000 scans for monolayer films using a deuterated octadecanethiol-d_{37} self-assembled monolayer on gold as the background.

PM-IRRAS data were collected using a Bruker PMA-50 attachment to a Bruker Tensor 26 infrared spectrometer equipped with a liquid-nitrogen-cooled mercury-

cadmium-telluride (MCT) detector and a Hinds Instruments PEM-90 photoelastic modulator. The source beam was modulated at a frequency of 50 kHz with half-wavelength ($\lambda/2$) retardation and set at 80° incident to the sample surface. Spectra for SAMs on gold substrates were collected over 760 scans at a resolution of 4 cm^{-1}. The differential reflection spectra (ΔR/R) were calculated from the s- and p-polarized signals simultaneously collected by a lock-in-amplifier.

Electrochemical Impedance Spectroscopy

Barrier properties of organic thin films may be measured with electrochemical impedance spectroscopy. In EIS, the film-coated electrode is part of an electrochemical cell with a solution containing redox probes and ions and connected to an alternating current source. During an EIS experiment, current is measured upon altering the potential of the working electrode with a sinusoidal perturbation of varying frequency. The following equation is then applicable to this situation:

$$Z = \frac{E(t)}{I(t)} = \frac{E_0 \cos(\omega t)}{I_0 \cos(\omega t - \phi)} = Z_0 \frac{\cos(\omega t)}{\cos(\omega t - \phi)} \tag{3-2}$$

where Z is the impedance of the system, $E(t)$ is the applied potential at time *t*, $I(t)$ is the resulting current at time *t*, E_0 is the amplitude of the potential, ω is the radial frequency (equals $2\pi f$ where *f* is the frequency in Hz), I_0 is the amplitude of the current, ϕ is the phase shift of the output signal, and Z_0 is the magnitude of the impedance. From these equations, the impedance of a system can be characterized by a magnitude

and a phase shift. An impedance plot is obtained by measuring cell current while altering the frequency of the ac source. The impedance changes due to the ability of redox probes to reach the vicinity of the working electrode/metal surface underlying the film where they can be oxidized/reduced. Impedance is directly affected by the transport of ions through a film, and lower frequencies allow more time for diffusive processes to occur.[22] Since an electrochemical cell is used, the results can be modeled using equivalent electrical circuits consisting of resistors and capacitors that represent film, interfacial, and solution properties. Resistance and capacitance values for the initiator and polymer layers in our films may be estimated using the following equations that apply to the equivalent circuits shown in Figure 3.2.

$$|Z| = \sqrt{(Z_{real})^2 + (Z_{imag})^2} \tag{3-3}$$

$$Z_{real} = R \tag{3-4}$$

$$Z_{imag} = \frac{I}{j\omega C} \tag{3-5}$$

where $|Z|$ equals Z_0 and is the magnitude of the total impedance, Z_{real} and Z_{imag} are the real (resistances) and imaginary (capacitances) components of the impedance, *R* denotes a resistance, and *C* denotes a capacitance. As evidenced by the impedance equations for a resistor and capacitor, higher film resistance and lower film capacitance yield higher

total impedance. Higher impedance corresponds with the inhibition of ion transport to the surface and signifies a better barrier film.[23]

EIS was performed with a Gamry Instruments CMS300 impedance system interfaced to a personal computer. A flat cell (EG&G) was used to selectively expose 1.0 cm^2 of each sample as the working electrode to an aqueous analyte solution. Measurements were taken using a Ag/AgCl/saturated KCl reference electrode with evaporated gold on silicon as the counter electrode. Data were collected between 10^{-1} and 10^4 Hz and fit using an appropriate equivalent circuit to determine resistance and capacitance values. Reported values and errors represent the averages and standard deviations, respectively.

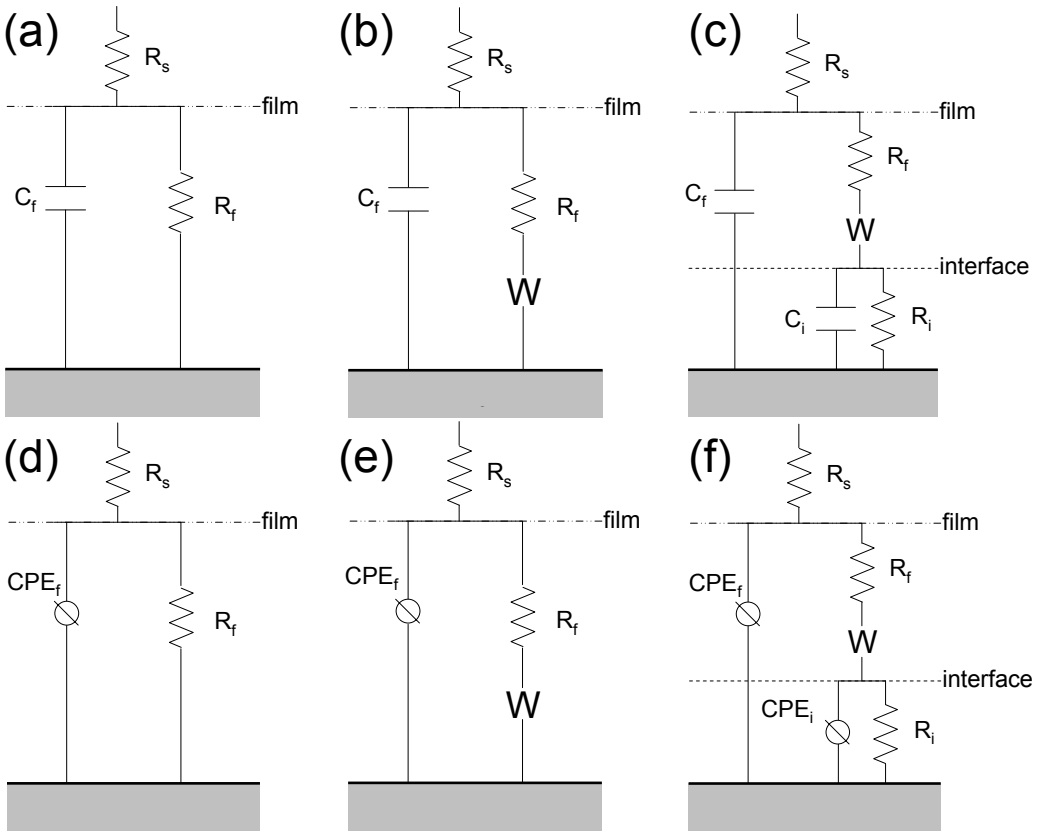

Figure 3.2. Equivalent circuits used to model impedance spectra for films on gold, nanoprous gold, and carbon paper electrodes: (a) the commonly used Randle's circuit; (b) the Randles circuit model modified with a Warberg impedance; (c) the two-time constant model with mass transfer limitations; (d) the constant-phase-element equivalent of a Randle's circuit; (e) the constant-phase-element circuit modified with a Warberg impedance; and (f) the constant-phase-element equivalent of the two-time constant model. The constant phase element allows for film inhomogeneity and the modeling of "leaky" capacitors.

Cyclic Voltammetry (CV)

Cyclic voltammetry is the dynamic measurement of current at the working electrode as a result of a linearly-sweeping potential in a standard three electrode electrochemical cell. The potential is applied and is varied at a constant rate to a predefined potential limit, at which the direction of the scan is reversed and the potential is scanned in the opposite direction.[22, 24] In a redox experiment, species deposited via reduction on the forward scan are oxidized and desorbed on the reverse scan.

CV was performed with a Gamry Instruments CMS300 impedance system interfaced to a personal computer. A flat cell (EG&G) was used to selectively expose 1.0 cm^2 of each sample as the working electrode to an aqueous analyte solution. Reported values and errors represent the averages and standard deviations, respectively obtained from at least 3 different experiments. Details of the specific CVs used for copper underpotential deposition, thiolate desorption, and oxygen reduction reaction are discussed in Chapter VII.

Underpotential Deposition (UPD)

Underpotential deposition is a plating technique where the deposition of a metal adlayer onto a metal substrate occurs at potentials more positive than the equilibrium potential of the given species. This equilibrium potential (E_{eq}) is governed by the Nernst Equation:

$$E_{eq} = E^0 + \frac{RT}{nF}\ln(\frac{a^{red}}{a^{ox}}) \tag{3-6}$$

where E^0 is the standard potential, R is the gas constant, T is the absolute temperature, n is the number of electrons transferred, a is the chemical activity, and F is the Faraday constant.[25] UPD enables the deposition of submonolayer coverages of a less noble metal adlayer onto a more noble substrate. UPD is typically accomplished in a CV experiment, where deposition of the adlayer is observed as cathodic current and removal of the adlayer is observed as anodic current. The potential is held at a value corresponding to the desired adlayer coverage, and the working electrode is removed under constant potential. We utilize UPD to deposit a submonolayer of copper (less noble adlayer) onto

polycrystalline gold (more noble) substrates. Potentials are cycled between 500 and 50 mV vs. $Cu^{0/1+}$ in a solution of 1.0 mM $CuSO_4$ in 0.1 M H_2SO_4 (aq, nitrogen saturated). On polycrystalline gold, only one copper UPD peak (~200 mV) can typically be distinguished from the deposition of bulk copper.[26] Underpotential deposition of copper was performed with a Gamry Instruments CMS300 impedance system interfaced to a personal computer. After at least two cycles, the potential was held just negative of the UPD peak on the cathodic sweep (~100 mV), and the sample was removed from solution under potential control. Samples were rinsed in ethanol and dried in a nitrogen stream.

Photochronoamperometry

We used photochronoamperometry to investigate the effect of light on the current production from PSI films. Chronoamperometry is a measurement of current produced over time from a working electrode while a potential step is applied to the working electrode in the presence of redox mediators.[22] In our photochronoamperometric measurements, no potential step is made; however, a step in light exposure is used instead (i.e. from dark or no light to light and vice versa). By keeping the potential of the working electrode constant, the current produced by PSI films were measured exclusively. The photo-current response of PSI can be affected by diffusional limitations of electron transport mediators. The decay of the photo-current response is described by the Cottrell Equation:

$$I_{\lim} = nFAc\sqrt{\frac{D}{t\pi}} \tag{3-7}$$

where n is the number of electrons transferred in the reaction, F is Faraday's constant, A is the surface area of the electrode, c is the bulk concentration of electron mediator, D is

the diffusion coefficient of the mediator, and *t* is the time elapsed since the potential step (in our experiments, light). Eqn. 3-7 strictly describes diffusional mass transfer only; deviations from this model include convection or a non-diffusion limited system.[27]

Photochronoamperometric measurements taken over a span of discrete potential steps also provide valuable kinetic information. Plotting the amperometric responses vs. potential setting on a log scale creates a graph known as a Tafel plot. Tafel plots have two primary domains: a kinetically limited region in which electron transfer between the electrode and mediator is capped by the set potential, and a diffusion-limited region in which the concentration of mediator near the electrode surface is not sufficient to drive the redox reaction. The current increases exponentially with increasing over-potential throughout the kinetic regime of the plot, yet is approximately constant through the diffusion-limited regime.

Light-induced chronoamperometric data were collected using a custom three-electrode electrochemical cell attached to a CH Instruments CHI660a electrochemical workstation equipped with a Faraday cage. A Ag/AgCl (saturated KCl) electrode was used as a reference electrode, and a Pt mesh was used as a counter electrode. The electrolyte medium contained 5 mM phosphate buffer, 100 mM sodium chloride, 250 μM 2,6 dichloroindophenol, and 5 mM sodium ascorbate. A 500 lumens Leica KL2500 cold lamp equipped with a red light filter was used as a light source. The working electrode was set to a -0.11 V potential bias during data collection.

Spectroscopic Ellipsometry

Ellipsometery allows determination of thickness and refractive index of single films, layered stacks, and substrate materials with very high sensitivity.[28] Film thickness between 0.1 nm and 100 μm can be measured, depending on the spectral range used and the homogeneity of the thicker films. Thickness < 1 μm can be determined with a sensitivity better than 0.01 nm.[28] Linear polarized light in a specified wavelength range is reflected from a sample surface and changed into elliptically polarized light. Both the polarization change, phase (Δ) and amplitude (Ψ), of the reflected light are collected by a detector. Information about the properties of the sample are contained in the complex ratio, ρ is the Fresnel coefficient of reflection comprised of the parallel (r_p) and perpendicular (r_s) electrical field vectors.

$$\rho = \frac{r_P}{r_s} \tag{3-8}$$

The fundamental equation of ellipsometry

$$\rho = \tan\psi e^{i}\Delta \tag{3-9}$$

describes the connection between the measured quantities Ψ (amplitude) and Δ (phase) and the sample properties contained in the coefficient of reflection ρ. Model layers representing the film on the surface can be created to fit theory to the measured data.

A simple, effective model for thin organic films is the Cauchy Equation:

$$n = A + \frac{B}{\lambda^2} + \frac{C}{\lambda^4} + \ldots, \tag{3-10}$$

where *n* is the film refractive index, *A*, *B* and *C* are model fit parameters, and λ is the wavelength of incident light. The Cauchy model assumes a film to be optically transparent and uniform in thickness.

A J. A. Woollam Co. M-2000DI variable angle spectroscopic ellipsometer with WVASE32 software for modeling was used for all ellipsometric measurements. The optical source beam was set at a 75^{o} incident angle to the sample surface and data was taken from 400 nm – 700 nm. Thickness measurements were extrapolated using a one parameter Cauchy model with an index of refraction of 1.45 for alkanethiol monolayers, 1.33 for PSI films,[29] and 1.38 for fluorocarbon polymer films.[30] Reported values and errors are the averages and standard deviations, respectively, of at least three independently prepared samples.

Profilometry

A profiler uses a stylus tip to map surface topography and roughness by measuring changes in the height of the stylus tip as it probes the surface using direct contanct.[31] Profilers have excellent vertical resolution, on the order of tens of nm, and decent lateral resolution, on the order of hundreds of nm.[31] A Veeco Dektak stylus profiler equipped with a high aspect ratio tip was used to determine pNBF6 film thicknesses that exceeded 100 nm.

Atomic Force Microscopy

Atomic force microscopy (AFM) consists of a small cantilever with a nanometer scale tip that is brought into contact with the surface being examined. The deflection of the cantilever by the surface is monitored by the position of laser light reflected off the cantilever.[31, 32] Tapping mode (intermittent contact mode or dynamic contact mode) AFM refers to the oscillation of the cantilever and detecting changes in the phase or

amplitude of the oscillations to provide information on the surface. For soft surfaces, such as protein or polymeric films, AFM is generally operated in tapping mode to eliminate lateral forces that could potentially damage the surface and distort the topographical image.[32] We used a JEOL 5200 scanning probe microscope (SPM) to investigate the surface morphology and uniformity of PSI and pNBFn films. Height contrast images (20 μm x 20 μm) were collected in tapping mode using a silicon nitride tip. The images were plane-fitted and filtered to remove noise using the instrument software.

Scanning Electron Microscopy

Scanning electron microscopy (SEM) uses a focused beam of electrons (in vacuum) to probe a target surface or film. Upon interaction with the target sample, the electrons and photons are emitted from, or through, the sample and collected using appropriate detectors. The output of the detectors is synchronized with the directional coordinates of the rastering electron beam to create an image of the surface. The SEM image can yield information on morphology, composition, and crystallography about the target sample using three imaging techniques available in SEM: secondary electron images, backscattered electron images, and energy-dispersive X-ray analysis.[33] We obtained scanning electron micrographs using a Raith eLINE electron beam lithography tool in image mode with an accelerating voltage of 10.0 kV and a working distance of 10 mm equipped with a backscattering detector. We used the Raith to characterize unmodified NPGL and carbon paper electrodes, as well as, pNBFn films on planar polycrystalline gold, nanoporous gold, and carbon paper electrodes. SEM images were

also collected to investigate the morphology of PSI multilayer films on planar polycrystalline gold electrodes.

X-ray Photoelectron Spectroscopy

X-ray photoelectron spectroscopy (XPS) is an ultra high vacuum technique where a material is irradiated with x-rays while the kinetic energy and number of escaping electrons are measured. The kinetic energy can be used to determine the composition, chemical state, and electronic state of the outermost ~10 nm of a material.[34] Data are typically reported as counts per second against binding energy. Binding energy (E_B) is related to the kinetic energy (E_K) by equation 3-8, where $h\nu$ is the energy of the incident photons and Φ is the work function of the spectrometer.[34]

$$E_K = h\nu - E_B - \Phi \tag{3-11}$$

We used XPS to investigate the extent of Cu and Pt coverage on a gold electrode (discussed in Chapter VII), as well as, the surface concentration of oxygen and fluorine moieties on carbon paper (discussed in Chapter IX). X-ray Photoelectron spectra were obtained with a PHI 5000 VersaProbe spectrometer equipped with a monochromatized Al Kα X-ray source (square spot of 100 μm x 100 μm) and a concentric hemispherical analyzer (pass energy = 150 eV). The detector angle with respect to the surface normal was 45°. Peak positions were referenced to Au($4f_{7/2}$) = 84.2 eV, and peaks were fit with 70% Gaussian/30% Lorentzian profiles and a Shirley background.

Contact Angle Goniometry

The surface properties of films can be measured using the simple, direct method of contact angle goniometry.[35] When a small drop of liquid is placed onto a surface, the interfacial tensions between the drop, the film surface, and air determine the shape of the drop. The interfacial tensions are denoted as γ_{SV} at the solid-vapor interface, γ_{SL} at the solid-liquid interface, and γ_{LV} at the liquid-vapor interface. A force balance of these tensions involved in the surface-liquid-air interface leads to Young's equation:

$$\gamma_{SV} - \gamma_{SL} = \gamma_{LV} \cos\theta \tag{3-12}$$

where the contact angle, θ, is the angle between the line drawn tangent to the edge of the liquid drop (at the liquid-vapor interface) and the line flush with the surface underneath the drop (the solid-liquid interface). For a given liquid, typically water or hexadecane, γ_{LV} is held constant while all other values change depending on surface composition. A goniometer, an optical microscope with a protractor built into the lens, is used to determine θ. Water contact angles are used to indicate the relative hydrophilicity/hydrophobicity of a surface, while hexadecane is used for oleophilicity / oleophobicity. Larger measured angles result from more hydrophobic and oleophobic surfaces.

Contact angles are useful in providing insight into surface roughness, chemical composition, and interfacial structure. By adding small liquid drops (~5μL) to the surface using a microliter syringe, the advancing contact angle θ_A and receding contact angle θ_R are generally measured. θ_A is measured after liquid has been added to the drop,

causing it to slowly advance across the surface, and θ_R is measured after liquid has been removed from the drop, causing it to slowly recede across the surface. The chemical composition at the surface also greatly affects the measured contact angles. Depending on whether a surface is dominated by $-CH_2-$, $-CH_3$, $-CF_2-$, $-CF_3$, or higher energy ($-SO_3-$, -OH) groups, the contact angles will be altered, shown in Table 3.3.[36] The contact angle hysteresis, $\theta_A - \theta_R$, gives a measure of the roughness or chemical heterogeneity of the surface. More homogeneous surfaces have a very low hysteresis while heterogeneous surfaces have a much larger hysteresis.[37]

Table 3.3. Typical wetting properties of omega-terminated alkane thiols on gold. [36, 38, 39]

	Advancing Contact Angle	
Surface Functionality	θ_{water}	$\theta_{hexadecane}$
$-SO_3$	< 15	< 10
-OH	25	< 10
$-CH_2-$	103	< 10
$-CH_3$	115	48
$-CF_2-$	109	53
$-CF_3$	120	83

A Rame-Hart contact angle goniometer with a microliter syringe was used to measure advancing and receding contact angles on static drops of the probing liquid on the sample surfaces. The needle tip of the syringe remained inside the liquid drop while measurements were taken on both sides of ~5 μL drops. Reported values and ranges represent the average and standard deviation of values obtained from at least five independent sample preparations.

References

1. Shiozawa, J. A.; Alberte, R. S.; Thomber, J. P., *Arch. Biochim. Biophys.* **1974,** 165, 388-397.

2. Reeves, S. G.; Hall, D. O., *Methods in Enzymology* **1980,** 69, 85-94.

3. Owens, T. G.; Webb, S. P.; Alberte, R. S.; Mets, L.; Fleming, G. R., *Proc. Nat. Acad. Sci. USA* **1987,** 84, 1532-1536.

4. Lee, J. W.; Zipfel, W.; Owens, T. G., *Journal of Luminescence* **1992,** 51, 79-89.

5. Markwell, J. P.; Thornber, J. P.; Skrdla, M. P., Effects of Detergents on the Reliability of a Chemical Assay for P-700. *Biochimica Et Biophysica Acta* **1980,** 591, 391-399.

6. Baba, K.; Itoh, S.; Hastings, G.; Hoshina, S., Photoinihibition of Photosystem I Electron Transfer Acitivity Isolated Photosystem I. *Photosynthesis Research* **1996,** 47, 121-130.

7. Perez, E.; Laval, J. P.; Bon, M.; Rico, I.; Lattes, A., Synthesis of bicyclo [2· 2· 1] hept-2-enes with mono and disubstituted long perfluorinated chains CnF2n+1 (n = 4,6,8,10) Investigation of association in solution by 19F NMR study of polymerization via a metathetic reaction. *Journal of Fluorine Chemistry* **1988,** 39, 173-196.

8. Hinrichs, K., Reflection Adsorption IR Spectroscopy (RAIRS). In *Surface and Thin Film Analysis Principle, Instrumentation, and Applications*, Bubert, H.; Jenett, H., Eds. Wiley=VCH: Weinheim, 2002.

9. Nuzzo, R. G.; Dubois, L. H.; Allara, D. L., Fundamental-Studies Of Microscopic Wetting On Organic-Surfaces .1. Formation And Structural Characterization Of A Self-Consistent Series Of Polyfunctional Organic Monolayers. *Journal of the American Chemical Society* **1990,** 112, 558.

10. Nuzzo, R. G.; Dubois, L. H.; Allara, D. L., Fundamental-Studies Of Microscopic Wetting On Organic-Surfaces .1. Formation And Structural Characterization Of A Self-Consistent Series Of Polyfunctional Organic Monolayers. *Journal of the American Chemical Society* **1990,** 112, 558-569.

11. Seshadri, S.; Khurana, R.; Fink, A. L., Fourier Transform Infrared Spectroscopy in Analysis of Protein Deposits. *Methods in Enzymology* **1999,** 309, 559-576.

12. Arrondo, J. L.; Goni, F. M., Structure and dynamics of membrane proteins as studied by infrared spectroscopy. *Progress in Biophysiscs and Molecular Biology* **1999,** 72, 367-405.

13. Fu, K.; Griebenow, K.; Hsieh, L.; Klibanov, A. M.; Langer, R., FTIR characterization of the secondary structure of proeins encapsulated within PLGA microspheres. *Journal of Controlled Release* **1999,** 58, 357-366.

14. Kota, Z.; Szalontai, B.; Droppa, M.; Horvath, G.; Pali, T., Fourier transform infrared and electron paramagnetic resonance spectroscopic studies of thylakoid membranes. *Journal of Molecular Structure* **1999,** 481, 395-400.

15. Khurana, R.; Fink, A. L., Do Parallel b-helix Proteins have a Unique Fourier Transform Infrared Spectrum? *Biophysical Journal* **2000,** 78, 994 - 1000.

16. Guiomar, A. J.; Guthrie, J. T.; Evans, S. D., Use of Mixed Monolayers in a Study of the Effect of the Microenvironment on Immobilized Glucose Oxidase. *Langmuir* **1999,** 15, 1198-1207.

17. Gilbert, S. M.; Wellner, N.; Belton, P. S.; Greenfield, J. A.; Siligardi, G.; Shewry, P. R.; Tatham, A. S., Expression and characterization of a highly repetitive peptide derived from wheat seed storage protein. *Biochimica Et Biophysica Acta* **2000,** 1479, 135-146.

18. Krueger, J. K.; Gallagher, S. C.; Wang, C. L.; Trewhalla, J., Calmodulin Remains Extended upon Binding to Smooth Muscle Caldesmon: A Combined Small-Angle Scattering and Fourier Transform Infrared Spectroscopy Study. *Biochemistry* **2000,** 39, 3979-3987.

19. Ruan, X.; Wei, J.; Xu, Q.; Wang, J.; Gong, Y.; Zhang, X.; Kuang, T.; Zhao, N., Comparison of the effects of Triton X-100 treatment on the protein secondary structure of Photosystem I and Photosystem II studied by FTIR spectroscopy. *Journal of Molecular Structure* **2000,** 525, 97-106.

20. Zhang, H.; Yamamoto, Y.; Ishikawa, Y.; Carpentier, R., Characterization of the secondary structure and thermostabiliy of the extrinsic 16 kilodalton protein of spinach

photosystem II by fourier transform infrared spectroscopy. *Journal of Molecular Structure* **1999,** 513, 127-132.

21. Heimburg, T.; Schunemann, J.; Wever, K.; Geisler, N., FTIR-Spectroscopy of Multistranded Coiled Coil Proteins. *Biochemistry* **1999,** 38, 12727-12734.

22. Bard, A. J.; Faulkner, L. R., *Electrochemical Methods: Fundamentals and Applications*. 2nd ed.; Wiley: New York, 2001.

23. Park, S. M.; Yoo, J. S., Electrochemical impedance spectroscopy for better electrochemical measurements. *Analytical Chemistry* **2003,** 75, 455A-461A.

24. Monk, P. M. S., Linear-Sweep and Cyclic Voltammetry at Solid Electrodes. In *Fundamentals of Electroanalytical Chemistry*, John Wiley & Sons: Manchester, 2001; pp 156-176.

25. Herzog, G.; Arrigan, D. W. M., Determination of trace metals by underpotential deposition-stripping voltammetry at solid electrodes. *Trac-Trends in Analytical Chemistry* **2005,** 24, 208-217.

26. Jennings, G. K.; Laibinis, P. E., *J. Am. Chem. Soc.* **1997,** 119, 5208-5214.

27. Monk, P. M. S., Chronoamperometry: Current Determined with Time. In *Fundamentals of Electroanalytical Chemistry*, John Wiley & Sons: Manchester, 2001; pp 136-142.

28. Robinson, K. L.; Khan, M. A.; Banez, M. V. D.; Wang, X. S., *Macromolecules* **2001,** 34, 3155-3158.

29. Kincaid, H. A.; Niedrinhaus, T.; Ciobanu, M.; Cliffel, D. E.; Jennings, G. K., Entrapment of Photosystem I within Self-Assembled Films. *Langmuir* **2006,** 22, 8114-8120.

30. Seehof, N.; Grutke, S.; Risse, W., *Macromolecules* **1993,** 26, 695-700.

31. Stevie, F. A., Surface Roughness. In *Encyclopedia of Materials Characterization*, Brundle, C. R.; Jr., C. A. E.; Wilson, S., Eds. Butterworth-Heinemann: Boston, 1992; pp 689-710.

32. Garcia, R.; Perez, R., Dynamic atomic force microscopy methods. *Surface Science Reports* **2002,** 47, 197-301.

33. Bindell, J. B., Scanning Electron Microscopy. In *Encyclopedia of Materials Characterization: Surfaces, Interfaces, Thin Films*, Fitzpatrick, L. E., Ed. Butterworth-Heinemann: Stoneham, MA, 1992; pp 70-84.

34. Briggs, D.; Seah, M. P., *Practical Surface Analysis*. John Wiley & Sons Ltd.: Chichester, 1983.

35. Laibinis, P. E.; Bain, C. D.; Nuzzo, R. G.; Whitesides, G. M., Structure and wetting properties of omega-alkoxy-n-alkanethiolate monolayers on gold and silver. *Journal of Physical Chemistry* **1995,** 99, 7663-7676.

36. Laibinis, P. E.; Palmer, B. J.; Lee, S. W.; Jennings, G. K., The synthesis of organothiols and their assembly into monolayers on gold. In *Thin Films*, Ulman, A., Ed. Academic Press: Boston, 1998; Vol. 24, pp 1-41.

37. Zisman, W. A., *Contact Angle, Wettability, and Adhesion*. American Chemical Society: Washington, DC, 1964; Vol. 43.

38. Weinstein, R. D.; Moriarty, J.; Cushnie, E.; Colorado, R.; Lee, T. R.; Patel, M.; Alesi, W. R.; Jennings, G. K., Structure, wettability, and electrochemical barrier properties of self-assembled monolayers prepared from partially fluorinated hexadecanethiols. *Journal of Physical Chemistry B* **2003,** 107, 11626-11632.

39. Morra, A.; Occhiello, E.; Garbassi, F., Wettability and surface chemistry of irradiated PTFE. *Die Angewandte Makromolekulare Chemie* **1990,** 180, 191-198.

CHAPTER IV

RAPID ASSEMBLY OF PHOTOSYSTEM I MONOLAYERS ON GOLD ELECTRODES

Introduction

Heightened awareness on global warming and an increasing demand for energy has generated a surging interest in the harnessing of solar radiation, which offers the greatest capacity of all alternative energy sources.[1] Natural light harvesting complexes are exceptionally efficient in converting captured photons with a quantum yield near 1.0.[2] Recently, Photosystem I (PSI), a 500 kDa protein complex[3] essential in the electron transfer process of photosynthesis, has been extracted from plants and cyanobacteria and assembled at electrode surfaces to investigate biomimetic solar energy conversion.[4] Orientation of adsorbed PSI layers on an electrode is a critical concern because PSI behaves as a photodiode, enabling electron transfer from the P700 reaction center to the F_A/F_B sites once a photon of light is captured.

Traditional methods for incorporating PSI into photovoltaics and electrochemical cells primarily include adsorption of extracted PSI from solution onto self-assembled monolayers (SAMs) on gold electrodes through physical or electrostatic interactions.[5-10] PSI has also been successfully tethered to a gold electrode through genetic mutation of specific subunits or residues.[11-13] These approaches can be labor intensive and may require many hours to achieve dense PSI layers that are effective in solar energy conversion. New fabrication methods that enable rapid assembly of oriented PSI

monolayers can offer a profound impact in the preparation of biomimetic solar cells and devices.

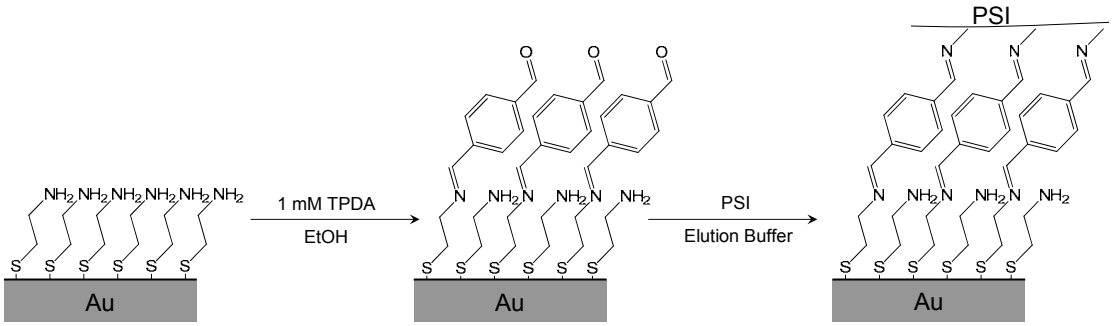

Figure 4.1. Covalent attachment of PSI to a gold substrate. An amine-terminated SAM is reacted with TPDA to form aldhydic termini, which are reactive with lysine residues of PSI to form covalent imine bonds.

In this chapter, we describe a rapid and effective method for achieving dense, oriented monolayer films of PSI. The versatility of this approach is demonstrated by the formation of precipitated monolayers of PSI, isolated from commercial spinach leaves, onto a variety of low and high energy surfaces alike. The method is similar to that where solvent evaporation is utilized to increase protein concentration upon surface attachment for preparation of assay arrays.[14] However, the majority of these methods involve heating the solution or extensive periods of time. Here, we reduce the pressure of the system in order to achieve rapid evaporation of solvent without thermal degradation of PSI.

Experimental Procedures

Preparation of SAMs.

The SAMs were prepared by immersing gold-coated silicon samples into 1 mM ω-terminated alkyl thiol solutions for 24 h at room temperature. Carboxyl-terminated SAMs were further modified by immersing the samples in 5 mM N-hydroxysuccinimide (NHS)and 20 mM 1-Ethyl-3-(3-dimethylaminopropyl)carbodiimide (EDCI) aqueous solution for 1 h. Amine-terminated SAMs were further modified by immersing the samples in a 1 mM TPDA aqueous solution for 1 h. The samples were rinsed with ethanol and water and dried under a stream of nitrogen following SAM formation and modification.

Results and Discussion

As an example of an effective approach, we exposed an amine-terminated SAM, prepared from adsorption of 2-aminoethanethiol onto gold, to a 1 mM solution of terephthaldialdehyde (TPDA) in ethanol for 1 h (Figure 4.1). The TPDA-capped SAM can bind lysine residues of proteins through covalent imine bonds.[15] An aqueous solution of PSI (~$1.9 \cdot 10^{-5}$ mol/L) containing 0.2 M phosphate buffer and 0.9 mM Triton X-100 was then deposited onto the TPDA-modified SAM, Figure 4.2(a), and placed under vacuum (~30 mTorr) for 5 – 180 min. As the water evaporates from the film, PSI aggregates form and crash out of solution since PSI is by far the least soluble component in this aqueous buffer solution. A thick film (~20 μm) of PSI, salt, and Triton X-100 is precipitated upon complete removal of the water, Figure 4.2(b). A dense and covalently

bound monolayer (~70 Å ellipsometric thickness) remains after thoroughly rinsing this film with water, Figure 4.2(c).

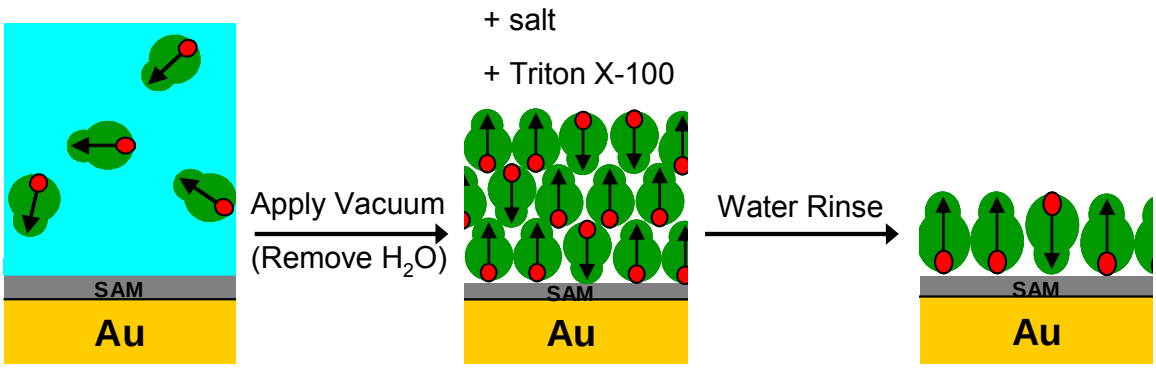

Figure 4.2. Vacuum-assisted approach for rapidly forming dense PSI monolayers.

Although covalent attachment utilizing lysine residues is not as selective as some other covalent attachment methods due to the abundance of lysines within PSI, the surface of subunit F near the P700 reaction center does contain multiple exposed lysine residues.[3] This fact, coupled with the tendency for PSI to orient with its luminal side nearest the electrode surface on high energy surfaces,[4,10] suggests that our approach can preferentially and covalently bind PSI with P700 proximal to the electrode for facile electron transfer.

Figure 4.3 shows polarized modulation infrared reflectance-absorption spectra (PM-IRRAS) of the amine-terminated SAM, the same SAM after capping with TPDA, and after exposure to PSI using the vacuum-assisted assembly approach shown in Figure 4.2. After exposure of the amine-terminated SAM (Figure 4.3(a)) to a 1 mM TPDA solution for 1 h (Figure 4.3(b)), TPDA conversion of the amine termini is evidenced by the appearance of a peak at ~1716 cm^{-1} corresponding to aldehydic C=O stretching and a peak at ~1640 cm^{-1} corresponding to imine stretching, (Figure 4.3(b)). Upon exposure of

TPDA-terminated films to ~19 μM PSI, covalent attachment is evidenced by the diminution of the carbonyl peak (~1716 cm^{-1}) and the appearance of strong Amide I and Amide II peaks at ~1662 cm^{-1} and ~1540 cm^{-1}, respectively (Figure 4.3(c)). The ~80% reduction of the ~1716 cm^{-1} carbonyl peak is consistent with the formation of multiple imine bonds between a single PSI complex and the underlying SAM since many TPDA groups would be underneath the ~80 nm^2 footprint of PSI.

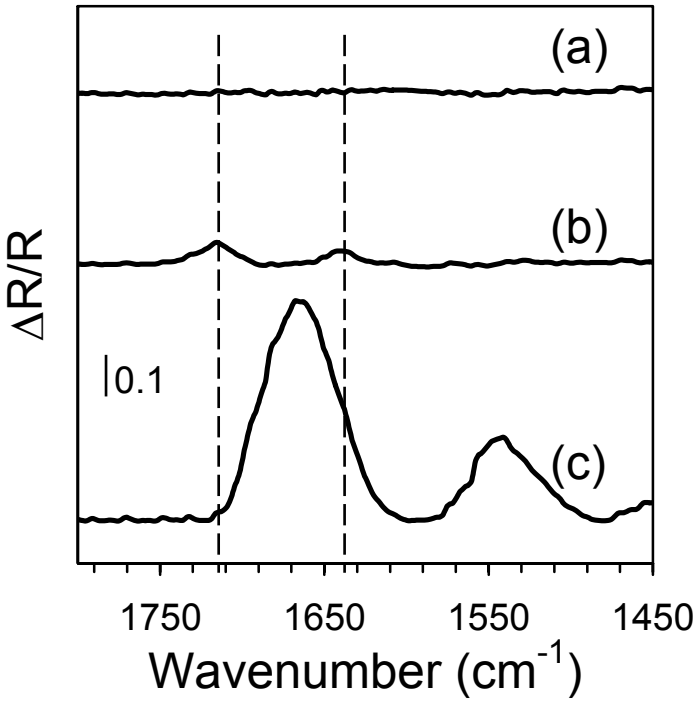

Figure 4.3. PM-IRRA spectral evidence of PSI covalent attachment. Spectra are shown for an amino-terminated SAM (a), a TPDA-functionalized SAM (b), and a PSI monolayer (c).

The PSI film that is attached through the TPDA-terminated SAM by the vacuum-assisted approach for 30 min has an ellipsometric thickness of 67 ± 7 Å, which is consistent with a dense monolayer of PSI, considering its size[16] and the accompanying free volume when curved objects such as PSI pack into a 2-D film. Using atomic force

microscopy (AFM) we confirm the formation of a dense PSI monolayer with a RMS roughness of 1.9 nm, as shown in Figure 4.4. As further confirmation that this PSI film is indeed a dense monolayer rather than a sparse multilayer, we have exposed it to a 1 mM solution of docosanethiol ($C_{22}SH$) in ethanol for 2 h.

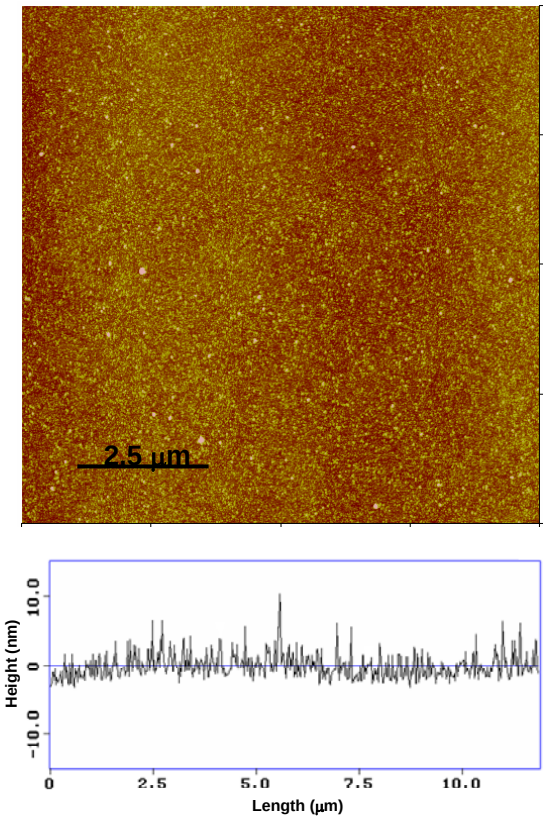

Figure 4.4. AFM image of a 10 µm by 10 µm section of a PSI monolayer film assembled using the vacuum approach with a diagonal line scan depicting the surface topology.

We have recently shown that $C_{22}SH$ will displace a thin, underlying SAM in areas that are not coated by PSI whereas the presence of PSI acts to block this displacement reaction.[8] As shown in Figure 4.5, $C_{22}SH$ displaces the TPDA-terminated SAM when PSI is not present, but does not adsorb when a PSI film is present on the surface. The ineffectiveness for $C_{22}SH$ to exchange away the TPDA SAM, coupled with the 67 ± 7 Å

thickness for the PSI film and the smooth nature of the film, indicates a dense monolayer of PSI on the surface of the electrode.

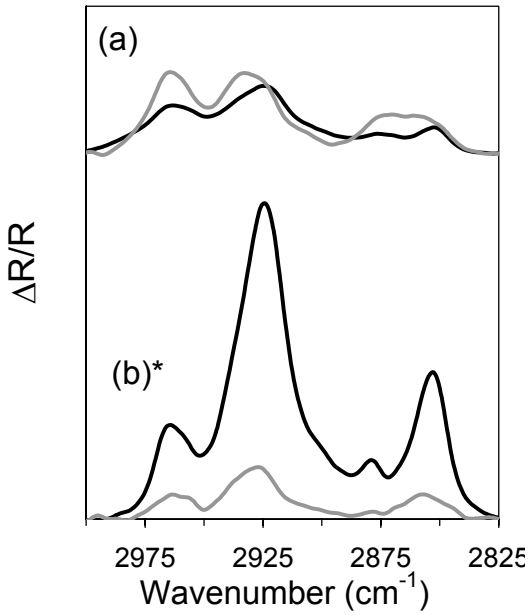

Figure 4.5. PM-IRRA spectra of a PSI monolayer prepared using the vacuum approach, (a), and a terephthaldialdehyde SAM (b) prior to (faded) and after (bold) exposure to $C_{22}SH$ for 2 h. *The PM-IRRA spectrum of the TPDA SAM prior to $C_{22}SH$ exposure (b, faded) has been magnified 10 fold to enable clearer comparison.

We used light-induced chronoamperometry with a custom 3-electrode electrochemical cell to characterize the photoelectrochemical activity and relative orientation of PSI films on gold electrodes. Upon adsorption, PSI can orient with its electron transfer vector directed away from the electrode surface (P700 proximal to the electrode), toward the electrode surface (F_B terminal acceptor proximal to the electrode), or in some random, non-specific orientation.[4] During irradiation by light, the gold electrode can donate electrons (cathodic current) to reduce the photooxidized $P700^+$ reaction centers located near the SAM/PSI interface, and the electrode can receive electrons (anodic current) from reduced F_B^- cofactors located near the SAM/PSI interface.

The net current induced by the light is a measure of the cathodic current minus the anodic current and is very sensitive to the average orientation of PSI. At the PSI/solution interface, electron mediators are required to maintain a steady flow of current by accepting electrons from F_B^- or donating electrons to $P700^+$ that are located near this interface. The electrolyte medium for this experiment contained 5 mM phosphate buffer, 100 mM NaCl, 250 μM 2,6 dichloroindophenol (DCIP), an electron acceptor compatible with the F_B site of PSI, and 5 mM sodium ascorbate (NaAs), an electron donor compatible with the P700 reaction center. Figure 4.6 displays the photo-induced amperometric responses of two different PSI films, one formed through the vacuum-assisted approach of Figure 2 for 30 min and one adsorbed from a ~1.9×10^{-5} M PSI solution for 30 min, with both using the TPDA attachment scheme (Figure 1).[17] The precipitated monolayer of PSI, prepared under vacuum, is ~75% denser (~70 Å vs ~40 Å thickness) by ellipsometry and draws ~10 times more current from the gold electrode than does the PSI film formed from traditional solution adsorption.

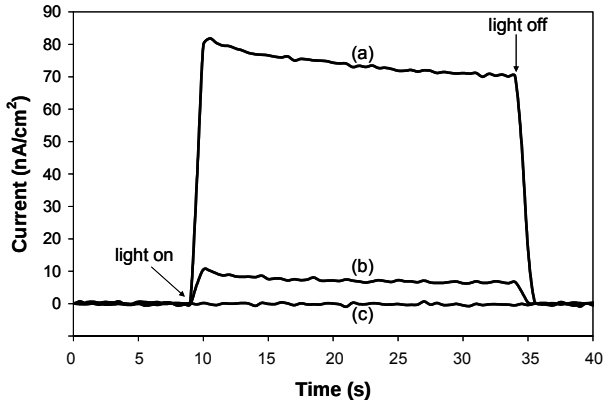

Figure 4.6. Chronoamperometry of PSI monolayers covalently bound to a TPDA-functionalized SAM by (a) vacuum-assisted assembly or (b) solution adsorption for 30 min. (c) Chronoamperometry of a TPDA-functionalized SAM without PSI.

The remarkably higher current for the vacuum approach may be related to a higher coverage of active and oriented PSI during the photoelectrochemical measurements. In this study, the electrodes were set to a potential of -0.11 V (vs. Ag/AgCl), at which the oxidation of F_B (E^0 = -0.787 V vs Ag/AgCl)[18] is more favorable than the reduction of $P700^+$ (E^0 = 0.313 V vs Ag/AgCl).[5] The observation of cathodic current in Figure 4.6 at this intermediate applied potential is consistent with an average orientation of PSI where P700 is near the electrode/SAM interface for facile reduction of $P700^+$ by gold.

To investigate whether adsorption of PSI from dilute solution precludes the formation of dense protein films, we exposed a TPDA-terminated SAM to the PSI solution for extended times. Assembly of PSI over these long periods of time (~50 h) using traditional solution adsorption produced films of similar thickness and photo-induced current to those of the vacuum approach under much shorter times (Figure 4.7a). Dense PSI monolayer films utilizing the TPDA attachment yield at least ~90 nA/cm^2 of photo-induced current for both vacuum-assisted assembly and solution adsorption. A sharp increase in yielded current occurs for both methods when the PSI monolayer approaches a density corresponding to at least a ~65 Å thickness on this TPDA monolayer (Figure 4.7c). We attribute this critical thickness to the related dense packing of the protein complex on the surface, which encourages preferential orientation of PSI and blocks access of reduced mediators to the gold surface to minimize anodic current. The critical thickness is achieved after ~40 h of solution adsorption and just 30 min using the vacuum approach, demonstrating that the vacuum-assisted assembly of PSI forms these requisitely dense PSI films ~80 times faster than solution adsorption.

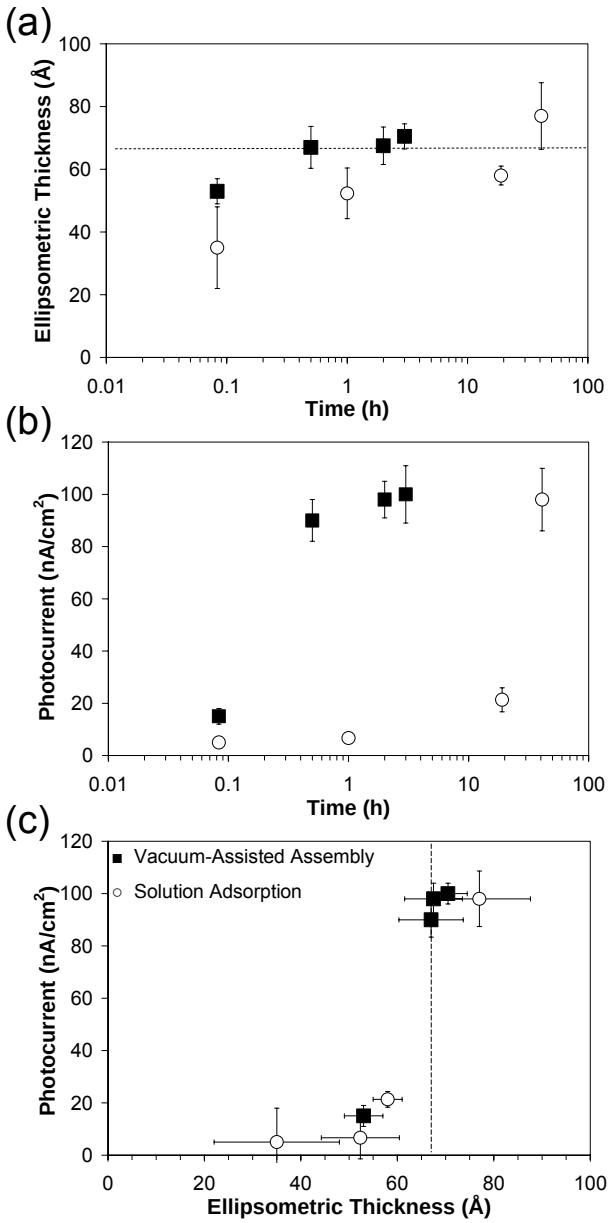

Figure 4.7. Time-dependence of (a) PSI film thickness by ellipsometry and (b) current density for vacuum-assisted assembly and solution adsorption of PSI. The dashed line in (a) represents a critical film thickness of ~67 Å, in which elevated photocurrents are observed. In (c), the critical film thickness is shown more clearly as the effect of film thickness on photocurrent is shown.

Vacuum-assisted assembly is not limited to the TPDA attachment strategy of Figure 4.1 and enables the formation of PSI monolayers on many SAMs, as well as direct adsorption onto the gold electrode (Table 4.1). The vacuum-assisted approach enables formation of PSI films on surfaces that previously promoted sparse or no PSI film

formation using traditional adsorption methods. For example, we previously reported that PSI does not assemble from solution onto CH_3-terminated SAMs due to mediating effects of the Triton X-100 surfactant with the low-energy surface.[6]

Table 4.1. A comparison between current and thickness produced from 30 min PSI adsorption via the vacuum approach and solution adsorption. *Denotes covalent attachment strategies.

	Vacuum-Assisted Assembly		Solution Adsorption	
Attachment	Average Current (nA/cm^2)	Average PSI Film Thickness (Å)	Average Current (nA/cm^2)	Average PSI Film Thickness (Å)
None	101 ± 11	72 ± 9	13 ± 7	44 ± 14
$HSC_7H_{14}CH_3$	31 ± 5	55 ± 13	0	0
$HSCH_2COOH$	26 ± 6	64 ± 7	4 ± 2	29 ± 14
$HSC_2H_4NH_2$	17 ± 9	62 ± 15	11 ± 3	52 ± 11
$HSCH_2CO$-NHS*	65 ± 34	71 ± 9	6 ± 3	34 ± 8
HSC_2H_4N-TPDA*	90 ± 8	67 ± 7	7 ± 4	35 ± 11

Using the vacuum approach, we can indeed form PSI layers on a CH_3-terminated SAM, albeit at lower densities than for the other surface compositions. The enhancement in photocurrent using vacuum-assisted assembly of PSI is greater than that of solution adsorption for every attachment strategy studied at the common time of 30 min. The vacuum approach accompanied by covalent attachment of PSI through TPDA or N-hydroxysuccinimidyl (NHS) termini or direct adsorption of PSI onto the gold electrode all enable consistently high PSI densities that again translate into high currents.

Conclusions

We have shown that a densely packed PSI monolayer of at least ~65 Å is required to obtain optimal solar conversion performance, and we have introduced a vacuum-assisted method for PSI adsorption that produces these requisitely dense, oriented

monolayers of PSI ~80 times faster than solution adsorption. This method also enables the assembly of PSI films onto surfaces that have previously resisted adsorption of this protein complex. The robustness and ease of this new assembly method should be easily adaptable to other biomimetic systems.

References

1. Lewis, N. S.; Nocera, D. G., Powering the Planet: Chemical Challenges in Solar Energy Utilization. *Proc. Nat. Acad. Sci.* USA **2006**, 103, 15729-15735.

2. Nelson, N.; Yocum, C. F., Structure and Function of Photosystems I and II. *Annu. Rev. Plant Biol.* **2006**, 57, 521-565.

3. Ben-Shem, A.; Frolov, F.; Nelson, N., Crystal structure of plant photosystem I. *Nature* **2003**, 426, 630-635.

4. Lee, I.; Lee, J. W.; Greenbaum, E. Biomolecular electronics: Vectorial arrays of photosynthetic reaction centers. *Phys. Rev. Lett.* **1997**, *79*, 3294-3297.

5. Ciobanu, M.; Kincaid, H. A.; Lo, V.; Dukes, A. D.; Jennings, G. K.; Cliffel, D. E., Electrochemistry and Photoelectrochemistry of Photosystem I Adsorbed on Hydroxyl-terminated Monolayers. *Journal of Electroanalytical Chemistry* **2007**, 599, 72-78.

6. Ko, B. S.; Babcock, B.; Jennings, G. K.; Tilden, S. G.; Peterson, R. R.; Cliffel, D., Effect of Surface Composition on the Adsorption of Photosystem I onto Alkanethiolate Self-Assembled Monolayers on Gold. *Langmuir* **2004**, 20, 4033-4038.

7. Terasaki, N.; Yamamoto, N.; Hiraga, T.; Sato, I.; Inoue, Y.; Yamada, S., Fabrication of Novel Photosystem I - Gold Nanoparticle Hybrids and their Photocurrent Enhancement. *Thin Solid Films* **2006**, 153-156.

8. Kincaid, H. A.; Niedringhaus, T.; Ciobanu, M.; Cliffel, D. E.; Jennings, G. K., Etrapment of Photosystem I within Self-Assembled Films. *Langmuir* **2006**, 22, 6114-8120.

9. Kievit, O.; Brudvig, G. W., Direct electrochemistry of photosytem I. *Journal of Electroanalytical Chemistry* **2001**, 497, 139-149.

10. Lee, I.; Lee, J. W.; Stubna, A.; Greenbaum, E. *Journal of Physical Chemistry B* **2000**, *104*, 2439-2443.

11. Das, R.; Kiley, P. J.; Segal, M.; Norville, J.; Yu, A. A.; Wang, L.; Trammell, S. A.; Reddick, L. E.; Kumar, R.; Stellacci, F.; Lebedev, N.; Schnur, J.; Bruce, B. D.; Zhang, S.; Baldo, M., Integration of Photosynthetic Protein Molecular Complexes in a Solid-State Electronic Device. *Nano Letters* **2004**, 4, 1079-1083.

12. Frolov, L.; Rosenwaks, Y.; Carmeli, C.; Carmeli, I., Fabrication of a Photoelectric Device by Direct Chemical Binding of Photosynthetic Reaction Center Protein to Metal Surfaces. *Advanced Materials* **2005**, 17, 2434-2437.

13. Carmeli, I.; Frolov, L.; Carmeli, C.; Richter, S., Photovoltaic Activity of Photosystem I - Based Self-Assembled Monolayer. *Journal of American Chemical Society* **2007**, 129, 12352-12353.

14. Chang, M. S.; Ji, Q.; Zhang, J.; El-Shourbagy, T. A., Historical review of sample preparation for chromatographic bioanalysis: Pros and cons. *Drug Development Research* **2007**, 68, 107-133.

15. Rozkiewicz, D. I.; Ravoo, B. J.; Reinhoudt, D. N., Reversible Covalent Patterning of Self-Assembled Monolayers on Gold and Silicon Oxide Surfaces. *Langmuir* **2005**, 21, 6337-6343.

16. Amunts, A.; Drory, O.; Nelson, N., The structure of a plant photosystem I supercomplex at 3.4 angstrom resolution. *Nature* **2007**, 447, 58-63.

17. The observed photocurrent decay in Figure 4.4 is attributed to the depletion of mediator concetration near the electrode surface.

18. He, W. Z.; Malkin, R. "Photosystems I and II". In *Photosynthesis: A Comprehensive Treatise*; Raghavendra, A. S., Ed.; Cambridge University Press: Cambridge, 1998. p. 29-43.

CHAPTER V

RAPID ASSEMBLY OF PHOTOSYSTEM I MULTILAYER FILMS ON GOLD ELECTRODES

Introduction

The remarkable efficiency and reducing power of PSI has led to the development of PSI-modified electrodes to convert solar energy for use in biocatalysis[1-4] or electrochemical power generation. In order to use PSI towards these means, it is extracted from its natural environment and attached to various electrode substrates. We[5-9] and others[10-14] have demonstrated the adsorption of PSI monolayers onto electrodes using self-assembled monolayers (SAMs). Greenbaum and co-workers described the orientation of PSI on carboxylic-, hydroxyl-, and amine-terminated surfaces and that hydroxyl surfaces preferentially orient the protein with the P700 center proximinal to the surface.[13] Terasaki et al. used a sulfonic-acid-terminated SAM to adsorb a monolayer PSI film with the F_B site close to the surface.[14] However, these methods do not provide a direct attachment of PSI to the electrode. To covalently bind PSI to an electrode surface Das et al.[11] and Carmeli et al.[10] modified a PSI subunit with cysteine mutations to directly bind the protein to a gold electrode. In the previous chapter we discussed a new, facile method for the preparation of monolayer PSI films that combines the convenience of SAMs and the stability afforded through covalent attachment. We determined that a critical density of PSI was required on the electrode surface in order to achieve appreciable photocurrent production.

These approaches are limited due to only a monolayer of PSI being used. In its natural environment, PSI resides within the lipid bylayer of thylakoid stacks located in

the chloroplasts of the cell. Since, the thylakoid membranes are in stacks, each plant cell is able to absorb more light. Thus, translating this principle to PSI-modified electrodes, multiple layers of PSI would be able to convert more light into chemical or electrical energy than monolayer PSI films. Recently, Carmeli and Frolov described a method in which they prepared a multilayer PSI film through layer-by-layer deposition.[15] They mutated PSI to include a cysteine moiety to preferentially bind the protein to the electrode surface. Then depositing Pt to the F_B site, they repeated PSI monolayer deposition taking advantage of sulfur's affinity for noble metals, creating stacked layers of PSI. This technique is tedious and cumbersome, requiring many steps to create the multilayered protein film. Last chapter, we described a technique in which we were able to form monolayer PSI films ~80 times faster than pre-existing methods.[7] Here, we extend this method to the formation of multilayer PSI films and compare their electrochemical performance to that of PSI monolayer films.

In this manuscript, we describe the preparation of multilayer PSI films using the vacuum-assisted assembly as depicted in Figure 5.1(ii). This simple method enables the formation of active micron-thick PSI films in as little as 30 min. We characterize the films using light-induced chronoamperometry to determine the current produced from PSI-modified electrodes upon irradiation. Comparisons between the performance of multilayer and monolayer PSI films are also discussed.

Experimental Procedures

Preparation of SAMs

Gold-coated silicon wafers were prepared by first evaporating a 100 Å layer of chromium followed by ~1250 Å of gold at a base pressure of 5 x 10^{-6} torr. The SAMs were prepared by immersing 1 cm by 3 cm gold-coated silicon samples into 1 mM 2-aminoethanethiol solutions in ethanol for 24-48 h at room temperature. The amine-terminated SAMs were further modified by immersing the samples in 1 mM TPDA aqueous solution for 1 h. The samples were rinsed with ethanol and water and dried under a stream of nitrogen following SAM formation and modification.

Preparation of PSI Films

An aqueous solution of PSI (~1.9 ·10^{-5} mol/L) containing 0.2 M phosphate buffer and 0.9 mM TritonX-100 was deposited onto the TPDA modified SAM and placed under vacuum (~30 mTorr) for 30 min. A thick layer of PSI, salt, and Triton X-100 is formed upon water removal as shown in Figure 5.1. A dense monolayer of PSI is obtained by thoroughly rinsing with water, Figure 5.1(i), as previously described.[7] A dense multi-layered PSI film can be obtained by first placing the samples in an ethanol bath prior to rinsing with water, Figure 5.1(ii). The ethanol bath enables the solvation of TritonX-100 leaving the salt and PSI film on the surface. Varying thickness of multilayer PSI films were achieved by using different volumetric amounts, 50 μL – 200 μL, of PSI solution during the vacuum-assisted depositions.

Results and Discussion

Multilayered Photosystem I films were prepared on gold electrodes utilizing a vacuum-assisted deposition we previously reported[7] as depicted in Figure 5.1(ii). We

exposed an amine-terminated SAM, prepared from adsorption of 2-aminoethanethiol onto gold, to a 1 mM solution of terephthaldialdehyde (TPDA) in ethanol for 1 h. The TPDA-capped SAM can bind lysine residues of proteins through covalent imine bonds.[16] An aqueous solution of PSI (□1.9 × 10-5 mol/L) containing 0.2 M phosphate buffer and 0.9 mM Triton X-100 was then deposited onto the TPDA-modified SAM and placed under vacuum (□30 mTorr) for 30 min. As the water evaporates from the film, PSI aggregates form and crash out of solution since PSI is by far the least soluble component in this aqueous buffer solution and bind to the TPDA-covered surface. A thick film (□20 μm) of PSI, salt, and Triton X-100 is precipitated upon complete removal of the water. Rinsing with water, Figure 5.1(i), leaves a PSI monolayer film on the surface removing excess PSI, salt and TritonX-100 residue.[7]

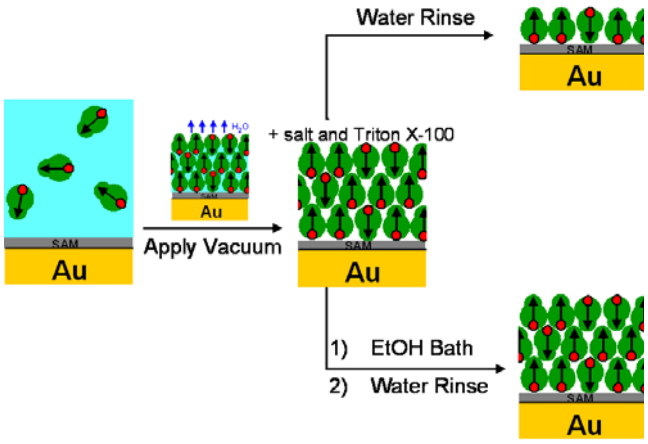

Figure 5.1. Vacuum-assisted approach for rapidly forming dense (i) PSI monolayers and (ii) PSI multilayers.

However, a multilayered PSI film can be formed by selectively removing the surfactant that stabilizes PSI in the aqueous buffer using an ethanol bath prior to rinsing with water.

Without the surfactant, PSI is less soluble in water, thus upon rinsing, Figure 5.1(ii) a multilayered PSI film remains on the surface. Figure 5.2 displays a cross-sectional scanning electron micrograph of a multilayered PSI film. As can be seen, a multilayered PSI film prepared using the method shown in Figure 5.1 is typically ~1 μm thick. The bright layer, ~125 nm thick, underneath the protein film, is the gold electrode on which the PSI film is deposited.

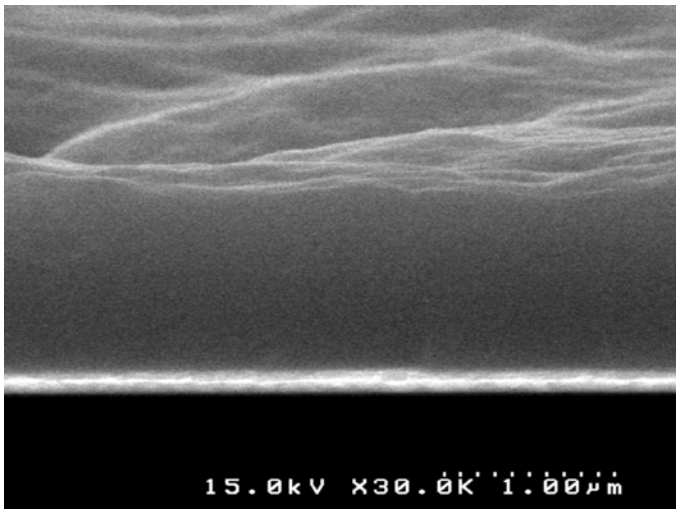

Figure 5.2. Cross-sectional scanning electron micrograph of a PSI multilayer.

Figure 5.3 displays the RAIR spectrum of a PSI multilayer film. For a PSI film, two significant vibrational bands appear in the mid-IR region corresponding to amide stretching: Amide I (1600-1700 cm^{-1}) and Amide II (1500-1600 cm^{-1}). The secondary structure of PSI can give insight into its activity and can be determined by further examination of the Amide I absorption peak. The IR absorption in the Amide I region can be assigned to various secondary structural moieties in a protein as shown in Table 3.2.[17-27] Thus, PSI denaturation can be monitored by the shape of the Amide I absorption peak in the RAIR spectrum. As can be seen in Figure 5.3, the multilayer has strong

Amide I and Amide II absorption peaks at ~1666 cm^{-1} and ~1548 cm^{-1}, suggesting that the PSI film is still functional and warrants electrochemical characterization.

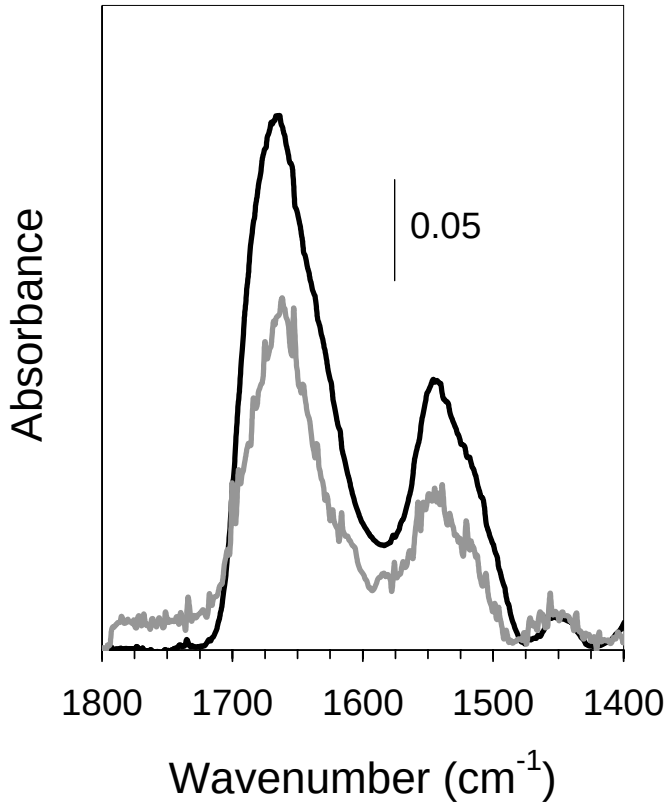

Figure 5.3. Reflectance absorption infrared spectrum of a multilayer PSI film (black line) and PSI monolayer film enhanced 10 fold (gray line).

We used light-induced chronoamperometry with a custom 3-electrode electrochemical cell to determine the photoelectrochemical activity of PSI films on gold electrodes. Upon adsorption, PSI can orient with its electron transfer vector directed away from the electrode surface (P700 proximal to the electrode), toward the electrode surface (F_B terminal acceptor proximal to the electrode), or in some random, non-specific orientation.[13] During irradiation by light, the gold electrode can donate electrons (cathodic current) to reduce the photooxidized $P700^+$ reaction centers or oxidized

mediator located near the SAM/PSI interface, and the electrode can receive electrons (anodic current) from reduced F_B^- cofactors or reduced mediator located near the SAM/PSI interface. The net current induced by the light is a measure of the cathodic current minus the anodic current. At the PSI/solution interface, electron mediators are required to maintain a steady flow of current by accepting electrons from F_B^- or donating electrons to $P700^+$ that are located near this interface. The electrolyte medium for this experiment contained 5 mM phosphate buffer, 100 mM NaCl, 250 μM 2,6 dichloroindophenol (DCIP), an electron acceptor compatible with the F_B site of PSI, and 5 mM sodium ascorbate (NaAsc), an electron donor compatible with the P700 reaction center. We previously reported the E_o of the P700 reaction center as +0.313 V vs. Ag/AgCl for a monolayer of PSI adsorbed onto a Au/S$(CH_2)_6$OH film,[6] whereas the E_o of F_B is ~ -0.787 V vs. Ag/AgCl, respectively.[28] Therefore, in order to favor reduction of the $P700^+$ reaction center, the cell potential was set to approximately -0.11 V vs. Ag/AgCl.

Figure 5.4 displays the photo-induced amperometric response of a multilayer PSI film (curve (a)) and a monolayer PSI film (curve (b)) adsorbed from a ~1.9×10^{-5} M PSI solution using the scheme shown in Figure 5.1. For both of these systems only the first layer of PSI is interfaced with the gold electrode, yet upon exposure to light, we observed a dramatic increase, ~ 20 fold, in photocurrent production by the multilayer PSI film, ~ 1800 nA/cm^2, over that of a PSI monolayer film, ~80 nA/cm^2. This suggests that the multilayer assembly provides additional conduits to the reduction of $P700^+$ reaction centers in PSI complexes proximal to the electrode surface.

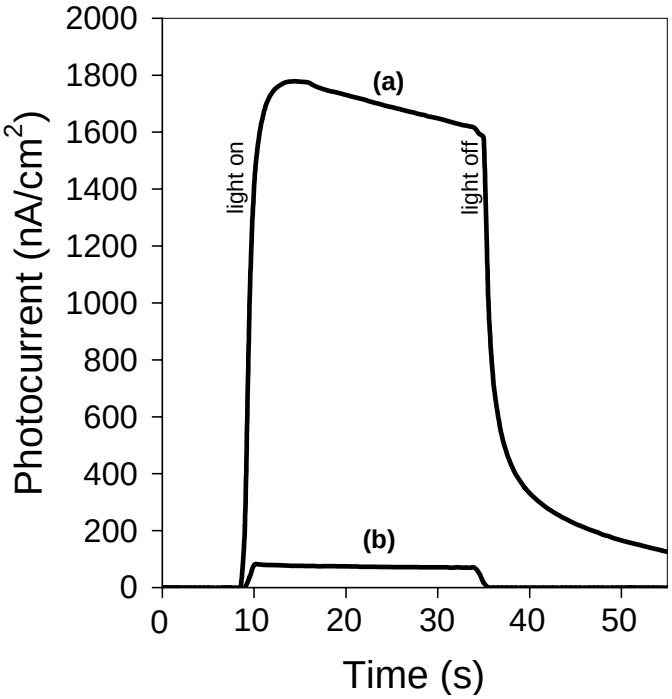

Figure 5.4. Photochronoamperometric response of a (a) PSI multilayer film and (b) PSI monolayer film covalently bound to a TPDA-functionalized SAM upon exposure to light.

The multilayer of PSI could contribute to enhanced photocurrent production in two ways: 1) the electron mediators enable non-"wired" PSI to contribute energy to the electrochemical system and 2) the electron mediators partition into the PSI film, thus increasing the concentration of mediator able to facilitate charge transfer throughout the PSI film and near the electrode interface. Recently, we demonstrated that the reduction and oxidation of $P700^+$ and F_B^- within a PSI multilayer film, respectively, changes the concentration of mediator near the working electrode.[29] The change in mediator concentration induced by the PSI multilayer film at the working electrode surface can be attributed to the conversion of oxidized electrochemical mediators to their reduced state by PSI complexes in non-bound layers, which acts to maintain a higher concentration of the reduced mediator species in the vicinity of the electrode. To complete the circuit of the electrochemical cell, every $P700^+$ center reduced must be accompanied by the

oxidation of an electron mediator at the counter electrode. Thus, the concentration gradient induced from the reduction of electrochemical mediators within the PSI multilayer film facilitates the transport of this reduced mediator to the counter electrode enabling the production of greater cathodic currents than in a PSI monolayer film.

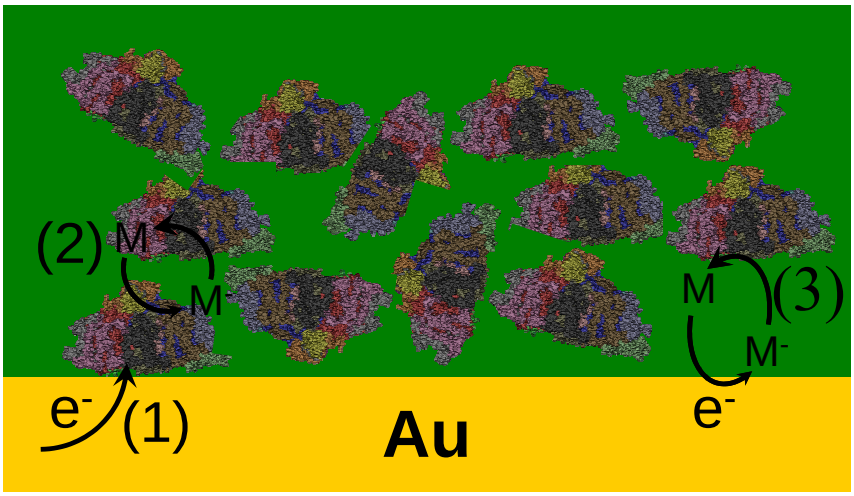

Figure 5.5. Schematic of possible avenues of cathodic current production in a multilayer PSI film. (1) Direct electron transfer from the electrode to reduce $P700^+$. (2) Rapid F_B- turnover through subsequent mediator oxidation and reduction facilitating the regeneration of $P700^+$ from the electrode. (3) Subsequent electron mediator reduction at the electrode surface after oxidation at $P700^+$ centers within the multilayer.

To further illustrate the impact of the PSI multilayer on photocurrent generation, Figure 5.5 displays a schematic depicting three methods that the multi-layered PSI-modified electrode produces cathodic current upon exposure to light. Figure 5.5(1) illustrates the direct electron transfer from the electrode to "wired" PSI complexes to regenerate $P700^+$ centers, which also occurs in PSI monolayer films. However, the $P700^+$ centers within the upper layers must also be regenerated to continue converting photons into electrochemical energy. Since they are not directly connected to the electrode, reduction from the surface is not possible as electron tunneling ceases beyond a few nm (the length scale of a single PSI complex).[30] Thus, electron mediators are able to reduce

the $P700^+$ sites, regenerating them for further activity. Figure 5.5(2) illustrates the regeneration of a $P700^+$ center and subsequent oxidation of a F_B site from the "wired" monolayer. This series of electron transfer would enable the rapid turn-over of PSI complexes anchored to the electrode, thereby, increasing the cathodic current production capacity of the interfacial layer of PSI. Similarly, electron mediators that regenerate $P700^+$ centers can then accept electrons from the working electrode, producing cathodic current, illustrated in Figure 5.5(3). The enhanced concentration gradient of oxidized mediator is not feasible in a PSI monolayer system and thus contributes to the photocurrent enhancement shown in PSI multilayer films over that of PSI monolayer films.

As noted previously, the photocurrent generation afforded by the electron mediators in multilayer PSI films is also due to preferential partitioning of the mediators into the PSI film over that of solution. The electron mediators used in our experiments are hydrophobic and thus, we expect them to preferentially partition into the PSI multilayer film from solution. To confirm that DCIP and NaAsc partition into the PSI

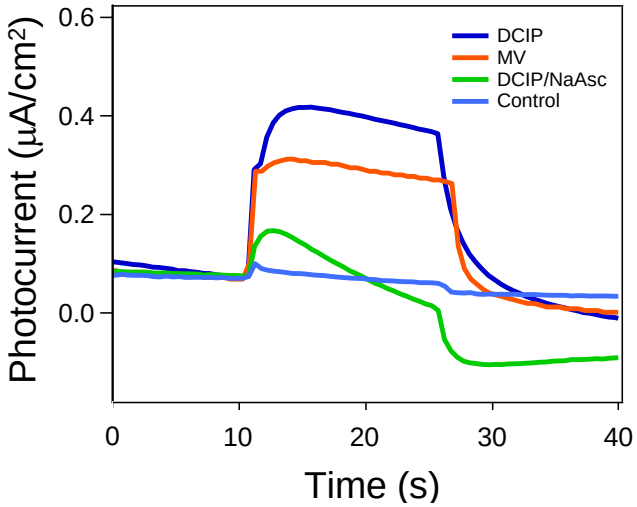

Figure 5.6. Photochronoamperometry, in 100 mM NaCl and 50 mM PBS solution (aq), of PSI multilayer films that have been exposed to 250 μM of the indicated electrolyte solution. The control indicates the response of a PSI multilayer film that was not exposed to any electrolyte solution.

film from bulk solution, we modified the preparation of the multilayer PSI films. Upon forming a PSI multilayer film using the scheme shown in Figure 5.1(ii), the PSI films were exposed to 250 μM solutions (aq) of methyl viologen (MV), DCIP, or DCIP/NaAsc for 30 min., rinsed with water, and dried with N_2. The performance of these films was assessed using photochronoamperometry with no electron transfer mediators in solution during the experiment, shown in Figure 5.6. Any photocurrent response is indicative of electron mediator having partitioned into the PSI multilayer film, thus facilitating electron transfer during the subsequent photochronoamperometric measurements. As a control, we measured the photocurrent response of a PSI film that was not exposed to any electron transfer mediators. As can be seen in Figure 5.6, the PSI multilayer films exposed to mediator solutions prior to the photocurrent measurement exhibit significant photochronoamperometric response upon irradiation with light. Thus, the PSI multilayer film acts to greatly increase the concentration of mediator near the electrode surface, enabling a larger gradient of mediator to enhance transport to the anode and elevate photocurrents.

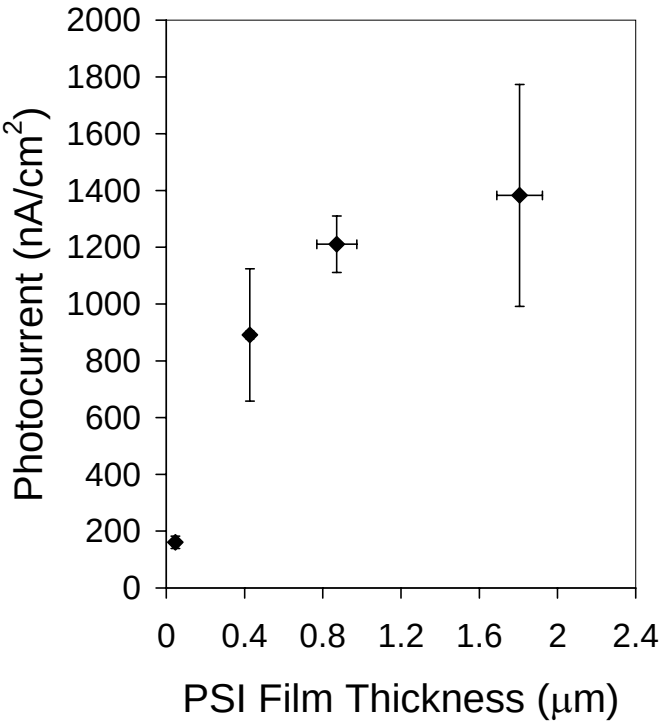

Figure 5.7. The photocurrent density of multilayer PSI films as a function of film thickness.

Figure 5.7 displays the impact of PSI film thickness on photocurrent generation. As can be seen, the first few additional layers of PSI complexes increases the photocurrent production linearly with a ~4 fold enhancement in thickness yielding a ~ 4 fold response in photocurrent. However, this trend does not continue as the PSI film thickness increases. For PSI films > 1.2 microns thick, the impact of additional PSI layers is not as effective in generating photocurrent. This is consistent with the electron transfer mechanism previously described as the electrochemical mediator must diffuse farther as the PSI film becomes thicker.

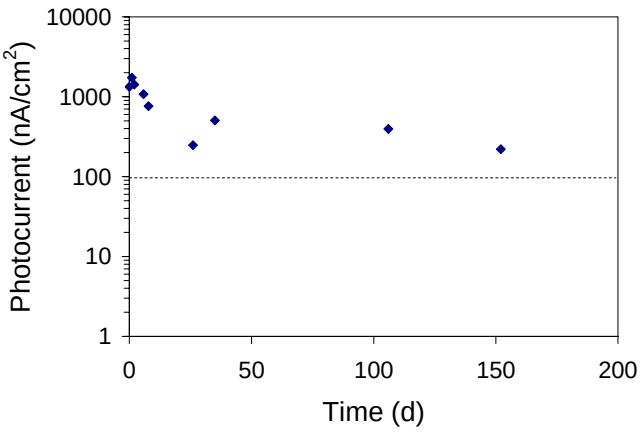

Figure 5.8. The photochronoamperometric response of a multilayer PSI film over time. The PSI film was stored in PBS, pH 7, in between measurements.

An additional benefit to preparing multilayered PSI films is the enhanced stability of the "wired" PSI monolayer. Previously, we developed a unique approach to insulate and stabilize adsorbed PSI complexes using long-chain alkanethiols to mimic the environment of the thylakoid membrane of green plants.[31] Similarly, we suggest that the additional PSI layers insulate and stabilize the "wired" PSI monolayer through intermolecular protein/protein interactions. Figure 5.8 displays the photocurrent response of a multilayered PSI film exposed to light at various time intervals. As can be seen, the PSI multilayer film produces at least ~250 nA/cm^2 of photocurrent over a 5 month time-span. The photocurrent generated by the multilayer film remained greater than the current produced by a freshly-prepared PSI monolayer film (~100 nA/cm^2), indicated by the dashed line in Figure 5.8. We attribute the decrease from the initial photocurrent production to loss of PSI layers during rinsing cycles between measurements, thereby reducing the amount of active protein on the surface. We recently reported a photoelectrochemical cell comprised of a multilayer-PSI modified electrode that has been

stable for over 1 year producing photocurrent and open circuit potentials comparable to initial values.[29]

Conclusion

We have demonstrated the facile preparation of multilayer Photosystem I films via vacuum-assisted assembly that generate ~20 fold greater light-induced current than monolayer PSI films upon light irradiation. The electron transfer mediators play an important role in the photocurrent enhancement observed in the multilayer films. The electron mediators preferentially partition into the multilayer PSI film, increasing the concentration of redox couples near the electrode surface over that of the bulk electrolyte solution. The electron mediators also enable non-"wired" PSI to contribute energy to the electrochemical system by providing an electron transfer pathway to the working electrode.

References

1. Winkler, M.; Heil, B.; Happe, T., Isolation and molecular characterization of the [Fe]-hydrogenase from the unicellular green alga Chlorella fusca. *Biochimica Et Biophysica Acta-Gene Structure and Expression* **2002,** 1576, 330-334.

2. Roessler, P. G.; Lien, S., Purification of hydrogenase from chlamydomonas-reinhardtii. *Plant Physiology* **1984,** 75, 705-709.

3. Grimme, R. A.; Lubner, C. E.; Bryant, D. A.; Golbeck, J. H., Photosystem I/molecular wire/metal nanoparticle bioconjugates for the photocatalytic production of H-2. *Journal of the American Chemical Society* **2008,** 130, 6308-6309.

4. Millsaps, J. F.; Bruce, B. D.; Lee, J. W.; Greenbaum, E., Nanoscale photosynthesis: Photocatalytic production of hydrogen by platinized photosystem I reaction centers. *Photochemistry and Photobiology* **2001,** 73, 630-635.

5. Ciobanu, M.; Kincaid, H. A.; Jennings, G. K.; Cliffel, D., Directed Adsorption of Photosystem I on Micropatterned Surfaces. *Langmuir* **2005,** 21, 692-698.

6. Ciobanu, M.; Kincaid, H. A.; Lo, V.; Dukes, A. D.; Jennings, G. K.; Cliffel, D. E., Electrochemistry and Photoelectrochemistry of Photosystem I Adsorbed on Hydroxyl-terminated Monolayers. *Journal of Electroanalytical Chemistry* **2007,** 599, 72-78.

7. Faulkner, C. J.; Lees, S.; Ciesielski, P. N.; Cliffel, D. E.; Jennings, G. K., Rapid assembly of photosystem I monolayers on gold electrodes. *Langmuir* **2008,** 24, 8409-8412.

8. Kincaid, H. A.; Niedringhaus, T.; Ciobanu, M.; Cliffel, D. E.; Jennings, G. K., Etrapment of Photosystem I within Self-Assembled Films. *Langmuir* **2006,** 22, 6114-8120.

9. Ko, B. S.; Babcock, B.; Jennings, G. K.; Tilden, S. G.; Peterson, R. R.; Cliffel, D., Effect of Surface Composition on the Adsorption of Photosystem I onto Alkanethiolate Self-Assembled Monolayers on Gold. *Langmuir* **2004,** 20, 4033-4038.

10. Carmeli, I.; Frolov, L.; Carmeli, C.; Richter, S., Photovoltaic Activity of Photosystem I - Based Self-Assembled Monolayer. *Journal of American Chemical Society* **2007,** 129, 12352-12353.

11. Das, R.; Kiley, P. J.; Segal, M.; Norville, J.; Yu, A. A.; Wang, L.; Trammell, S. A.; Reddick, L. E.; Kumar, R.; Stellacci, F.; Lebedev, N.; Schnur, J.; Bruce, B. D.; Zhang, S.; Baldo, M., Integration of Photosynthetic Protein Molecular Complexes in a Solid-State Electronic Device. *Nano Letters* **2004,** 4, 1079-1083.

12. Frolov, L.; Rosenwaks, Y.; Carmeli, C.; Carmeli, I., Fabrication of a Photoelectric Device by Direct Chemical Binding of Photosynthetic Reaction Center Protein to Metal Surfaces. *Advanced Materials* **2005,** 17, 2434-2437.

13. Lee, I.; Lee, J. W.; Greenbaum, E., Biomolecular electronics: vectorial arrays of photosynthetic reaction centers. *Phys. Rev. Lett.* **1997,** 79, 3294-3297.

14. Terasaki, N.; Yamamoto, N.; Hiraga, T.; Sato, I.; Inoue, Y.; Yamada, S., Fabrication of Novel Photosystem I - Gold Nanoparticle Hybrids and their Photocurrent Enhancement. *Thin Solid Films* **2006**, 153-156.

15. Frolov, L.; Wilner, O.; Carmeli, C.; Carmeli, I., Fabrication of oriented multilayers of photosystem I proteins on solid surfaces by auto-metallization. *Advanced Materials* **2008,** 20, 263-266.

16. Rozkiewicz, D. I.; Ravoo, B. J.; Reinhoudt, D. N., Reversible Covalent Patterning of Self-Assembled Monolayers on Gold and Silicon Oxide Surfaces. *Langmuir* **2005,** 21, 6337-6343.

17. Arrondo, J. L.; Goni, F. M., Structure and dynamics of membrane proteins as studied by infrared spectroscopy. *Progress in Biophysiscs and Molecular Biology* **1999,** 72, 367-405.

18. Fu, K.; Griebenow, K.; Hsieh, L.; Klibanov, A. M.; Langer, R., FTIR characterization of the secondary structure of proeins encapsulated within PLGA microspheres. *Journal of Controlled Release* **1999,** 58, 357-366.

19. Kota, Z.; Szalontai, B.; Droppa, M.; Horvath, G.; Pali, T., Fourier transform infrared and electron paramagnetic resonance spectroscopic studies of thylakoid membranes. *Journal of Molecular Structure* **1999,** 481, 395-400.

20. Khurana, R.; Fink, A. L., Do Parallel b-helix Proteins have a Unique Fourier Transform Infrared Spectrum? *Biophysical Journal* **2000,** 78, 994 - 1000.

21. Guiomar, A. J.; Guthrie, J. T.; Evans, S. D., Use of Mixed Monolayers in a Study of the Effect of the Microenvironment on Immobilized Glucose Oxidase. *Langmuir* **1999,** 15, 1198-1207.

22. Gilbert, S. M.; Wellner, N.; Belton, P. S.; Greenfield, J. A.; Siligardi, G.; Shewry, P. R.; Tatham, A. S., Expression and characterization of a highly repetitive peptide derived from wheat seed storage protein. *Biochimica Et Biophysica Acta* **2000,** 1479, 135-146.

23. Seshadri, S.; Khurana, R.; Fink, A. L., Fourier Transform Infrared Spectroscopy in Analysis of Protein Deposits. *Methods in Enzymology* **1999,** 309, 559-576.

24. Krueger, J. K.; Gallagher, S. C.; Wang, C. L.; Trewhalla, J., Calmodulin Remains Extended upon Binding to Smooth Muscle Caldesmon: A Combined Small-Angle Scattering and Fourier Transform Infrared Spectroscopy Study. *Biochemistry* **2000,** 39, (3979-3987).

25. Ruan, X.; Wei, J.; Xu, Q.; Wang, J.; Gong, Y.; Zhang, X.; Kuang, T.; Zhao, N., Comparison of the effects of Triton X-100 treatment on the protein secondary structure of Photosystem I and Photosystem II studied by FTIR spectroscopy. *Journal of Molecular Structure* **2000,** 525, 97-106.

26. Zhang, H.; Yamamoto, Y.; Ishikawa, Y.; Carpentier, R., Characterization of the secondary structure and thermostabiliy of the extrinsic 16 kilodalton protein of spinach photosystem II by fourier transform infrared spectroscopy. *Journal of Molecular Structure* **1999,** 513, 127-132.

27. Heimburg, T.; Schunemann, J.; Wever, K.; Geisler, N., FTIR-Spectroscopy of Multistranded Coiled Coil Proteins. *Biochemistry* **1999,** 38, 12727-12734.

28. He, W. Z.; Malkin, R., Photosystems I and II. In *Photosynthesis: A Comprehensive Treatise*, Raghavendra, A. S., Ed. Cambridge University Press: Cambridge, 1998; pp 29-43.

29. Ciesielski, P. N.; Hijazi, F. M.; Scott, A. M.; Faulkner, C. J.; Beard, L.; Emmett, K.; Cliffel, D.; Jennings, G. K., Photosystem I-based biohybrid photoeelctrochemical cells. *under review.*.

30. Nelson, N.; Yocum, C. F., Structure and Function of Photosystems I and II. *Annu. Rev. Plant Biol.* **2006,** 57, 521-565.

31. Kincaid, H. A.; Niedrinhaus, T.; Ciobanu, M.; Cliffel, D. E.; Jennings, G. K., Entrapment of Photosystem I within Self-Assembled Films. *Langmuir* **2006,** 22, 8114-8120.

CHAPTER VI

SURFACE-INITIATED POLYMERIZATION OF 5-(PERFLUORO-N-ALKYL)NORBORNENES FROM GOLD SUBSTRATES

Introduction

Due to their low critical surface energy,[1] dielectric constant,[2] and chemical inertness,[3] fluorinated polymers are used for a wide range of applications including protective coatings, biomaterials,[4] membranes,[5] and microelectronics.[6] Recently, more attention has been given to partially perfluorinated polymers because of concerns over the safety and processability of perfluorinated polymers. Partially fluorinated polymers are advantageous over perfluorinated polymers as the desired interfacial and surface properties of the fluorocarbon moiety can be achieved, and in many cases, surpassed, using safer, simpler, and less expensive methods.

Generally, fluorinated polymers are deposited onto surfaces via spin-coating,[7] dip-coating,[8] solution-casting[9], or chemical adsorption.[10] In the case of spin-coating and solution-casting, conformal polymer film coatings are possible on planar surfaces. However, these methods do not provide a direct attachment of the polymer to the surface, nor can they be applied to non-planar geometries. Chemical adsorption yields non-conformal, low density polymer films due to steric and diffusional constraints of untethered polymer segments.[10]

Surface-initiated polymerizations (SIP) enable controlled growth of polymer chains that are directly attached to a surface and are capable of producing conformal thin films on surfaces of many geometries.[11] Generally, surface-initiated polymer films

obtain their fluorocarbon functionality through post-processing methods. Our group[12] has modified poly(hydroxyethylmethacrylate) (PHEMA) films with perfluorinated acid chlorides to obtain fluorocarbon functionality throughout the film and achieve critical surface energies as low as 9 mN/m. Bruening, Baker, and co-workers have used post-fluorination of PHEMA to prepare membranes capable of high CO_2 permeability and CO_2/CH_4 selectivity.[5]

The ability to achieve partially perfluorinated polymer films directly via surface-initiated polymerization would eliminate the need for post-processing methods mentioned in the examples above. However, few partially fluorinated polymers have been grown directly from a surface using surface-initiated polymerizations. A notable example includes the work of Ruhe and co-workers, who polymerized a fluorinated acrylate using controlled radical polymerization methods.[13] They were able to achieve dense films; however, the polymerization required 4 h and 27 h to achieve films ~20 nm and ~70 nm thick, respectively. In general, controlled radical polymerization methods require hours to yield coherent polymer films less than 100 nm thick.[14, 15] An exception is water-accelerated atom transfer polymerization (ATRP), which exhibits much faster kinetics enabling the growth of thicker polymer films, > 100 nm.[16-18] However, monomers must be water soluble, thus precluding the use of most fluorinated monomers in water-accelerated ATRP.

In this manuscript, we describe the preparation of partially fluorinated polymer films using surface-initiated ring-opening metathesis polymerizations (SI-ROMP). SI-ROMP is attractive for its mild reaction conditions and rapid kinetics to enable films with thicknesses of several nm up to a few μm.[2, 19] The predominate ROMP monomers

studied in surface-initiated cases have been norbornene and its functional derivatives[2, 20-23] due to their high reactivity in ROMP and the ease of synthesizing functionalized monomers. Here, we have synthesized 5-(perfluoro-n-alkyl)nobornenes (NBFn) with fluorocarbon chain lengths (n) of 4, 6, 8, and 10 and polymerized them from surfaces using Grubbs 2nd generation catalyst (Figure 1). Our approach combines the advantages of SI-ROMP with the technological importance of partially fluorinated films to grow tunable films under ambient conditions.[24] We show that these films grow rapidly, are far more stable than polynorbornene films, and yield critical surface tensions that are dependent on the fluorocarbon chain length.

Experimental Procedures

Synthesis of NBFn

Four monomers were synthesized utilizing a Diels-Alder reaction described by Perez et al.[25]: 5-(perfluorobutyl)norbornene (NBF4), 5-(perfluorohexyl)norbornene (NBF6), 5-(perfluorooctyl)norbornene (NBF8), and 5-(perfluorodecyl)norbornene (NBF10), with ~47%, 48%, 47%, and 50% yield, respectively. Briefly, a Parr Instruments high pressure reaction vessel was charged with 1:1 molar ratios of the 1H,1H,2H-perfluoro-1-alkene and dicyclopentadiene and 0.03 mol fraction of hydroquinone, as a quenching agent. The reaction was held at 170 °C for 72 h. Monomers were purified by vacuum distillation. A DRX-400 Bruker NMR spectrometer equipped with a 9.4 Tesla Oxford magnet was used to confirm the chemical structure and composition of the synthesized 5-(perfluoro-n-alkyl)norbornenes (NBFn). The reactions yielded ~3:1 ratio of endo- to exo-isomers of the NBFn as determined by ^{13}C NMR. NMR spectra were collected and are consistent

with those reported by Perez et al.[25] A more detailed discussion of the NMR spectra is given in Chapter III.

Polymerization

Gold substrates were placed in a 1.0 mM ethanolic solution of 4-mercapto-1-butanol for at least 1 h to yield a hydroxyl-terminated self-assembled monolayer (SAM). The films were rinsed in ethanol and dried in a stream of nitrogen. Exposure of the SAM to a 5 mM solution of trans-3,6-endo-methylene-1,2,3,6-tetrahydrophthaloyl chloride in dichloromethane for 30 min yields the acylation product of a surface-tethered norbornenyl group.[26] The samples were rinsed with DCM, ethanol, and dried in a stream of N_2. The norbornenyl decorated substrates were exposed to a 5 mM solution of Grubbs (II) catalyst in dichloromethane for 10 min. The monolayers were rinsed with dichloromethane and immediately placed in a monomer solution containing 0.1 M NBF4, 0.05 M NBF6, 0.05 M NBF8, and 0.05 M NBF10 in dichloromethane for 1 min to grow pNBFn films that were ~50 nm. pNBFn films were also prepared in 0.5 M monomer solutions for 5 min to investigate the effect of fluorocarbon chain length on film growth. To determine the effects of monomer concentration on polymerization, pNBF8 films were prepared with monomer solutions ranging from 0.005 M – 1.0 M for 5 min. To obtain pNBH4 films, Grubbs II-modified surfaces were exposed to 0.47 M NBH4 solution for 10 min. All films were sequentially rinsed with fresh solvent, ethanol, and water and dried in a stream of nitrogen. A drop-cast film of pNBF10 was prepared utilizing ROMP in solution. Grubbs 2nd generation catalyst was added to 0.5 M NBF10

in dichloromethane at room temperature and polymerized for 30 min. The resulting polymer was cast onto a gold-coated silicon wafer and dried under vacuum for 24 h.

Results and Discussion

Kinetics and Concentration Effects

Films of pNBFn were grown from gold surfaces by utilizing SI-ROMP as depicted in Figure 6.3. A HOC_4S/Au SAM was treated with trans-3,6-endo-methylene-1,2,3,6-tetrahydrophthaloyl chloride, a norbornene with pendant acid chlorides in the 5 and 6 positions, to produce an ester-linked norbornene group on the surface. The resulting surface was made catalytically active for ROMP by exposure to Grubbs 2nd generation catalyst. Subsequent exposure to NBFn (n = 4, 6, 8, and 10) in dichloromethane (DCM) resulted in the growth of partially fluorinated polymer films from the surface in times ranging from 1 – 15 min.

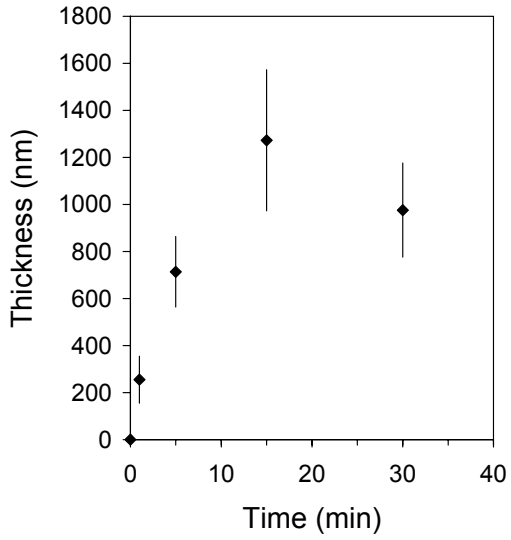

Figure 6.1. Kinetics of pNBF8 film growth by exposing Grubbs II-modified surfaces to 0.5 M NBF8 monomer solution in DCM.

As an example of the rapid kinetics of SI-ROMP of pNBFn, Figure 6.1 displays the growth of pNBF8 films from the surface in times ranging from 0 – 30 min. Polymerizations that exceeded 15 min did not result in thicker films as coupling and backbiting competes with metathesis and can actually result in decreased film thicknesses as observed by us[18] and others.[19, 27] The rapid growth of micron-scale pNBFn films by SI-ROMP contrasts the slower growth of ultrathin partially fluorinated films by ATRP.[13] Figure 6.2 displays the dependence of pNBF8 film growth on monomer concentration upon exposure to the monomer for 5 min. The linear dependence of pNBF8 thickness with monomer concentration suggests the ability to tune film thickness from ~50 nm to a few μm by changing the concentration of monomer in solution. The ability to achieve film thicknesses in excess of 1 μm in as little as 5 min is attributed to the rapid turnover and activity of the surface-bound Grubbs (II) catalyst. All monomers showed similar trends (not shown) with increased film thicknesses at higher monomer concentrations.

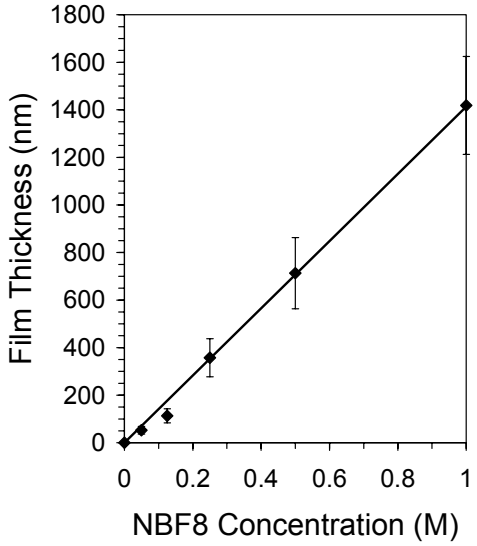

Figure 6.2. The effect of NBF8 monomer concentration on pNBF8 film thickness after exposure to the monomer in DCM for 5 min.

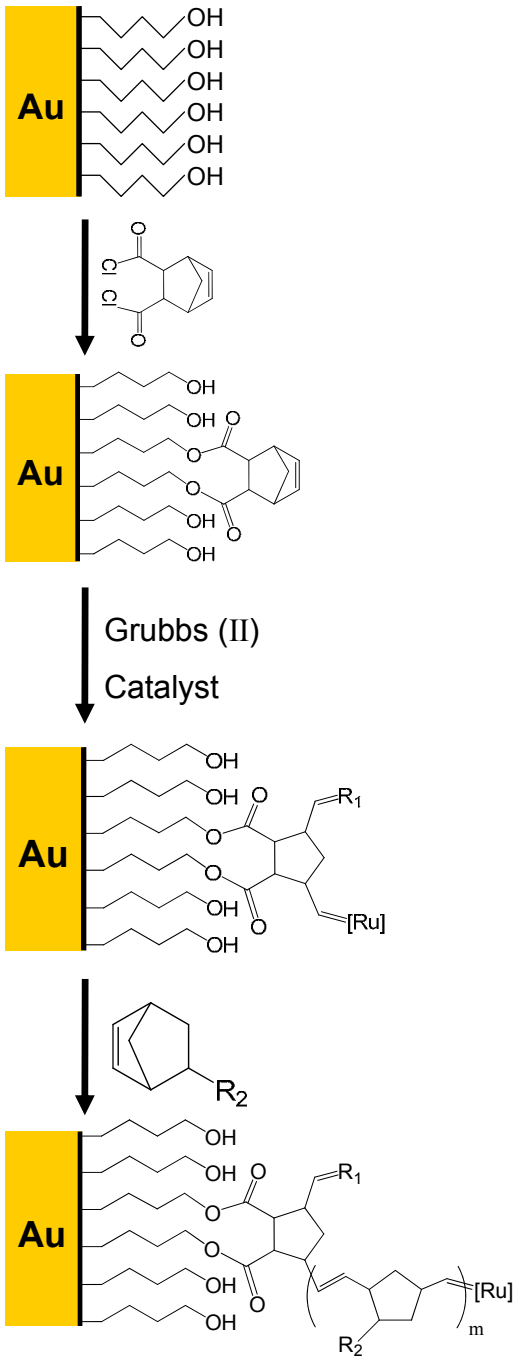

Figure 6.3. Schematic of SI-ROMP of 5-(perfluoro-alkyl)norbornenes on a gold substrate. A gold surface is modified with mercaptobutanol and further treated with trans-5-norbornene-2,3-dicarbonyl chloride for 30 min. The initiator is activated by Grubbs 2nd Generation catalyst, denoted as [Ru], and exposed to the NBFn monomer solution (R2 = C_4F_9, -C_6F_{13}, -C_8F_{17}, or -$C_{10}F_{21}$). R1 represents CHPh.

Effect of Fluorocarbon Chain Length

Table 6.1. Impedance properties and thicknesses of pNB and pNBFn films grown from 1 M monomer solutions for 5 min.

Film	Thickness (nm)	log (R_f(Ω cm^2))	C_f (nF/cm^2)
Initiator		1.3	19000
pNB	49	4.3	250
pNBF4	52	6.2	63.2
pNBF6	612	6.4	4.6
pNBF8	713	7.4	2.8
pNBF10	1565	7.5	1.6

The effect of fluorocarbon chain length (n) on film thickness upon exposure of Grubbs (II)-modified surfaces to 0.5 M NBFn in DCM for 5 min is shown in Table 6.1. Whereas pNBF4 and pNB (n = 0) yield similar thicknesses of ~50 nm, increasing n beyond 4 results in an order-of-magnitude increase in film thickness. The large thicknesses achieved in 5 min for pNBFn, where n = 6, 8, and 10, illustrate the rapid kinetics of SI-ROMP in comparison to other surface-initiated strategies. The trend of increasing thickness with longer fluorocarbon substituents is in stark contrast to the growth of non-fluorinated pNBHn that we observed previously.[19] SI-ROMP of NBHn yielded thinner films with more defects for increasing hydrocarbon chain-length, such that polymerization of NBH10 generated only sparse islands of polymer.[19] We attribute the dramatic increase in film growth for NBFn monomers with n > 4 to the greater strain of longer chains on the norbornenyl ring to assist metathesis[25] as well as the structure of the predominate endo monomers in solution. Perez et. al.[25] reported a structural conformation of endo NBFn monomers in solution such that they adopt a folded structure in which the fluorocarbon side chain folds back toward the olefin in the norbornenyl ring. The folded structure of the monomer units was theorized to obstruct access to the olefin

and interferes with the metathesis polymerization. They also noted a significant reduction in the amount of monomer that adopt the folded conformation for monomers for n > 6, as longer fluorocarbon chains are known to be stiff and would lack the flexibility to fold back to the olefin site. Thus, long flexible hydrocarbon chains on the norbornenyl ring would be expected to interfere with metathesis to a greater extent than would a much stiffer fluorocarbon chain of similar length.

Solvent Effects on Film Growth

To demonstrate the effect of solvent on SI-ROMP of NBFn, we grew pNBF4 and pNBF8 films in a variety of solvents and compared them to films grown in DCM. pNBF4 and pNBF8 films were prepared by exposure of Grubbs II-modified surfaces to 250 mM and 50 mM solutions, respectively, for 5 min. We observed little to no pNBF4 and pNBF8 film growth in chloroform or 1,2-dichloroethane, two halogenated solvents that are similar to DCM, although these solvents appear to solvate the monomers very well. However, pNBF4 films grown in 2,2,2-trifluoroethanol and 1,2,4-trichlorobenzene were comparable to those grown in DCM. pNBF8 films grew only in 1,2,4-trichlorobenzene but were much thinner than pNBF8 films prepared in DCM. Others have also observed that ROMP performed in solvents with stronger polarity, such as DCM, are more effective and have faster turn-over rates than less polar solvents.[28] For the SI-ROMP of pNBFn films, DCM appears to be an optimal solvent because of its significant polarity and capacity to solvate fluorinated species.

pNBFn Barrier Properties

The greater thicknesses for n > 4 translated into more protective coatings in an aqueous environment. We used electrochemical impedance spectroscopy to investigate the barrier properties of pNBFn films in the presence of $K_3Fe(CN)_6$ and $K_4Fe(CN)_6$ in 0.1 M Na_2SO_4(aq).

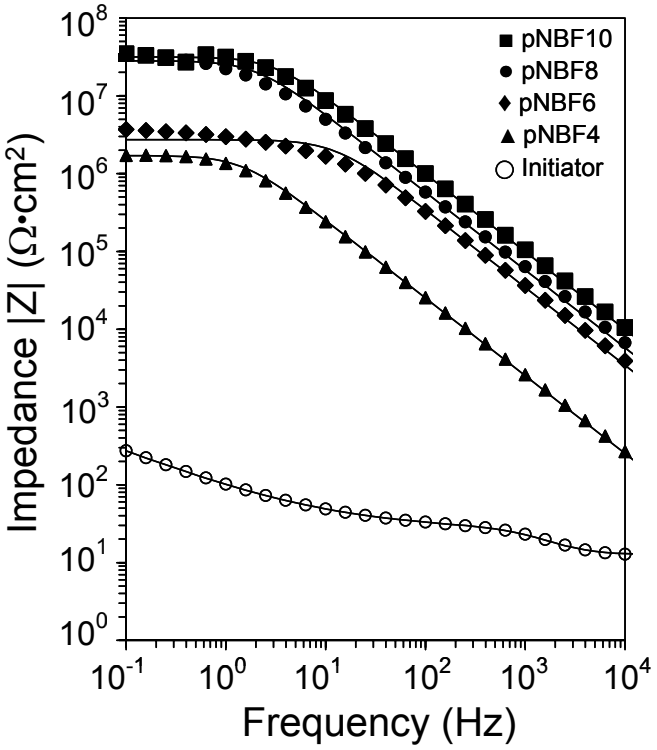

Figure 6.4. Electrochemical impedance spectra obtained in 1 mM $K_3Fe(CN)_6$ and 1 mM $K_4Fe(CN)_6$ in 0.1 M Na_2SO_4(aq) for the indicated films on gold prepared by exposure of Grubbs II-modified surfaces to 0.5 M NBFn for 5 min. Solid curves represent fits of the data using appropriate equivalent circuit models.

Representative Bode plots for pNBF4, pNBF6, pNBF8, and pNBF10 films that were prepared by exposure to a 0.5 M monomer solution in DCM for 5 min are shown in Figure 6.4. All films exhibit much higher impedance than that of the initiator SAM, and in general, the impedance at all frequencies scales with the thicknesses of these polymer

films from Table 6.1. The thicker films provide a more complete barrier with fewer defects to minimize the penetration of the redox probes. The impedance spectra of the polymer films are best fit with a Randle's equivalent circuit[29] modified with a Warburg impedance term to account for a resistance to mass transfer.[12] Table 6.1 shows film thicknesses along with the resistances (R_f) of the films against penetration by redox probes, and capacitance (C_f) values. The film resistances ($R_f \sim 10^{6\text{-}7}$ $\Omega^{\bullet}cm^2$) and capacitances (~2 - 63 nF) of pNBFn are comparable to those of other highly blocking fluorinated polymer films.[12] Consistent with the trends of film thickness, we observed an increase in the polymer film resistance and decrease in the film capacitance with increasing perfluorinated chain-length, with a dramatic decrease in capacitance for n > 4. When pNBFn films of similar thickness (~50 nm) were characterized by EIS, the results (not shown) indicated no effect of chain length.

Film Structure

We used RAIRS to determine the composition and structure of the pNBFn films. Figure 6.5 displays the fluorocarbon region of RAIR spectra for the pNBFn films where n = 4, 6, 8, and 10. The CF_2 stretching modes absorb strongly from 1100-1400 cm^{-1}. Due to the helical structure of fluoroalkyl chains, two types of CF_2 stretching peaks are expected in the IR: those lying along the helical axis ($\nu_{ax}(CF_2)$, 1300-1400 cm^{-1}) and those perpendicular to the helical axis ($\nu_{pd}(CF_2)$, 1100-1300 cm^{-1}).[30-32] The ratio of $\nu_{pd}(CF_2)$ to $\nu_{ax}(CF_2)$ absorbance for the film, relative to the same ratio for isotropic orientation of drop-cast pNBFn films, provides information on the orientation of the fluorocarbon side chains in the polymer film relative to the surface normal. RAIRS

utilizes inherent surface selection[30] such that the intensity for a given mode in the IR spectrum is proportional to the square of the component of its dynamic dipole moment oriented along the surface normal.

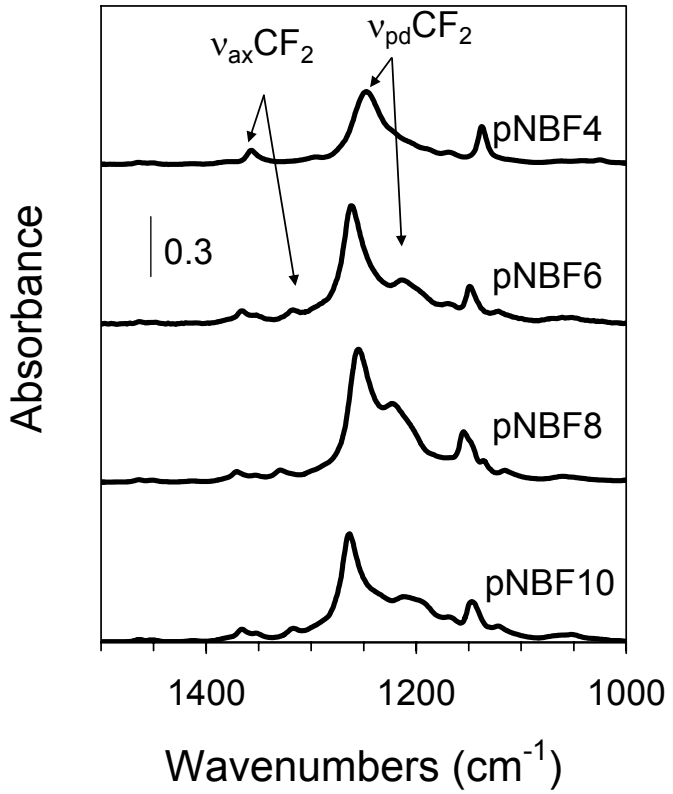

Figure 6.5. Reflectance absorption infrared spectra of pNBFn films. -CF_2 groups primarily exhibit two modes of stretching: ν_{ax} (CF_2) from 1300-1400 cm^{-1} and ν_{pd} (CF_2) from 1100-1300 cm^{-1}.

Figure 6.6 displays the RAIR spectrum for a drop cast film of pNBF10 where the absorbance of $\nu_{pd}(CF_2)$ to $\nu_{ax}(CF_2)$ is nearly equal. Thus, the orientation of fluorocarbon chains within polymer films grown from a surface can be assessed if the ratios of $\nu_{pd}CF_2$ to $\nu_{ax}CF_2$ differs from 1. For films where $\nu_{pd}CF_2$ to $\nu_{ax}CF_2$ is >> 1, the fluorocarbon chains are generally oriented parallel to the surface. However, if $\nu_{pd}CF_2$ to $\nu_{ax}CF_2$ is << 1, the fluorocarbon chains are primarily oriented normal to the surface. We observe a

high ratio of $\nu_{pd}(CF_2)$ to $\nu_{ax}(CF_2)$ absorbance (> 4) in the surface-initiated pNBFn films, as shown in Figure 6.5, indicating the fluorinated side chains of the polymer are generally oriented more along the parallel to the gold substrate. This parallel orientation of the fluorocarbon groups is similar to that in semi-fluorinated polyisoprene films reported by Genzer et. al.[31] and that reported by us for the acylation of PHEMA films with perfluorinated acid chlorides.[12]

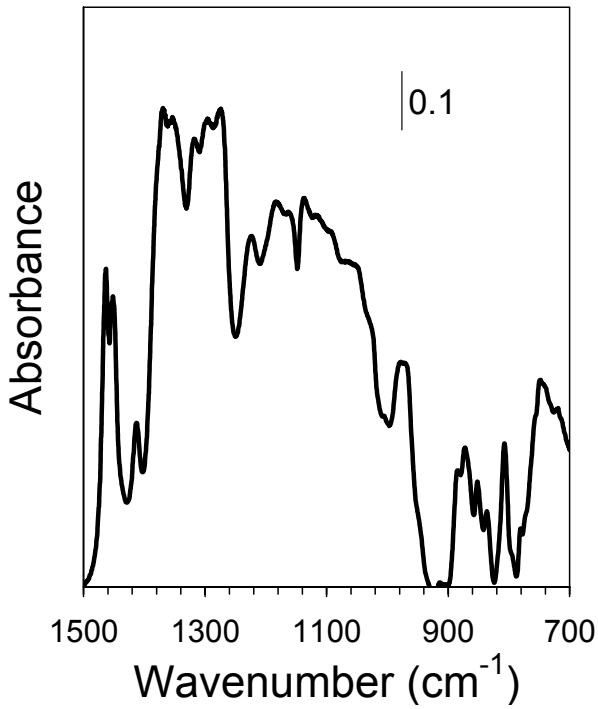

Figure 6.6. RAIR spectrum of a drop-cast pNBF10 film.

Film Stability

pNB (n = 0) films have been reported as oxidatively unstable due to the unprotected olefin functionality located along the polymer backbone. Seehof and co-workers demonstrated that fluorocarbon substituents increase oxidative stability such that fluorinated polynorbornenes showed no degradation over time, whereas, unmodified pNB

started to degrade within 24 h.[32] They attribute oxidative stability to the electron-withdrawing nature of the fluorocarbon moieties, which stabilize the polymer. Elimination of chain unsaturation by sulfonation of the olefins to achieve a hydroxysulfonate product also results in more stable pNB polymer films, but sulfonation increases the solubility of any chains that were already oxidatively cleaved and may result in their removal from the film upon rinsing.[26] Thus, the sulfonation process itself can be used as a measure of the stability of the polymer film. Previously, we observed 40% film loss of pNB films upon 1 min exposure to acetyl sulfate.[26] However, negligible film loss was observed during the sulfonation of pNBF4 over a 24 h exposure to acetyl sulfate.[33] The improved stability imparted by the fluorocarbon side chains is likely the result of diluting olefin functionality within the film to inhibit reactions such as coupling and backbiting that are known to cleave chain fragments.[34-36] For $n \geq 4$, the fluorocarbon chain consists of ≥ 77% of the mass of the monomer repeat unit.

Surface Properties

We utilized contact angle goniometry to probe the surface of the pNBFn films. Table 2 summarizes the advancing contact angles of water and hexadecane droplets in contact with pNBFn films. As n increases, the surfaces of the films increase in hydrophobicity and oleophobicity with the exception of pNBF10. The pNBFn films present hydrophobic and oleophobic surfaces that should have low critical surface tensions (γ_C), defined as the highest surface tension of liquid that completely wets the surface. Surfaces dominated by $-CF_3$ groups exhibit a γ_C of 6-9 mN/m, whereas $-CF_2-$ surfaces such as PTFE exhibit γ_C of ~18 mN/m. To estimate the critical surface tensions

of the films, we used the Zisman method[37, 38] and selected a series of *n*-alkanes having even numbers of carbons, from hexane to tetradecane, as contacting liquids. θ_A for each of the liquids was measured on each pNBFn film, and cos θ_A was plotted against γ_L, the surface tension of the liquid (Figure 6.7). A straight line fit of the data and extrapolation of the line to cos θ_A= 1 gives γ_C of the film such that a liquid with $\gamma_L \leq \gamma_C$ will completely wet the surface.

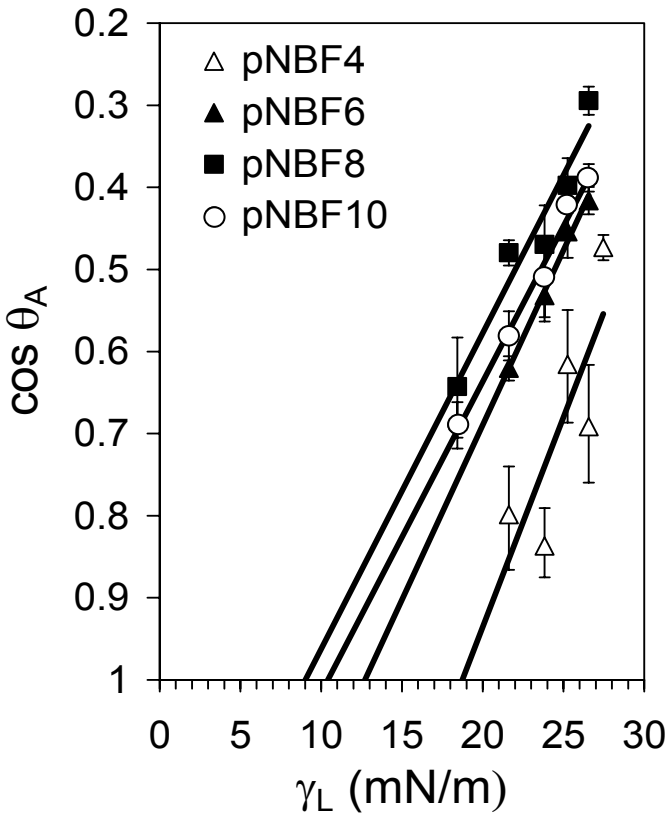

Figure 6.7. Zisman plot of advancing contact angles of hexane (γ = 18.4 mN/m), octane (γ = 21.6 mN/m), decane (γ = 23.8 mN/m), dodecane (γ = 25.2 mN/), and tetradecane (γ = 26.6) on pNBFn films that were exposed to air for at least 12 h prior to measurement. The lines represent least square fits to the data and are extrapolated to cos θ_A = 1.0 to determine the critical surface energy (γ_C).

pNBF8 yielded the lowest surface energy of these films with a γ_C of ~9 mN/m, consistent with a CF_3-rich surface that contains some higher energy -CF_2- groups. The

low critical surface energy of pNBF8 and the implied dominance of $-CF_3$ groups at the surface is consistent with fluorocarbon chains orientated normal to the substrate at the liquid/polymer interface, whereas, the fluorocarbon chains in the bulk of the film adopt a parallel orientation based on the large ratio of $\nu_{pd}(CF_2)$: $\nu_{ax}(CF_2)$ absorbances in RAIR spectra (Figure 6.5). Consistent with advancing contact angles of water and hexadecane, the γ_C of the pNBFn films decreased with increasing fluorocarbon side chain length with the exception of the pNBF10 films. The discontinuance of this trend for n = 10 may be related to its larger CF_2:CF_3 ratio, exposing more $-CF_2-$ groups and reducing oleophobicity, or its presumed lower mobility to achieve a dense, oriented fluorocarbon film at the outer surface. The low γ_C's of pNBF10 (~11 mN/m) and pNBF6 (~13 mN/m) indicate that the fluorocarbon chains at the surface are oriented generally normal to the substrate, but with more $-CF_2-$ groups exposed than for pNBF8. However, the fluorocarbon chains within pNBF4 do not orient at the surface like the other pNBFn films. From Figure 6.7, we estimate the γ_C of pNBF4 to be ~19 ± 2 mN/m, suggesting that -CH- and $-CH_2-$ groups are present at the surface, as well as $-CF_2-$ and $-CF_3$ functionalities.

Table 2. Wetting properties and critical surface tensions of pNBFn films.

	Advancing Contact Angle (°)		
Film	water	hexadecane	γ_C *(mN/m)*
pNBF4	110 ± 2	61 ± 1	19 ± 2
pNBF6	116 ± 5	67 ± 1	13 ± 1
pNBF8	123 ± 3	78 ± 1	9 ± 1
pNBF10	120 ± 3	73 ± 2	11 ± 1

The Zisman plot shown in Figure 6.7 displays the γ_C of pNBFn films exposed to air for at least 12 h. The γ_C's for freshly prepared pNBFn films were 2-3 mN/m higher than those exposed to air, which is consistent with the gradual diffusion of the fluorocarbon side chains to the air/polymer interface. The tendency for fluorocarbon moieties to partition to the air/polymer interface has been observed by others[31, 39] and is related to their mobility and the driving force to reduce interfacial free energy.

Film Morphology

We used scanning electron microscopy (SEM) in conjunction with atomic force microscopy (AFM) to investigate the morphology and topography of pNBFn films. Figure 6 displays SEM images of pNBFn films grown for 1 min using 0.1 M (n = 4) or 0.05 M (n = 6, 8, and 10) monomer concentrations in which we observed distinct light/dark patterns. As a control, we obtained SEM micrographs of pNBH4 films, also displayed in Figure 6.8, that do not show the patterns found in the pNBFn films. Contrast in SEM images is due to varying chemical composition of the polymer, where brighter areas correspond to higher molecular weight elements or higher electron density.[40]

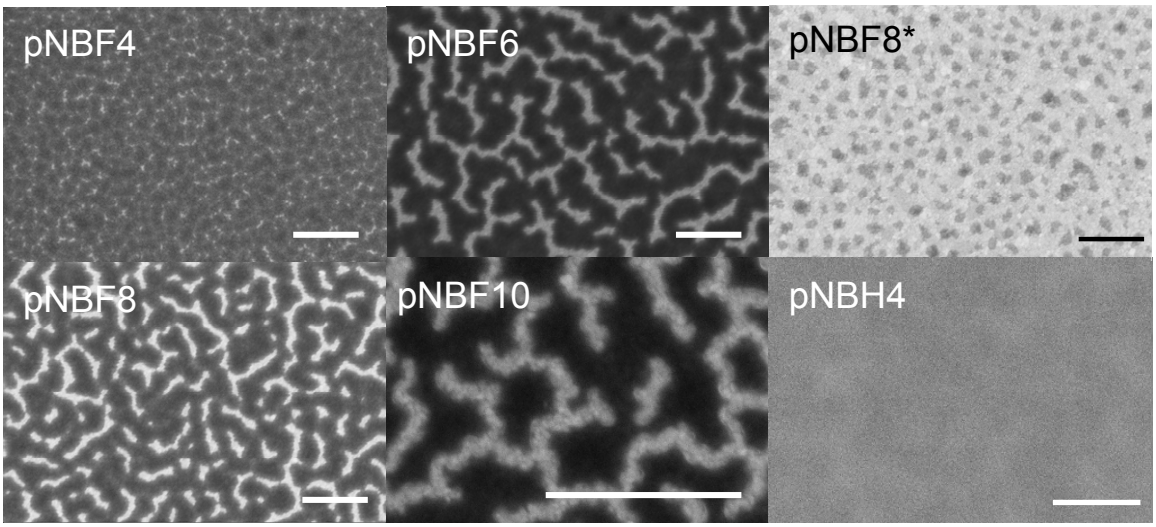

Figure 6.8. Scanning electron micrographs of pNBF4, pNBF6, pNBF8, pNBF10, and pNBH4 films. The pNBF6, pNBF8, and pNBF10 films were grown in 0.05 M monomer solutions for 1 min, whereas pNBF4 and pNBH4 were grown in 0.1 M and 0.47 M monomer solutions for 1 min, respectively. The scale bar indicates 1 μm. * For the top right pNBF8 panel, the film has been annealed at 120 °C for 1 h.

The observed patterns are not due to islands within a sparse polymer film as the AFM image in Figure 6.9, the barrier properties displayed in Table 2, and the critical surface energies of Figure 6.7 confirm the growth of dense pNBFn films. A naïve interpretation of the image might suggest that the lighter regions are fluorocarbon and the darker ones are hydrocarbon. However, the fact that pNBFn is a comb-like homopolymer in which fluorocarbon and hydrocarbon regions cannot be completely separated, combined with the size (~50 – 100 nm) and fractional coverage of the lighter regions in Figure 6.8, are inconsistent with complete phase separation. Indeed, these patterns are much too large to represent the molecular structuring of a few neighboring chains, since the width of two adjacent polymer chains for pNBF10 would span approximately 2 nm. Further, the size of these lighter regions does not scale with fluorocarbon chain length (n), and the very low critical surface energies for n = 6, 8, and

10 are consistent with dense fluorocarbon layers over the entire outermost surface and not just fractionally in the lighter regions.

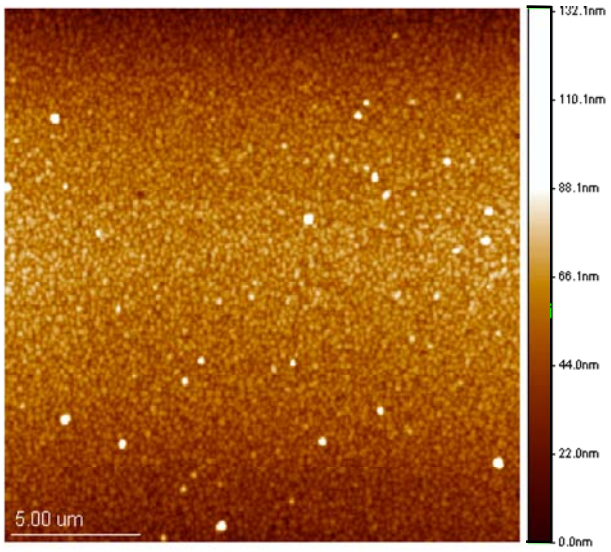

Figure 6.9. Atomic force microscopy tapping mode image of a pNBF10 polymer film grown by exposure to 0.05 M NBF10 in DCM for 1 min.

A closer view of these regions in Figure 6.8, panel pNBF10, reveals the presence of small round clusters of 20 – 30 nm in both the lighter and darker regions. Since SEM is probing the outermost few nm of the surface,[40] the lighter regions may correspond to specific organization within polymer chains that concentrate fluorocarbon groups densely at the outer few nm of the surface, such as a hemispherical shell of dense fluorocarbon with hydrocarbon chains concentrated in the core. The darker regions, which still correspond to fluorocarbon groups at the outer surface, likely represent a different type of chain conformation where fluorocarbon groups are not concentrated as extensively in the outer few nm of the film. Annealing the film at 120 °C followed by cooling to room temperature provides sufficient energy for more chains to adopt the low-energy

configuration to produce a less heterogeneous SEM image that shows a prevalence of the lighter region (Figure 6.8, panel pNBF8*).

Conclusions

We have utilized SI-ROMP of perfluorinated n-alkylnorbornenes to form robust partially fluorinated polymer films of tunable thicknesses ranging from tens of nanometers to microns on gold substrates. The length of the fluorocarbon substituent on the norbornenyl ring influences the properties of the polymer film. Increasing the length of the fluorocarbon side chain enhances the rate and extent (thickness) to which the polymer films grow from the surface. The critical surface tensions also decrease with increasing fluorocarbon chain length in which pNBF8 films yield the lowest critical surface energy, ~9 mN/m. Upon exposure to air, the fluorocarbon chain segments of the pNBFn films seek the air/polymer interface, enhancing the hydrophobicity and oleophobicity of the surface. SI-ROMP of pNBFn yields 20 – 30 nm clusters of different conformations of the polymer chains, observed as distinct light/dark patterns in SEM micrographs.

References

1. Wang, J. G.; Mao, G. P.; Ober, C. K.; Kramer, E. J., Liquid crystalline, semifluorinated side group block copolymers with stable low energy surfaces: Synthesis, liquid crystalline structure, and critical surface tension. *Macromolecules* **1997,** 30, 1906-1914.

2. Rutenberg, I. M.; Scherman, O. A.; Grubbs, R. H.; Jiang, W.; Garfunkel, E.; Bao, Z., Synthesis of Polymer Dielectric Layers for Organic Thin Film Transistors via Surface-Initiated Ring-Opening Metathesis Polymerization. *Journal of the American Chemical Society* **2004,** 126, 4062-4063.

3. Garbassi, F.; Morra, M.; Occhiello, E., *Polymer surfaces: from physics to technology*. John Wiley & Sons: Chichester, 1998.

4. Tarnowski, D. J.; Bekos, E. J.; Korzeniewski, C., Oxygen-transport characteristics of refunctionalized fluoropolymeric membranes and their application in the design of biosensors based upon the clark-type oxygen probe. *Analytical Chemistry* **1995,** 67, 1546-1552.

5. Balachandra, A. M.; Baker, G. L.; Bruening, M. L., Preparation of composite membranes by atom transfer radical polymerization initiated from a porous support. *Journal of Membrane Science* **2003,** 227, 1-14.

6. Mocella, M. T. In *Fluorinated compounds for advanced IC interconnect applications: a survey of chemistries and processes*, 2003; Elsevier Science Sa: 2003; pp 87-92.

7. Genzer, J.; Sivaniah, E.; Kramer, E. J.; Wang, J. G.; Xiang, M. L.; Char, K.; Ober, C. K.; Bubeck, R. A.; Fischer, D. A.; Graupe, M.; Colorado, R.; Shmakova, O. E.; Lee, T. R., Molecular orientation of single and two-armed monodendron semifluorinated chains on "soft" and "hard" surfaces studied using NEXAFS. *Macromolecules* **2000,** 33, 6068-6077.

8. Phani, A. R.; Passacantando, M.; Santucci, S., Structural, compositional, thermal resistant and hydro-oleophobic properties of fluorine based block-co-polymer films on quartz substrates by wet chemical process. *Journal of Physics and Chemistry of Solids* **2006,** 67, 1703-1711.

9. Sivakumar, C.; Wen, T. C.; Gopalan, A.; Teng, H., Electroactive conducting blends of poly(o-toluidine) and poly(vinylidene fluoride) and characterisation. *Synthetic Metals* **2003,** 132, 219-226.

10. Edmondson, S.; Osborne, V. L.; Huck, W. T. S., Polymer brushes via surface-initiated polymerizations. *Chemical Society Reviews* **2004,** 33, 14-22.

11. Jennings, G. K.; Brantley, E. L., Physicochemical properties of shurface-initiated polymer films in the modification and processing of materials. *Adv. Mater.* **2004,** 16, 1983-1994.

12. Brantley, E. L.; Jennings, G. K., Fluorinated Polymer Films from Acylation of ATRP Surface-Initiated Poly(hydroxyethyl methacrylate). *Macromolecules* **2004,** 37, 1476-1483.

13. Jung, D. H.; Park, I. J.; Choi, Y. K.; Lee, S. B.; Park, H. S.; Ruhe, J., Perfluorinated polymer monolayers on porous silica for materials with super liquid repellent properties. *Langmuir* **2002,** 18, 6133-6139.

14. Matyjaszewski, K.; Miller, P. J.; Shukla, N.; Immaraporn, B.; Gelman, A.; Luokala, B. B.; Siclovan, T. M.; Kickelbick, G.; Vallant, T.; Hoffmann, H.; Pakula, T., Polymers at interfaces: Using atom transfer radical polymerization in the controlled growth of homopolymers and block copolymers from silicon surfaces in the absence of untethered sacrificial initiator. *Macromolecules* **1999,** 32, 8716-8724.

15. Kim, J. B.; Huang, W.; Bruening, M. L.; Baker, G. L., Synthesis of Triblock Copolymer Brushes by Surface-Initiated Atom Transfer Radical Polymerization. *Macromolecules* **2002,** 35, 5410-5416.

16. Wang, X. S.; Lascelles, S. F.; Jackson, R. A.; Armes, S. P., Facile synthesis of well-defined water-soluble polymers via atom transfer radical polymerization in aqueous media at ambient temperature. *Chem. Commun.* **1999**, 1817-1818.

17. Robinson, K. L.; Khan, M. A.; Banez, M. V. D.; Wang, X. S., Controlled polymerization of 2-hydroxyethyl methacrylate by ATRP at ambient temperature. *Macromolecules* **2001,** 34, 3155-3158.

18. Brantley, E. L.; Holmes, T. C.; Jennings, G. K., Modification of Poly(hydroxyethyl methacrylate) Films with Hydrocarbon Side Chains. *J. Phys. Chem. B* **2004,** 108, 16077-16084.

19. Berron, B. J.; Graybill, E. P.; Jennings, G. K., Growth and Structure of Surface-Initiated Poly(n-alkylnorbornene) Films. *Langmuir* **2007,** 23, 11651-11655.

20. Kim, N. Y.; Jeon, N. L.; Choi, I. S.; Takami, S.; Harada, Y.; Finnie, K. R.; Girolami, G. S.; Nuzzo, R. G.; Whitesides, G. M.; Laibinis, P. E., Surface-Initiated Ring-Opening Metathesis Polymerization on Si/SiO2. *Macromolecules* **2000,** 33, 2793-2795.

21. Buchmeiser, M. R.; Sinner, F.; Mupa, M.; Wurst, K., Ring-Opening Metathesis Polymerization for the Preparation of Surface-Grafted Polymer Supports. *Macromolecules* **2000,** 33, 32-39.

22. Liu, X. G.; Guo, S. W.; Mirkin, C. A., Surface and site-specific ring-opening metathesis polymerization initiated by dip-pen nanolithography. *Angew. Chem., Int. Ed.* **2003,** 42, 4785-4789.

23. Weck, M.; Jackiw, J. J.; Rossi, R. R.; Weiss, P. S.; Grubbs, R. H., Ring-Opening Metathesis Polymerization from Surfaces. *J. Am. Chem. Soc.* **1999,** 121, 4088-4089.

24. Pasquale, A. J.; Fornof, A. R.; Long, T. E., Synthesis of norbornene derivatives by Diels-Alder cycloaddition and subsequent copolymerization with maleic anhydride. *Macromol. Chem. Phys.* **2004,** 205, 621.

25. Perez, E.; Laval, J. P.; Bon, M.; Rico, I.; Lattes, A., Synthesis of bicyclo [2· 2· 1] hept-2-enes with mono and disubstituted long perfluorinated chains CnF2n+1 (n = 4,6,8,10) Investigation of association in solution by 19F NMR study of polymerization via a metathetic reaction. *Journal of Fluorine Chemistry* **1988,** 39, 173-196.

26. Berron, B. J.; Payne, P. A.; Jennings, G. K., Sulfonation of Surface-Initiated Polynorbornene Films. *Industrial & Engineering Chemistry Research* **2008,** 47, (20), 7707-7714.

27. Harada, Y.; Girolami, G. S.; Nuzzo, R. G., Catalytic amplification of patterning via surface-confined ring-opening metathesis polymerization on mixed primer layers formed by contact printing. *Langmuir* **2003,** 19, 5104-5114.

28. Stark, A.; Ajam, M.; Green, M.; Raubenheimer, H. G.; Ranwell, A.; Ondruschka, B., Metathesis of 1-octene in ionic liquids and other solvents: Effects of substrate solubility, solvent polarity and impurities. *Advanced Synthesis & Catalysis* **2006,** 348, 1934-1941.

29. Jennings, G. K.; Laibinis, P. E., Self-Assembled n-Alkanethiolate Monolayers on Underpotentially Deposited Adlayers of Silver and Copper on Gold. *J. Am. Chem. Soc.* **1997,** 119, 5208-5214.

30. Parikh, A. N.; Allara, D. L., Quantitative-determination of molecular-structure in multilayered thin-films of biaxial and lower symmetry from photon spectroscopies.1. Reflection Infrared vibrational spectroscopy. *Journal of Chemical Physics* **1992,** 96, 927-945.

31. Genzer, J.; Sivaniah, E.; Kramer, E. J.; Wang, J. G.; Korner, H.; Xiang, M. L.; Char, K.; Ober, C. K.; DeKoven, B. M.; Bubeck, R. A.; Chaudhury, M. K.; Sambasivan, S.; Fischer, D. A., The orientation of semifluorinated alkanes attached to polymers at the surface of polymer films. *Macromolecules* **2000,** 33, 1882-1887.

32. Seehof, N.; Grutke, S.; Risse, W., Selective Reaction of Exo-Isomers in Ring Opening Olefin Metathesis Polymerization of Fluoroalkyl-Substituted Norbornene Derivatives. *Macromolecules* **1993,** 26, 695-700.

33. Berron, B.; Faulkner, C. J.; Fischer, R. E.; Payne, P. A.; Jennings, G. K., Surface-Initiated Growth of Ionomer Films from Pt-Modified Gold Electrodes. *Langmuir* **2009**.

34. Hatjopoulos, J. D.; Register, R. A., Synthesis and properties of well-defined elastomeric poly(alkylnorbornene)s and their hydrogenated derivatives. *Macromolecules* **2005,** 38, 10320-10322.

35. Lee, L. B. W.; Register, R. A., Hydrogenated ring-opened polynorbornene: A highly crystalline atactic polymer. *Macromolecules* **2005,** 38, 1216-1222.

36. Boyd, T. J.; Schrock, R. R., Sulfonation and Epoxidation of Substituted Polynorbornenes and Construction of Light-Emitting Devices. *Macromolecules* **1999,** 32, 6608-6618.

37. Zisman, W. A., *Contact Angle, Wettability, and Adhesion*. American Chemical Society: Washington, DC, 1964; Vol. 43.

38. Bin Zhang, Z.; Ying, S. K.; Hu, Q. H.; Xu, X. D., *Journal of Applied Polymer Science* **2002,** 83, 2625-2633.

39. Xie, X. M.; Gengenbach, T. R.; Griesser, H. J., Changes in wettability with time of plasma-modified perfluorinated polymers. *Journal of Adhesion Science and Technology* **1992,** 6, 1411-1431.

40. Bindell, J. B., Scanning Electron Microsopy. In *Encylopedia of Materials Characterization*, Brundle, C. R.; Jr., C. A. E.; Wilson, S., Eds. Butterworth-Heinemann: Boston, 1992; pp 70-84.

CHAPTER VII

SURFACE-INITIATED GROWTH OF IONOMER FILMS FROM PT-MODIFED GOLD ELECTRODES

Introduction

The direct wiring of ionomer films to electrode surfaces is beneficial to control interfacial composition in many energy-related applications.[1-3] In a proton exchange membrane (PEM) fuel cell, for example, the so-called "triple interface"[4,5] at the cathode requires that catalyst particles be electronically wired to a conductive gas diffusion layer and ionically interfaced with a proton-conducting polymer to enable the convergence of oxygen, protons, and electrons for the production of water. Chemisorption of the ionomer at the electrode surface enables the direct wiring for efficient transfer of protons and oxygen to the electrode surface and has been shown to boost electrochemical performance.[1,3] However, a key issue regarding the direct chemical wiring of ionomer to electrode/catalyst interfaces is the possible deactivation of the catalyst by the chemisorption event.

In this chapter, we report the surface-initiated growth and sulfonation of polynorbornene (pNB), poly(5-n-butylnorbornene) (pNBH4), and poly(5-n-perfluorobutylnorbornene) (pNBF4) to prepare ionomer films on gold electrodes that are pre-modified by an atomic layer of Pt. This experimental system offers two unique advantages in the investigation of chemisorbed ionomer/electrode interfaces. First, the Pt monolayer is localized at a well-defined 2-D interface such that its loading is ultra low and its utilization in an electrochemical reaction is potentially very high. Second, since

the catalytic performance of the electrode is easily diminished by displacement or chemical alteration of the single Pt layer, its performance is extremely sensitive to the nature of the chemisorption of ionomer.

Surface-initiated polymerization is a commonly used method for coating 2-D or complex, three-dimensional substrates with uniform films of well-controlled thicknesses.[6-12] In surface-initiated polymerization, the monomer reacts with a surface-tethered initiator or polymerization catalyst, resulting in the growth of a polymer chain from the surface.[6] As fuel cell interfaces evolve from nearly 2-D to highly porous, 3-D systems,[13] the ability to grow ionomer from the electrode surface, monomer by monomer, is essential to ensure the appropriate integration of ionomer with electrode/catalyst. Presynthesized bulk ionomer would be restricted from entering small pores, leading to inaccessibility of the expensive catalyst in those pores to the transport of reactants. Here, we employ the surface-initiated ring opening metathesis polymerization of three different norbornenes, followed by sulfonation of their olefinic groups,[2] as a route towards ultrathin ionomer coatings of tunable thickness with tailored hydrophobicity. Our work represents the first reported surface-initiated growth of pNBF4 as well as the first functionalization of Pt monolayer/Au surfaces. Through complementary characterizations of the resulting films and interfaces, we have investigated the effects of ionomer attachment and side chain composition on the impedance against proton transfer as well as the current and potential of the oxygen reduction reaction.

In order to fully assess the performance of the ionomer coating, it must be evaluated in a catalytic electrode assembly. The deposition of platinum as an oxygen reduction reaction (ORR) catalyst is an essential step in many electrode processes.[14-16]

The expense of platinum necessitates sparse and controlled use both experimentally and in commercial applications. For maximum utilization of the Pt, a monolayer of Pt atoms on the support is desirable, allowing each Pt atom to be accessible by the reactants. Brankovic and Adzic have developed a process of depositing adlayers of platinum onto gold surfaces through a two step process.[17] They utilize underpotential deposition (UPD)[18] to achieve sub-monolayer coverages of copper atoms onto the gold supports, and then electrolessly exchange the copper with platinum, thus immobilizing an adlayer of platinum on the gold surface.[17] The deposition of the platinum adlayer at a well-defined planar interface potentially allows for complete utilization of this catalyst.

Our goal here is to demonstrate proof-of-concept systems for the integration of ionomer and catalyst at model 2-D electrode surfaces. Although a 2-D Pt/Au electrode is not an appropriate substrate for PEM fuel cells, elements of the strategy presented here could be extended to 3-D supports in which the deposition of Pt[19,20] and the surface-initiated growth of polymers[21,22] remain viable. An important aspect of the work is to investigate the compatibility of surface-initiated, chemisorbed ionomer with a catalytically active electrode for oxygen reduction. A 2-D electrode offers a straightforward integration of ionomer with catalyst as well as ease of characterization of the performance of the interface and therefore, is used exclusively in this study. By controlling the hydrophobicity of the ionomer through selection of side chain, we are able to examine the effect of ionomer composition on the performance of the electrode.

In surface-initiated polymerizations, only a small fraction (often $< 10\%$)[7] of the initiator sites typically yield polymer. For electrochemical applications, those adsorbates that do not tether polymer can block catalyst sites on the surface and hamper the

performance of the electrode. Here, we demonstrate the ability to electrochemically reduce and desorb these short, non-polymeric adsorbates from the surface without affecting the surface-attached ionomer. Others[23,24] have used electrochemical reduction to remove alkanethiolate SAMs from gold surfaces. Here, we extend this approach to heterogeneous films containing short-chain thiolates and tethered polymer chains on Pt/Au and gold electrodes. We show that desorption of these short molecular components from the polymer/electrode interface reduces interfacial impedance and greatly improves the performance of the Pt/Au electrode for oxygen reduction.

Experimental Procedures

Polymer Film Preparation

Gold substrates were placed in a 1.0 mM ethanolic solution of 4-mercapto-1-butanol for at least 1 h to yield a hydroxyl-terminated self-assembled monolayer. The samples were rinsed in ethanol and dried in a stream of nitrogen. Exposure of the SAM to a 5 mM solution of trans-3,6-endo-methylene-1,2,3,6-tetrahydrophthaloyl chloride in dichloromethane for 30 min yields the acylation product of a surface-tethered norbornenyl group.[2] The samples were rinsed in ethanol and dried in a stream of N_2. The norbornenyl decorated substrates were exposed to a 5 mM solution of Grubbs (I) catalyst in dichloromethane for 15 min for growth of pNB or pNBH4. The monolayers were rinsed with dichloromethane and immediately placed in a monomer solution containing 1.0 M norbornene in toluene or 1.0 M NBH4 in dichloromethane for 15 min to achieve ~120 nm polymer films. To achieve 50 nm films, a concentration of 0.27 M NB or 0.5 M NBH4 and the same time of 15 min was utilized. The norbornenyl decorated

substrates were exposed to a 5 mM solution of Grubbs (II) catalyst in dichloromethane for 15 min for growth of pNBF4. The monolayers were rinsed with dichloromethane and immediately placed in a monomer solution containing 1.0 M or 0.1 M NBF4 in dichloromethane for 15 min to grow pNBF4 films that were ~120 nm or ~50 nm, respectively. All films were sequentially rinsed with fresh solvent, ethanol, and water and dried in a stream of nitrogen.

Sulfonation

A 1.0 M acetyl sulfate solution in dichloromethane was prepared immediately prior to use similar to Tran et al.[26] Acetic anhydride (2.8 mL) was added to dichloromethane (14.0 mL) at 0˚C. Concentrated sulfuric acid (1.0 mL) was added dropwise to the acetic acid solution resulting in a 1.0 M acetyl sulfate solution in DCM. 1.0 mL of the 1.0 M acetyl sulfate solution was diluted to 0.1 M through the addition of 9.0 mL of dichloromethane. Polymer-coated substrates were exposed to the 0.1 M solution of acetyl sulfate for 1 min to yield a surface-tethered sulfonated polymer coating. Samples were rinsed with dichloromethane and ethanol and dried in a nitrogen stream.

Copper and Platinum Deposition

Underpotential deposition of copper was performed with a Gamry Instruments CMS300 impedance system interfaced to a personal computer. Potentials were cycled at 20 mV/s between 500 and 50 mV vs $Cu^{0/1+}$ in a N_2-saturated solution of 1.0 mM $CuSO_4$ in 0.1 M H_2SO_4(aq) using a polycrystalline gold-coated counter electrode. After at least two cycles, the potential was held just negative of the deposition peak (~100 mV) on the

cathodic sweep, and the sample was removed from solution under potential control. Samples were rinsed in ethanol and dried in a nitrogen stream.

Copper-coated gold substrates were immediately placed in a N_2-saturated solution of 1.0 mM K_2PtCl_4 in 0.1 M H_2SO_4(aq). After 5 min, samples were removed from solution, rinsed sequentially with water and ethanol and dried in a nitrogen stream.

Monitoring the Oxygen Reduction Reaction

The catalysis of the oxygen reduction reaction (ORR) was monitored via cyclic voltammetry (CV) with a Gamry Instruments CMS300 impedance system interfaced to a personal computer. ORR measurements were obtained using a Ag/AgCl/saturated KCl reference electrode (EG&G Instruments) with a Pt mesh as the counter electrode in an O_2 saturated, 0.1 M H_2SO_4(aq). Samples were cycled at 50 mV/ s over potentials from 800 to 0 mV in an O_2-saturated, 0.1 M H_2SO_4(aq). Due to irreproducibilities in the mass transfer of oxygen over various experiments, we report here the half-wave potential ($E_{1/2}$), or the potential corresponding to half the maximum current.

Desorption of Short-Chain Thiolates

Cyclic voltammetry was used to monitor thiolate desorption from gold substrates using a Gamry Instruments CMS300 impedance system interfaced to a personal computer. Potentials were cycled at 200 mV/s between 0 and -1000 mV vs a Ag/AgC/saturated KCl reference in a N_2-saturated solution of 50.0 mM $NaH_2PO_4 \cdot H_2O$(aq) (pH 8.3) using a polycrystalline gold-coated counter electrode.

Preparation of Pt Submonolayers on Au

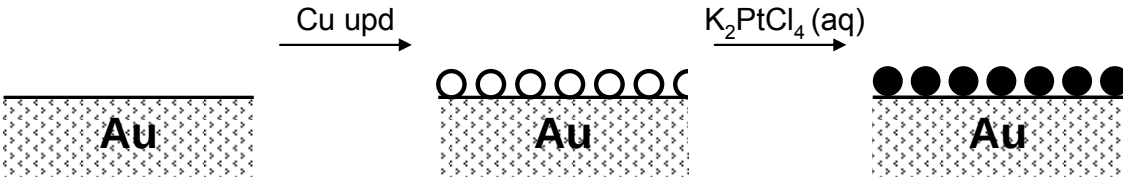

Figure 7.1. Schematic illustration of the deposition of a Pt monolayer onto a gold electrode by the underpotential deposition (upd) of Cu followed by electroless exchange of Cu with Pt.

To prepare Pt submonolayers on a gold electrode, we have used the method of Adzic and co-workers[17] where Pt electrolessly displaces a copper submonolayer from the gold surface (Figure 7.1). We first deposit a submonolayer of copper onto a polycrystalline gold-coated substrate via underpotential deposition (UPD) from a solution of 1.0 mM copper sulfate and 0.1 M sulfuric acid.[27] As shown in the cyclic voltammogram of Figure 7.2, the positions of the anodic Cu (220 mV vs Cu wire) and cathodic (170 mV) peaks are consistent with previous reports,[27] and signify the stripping and deposition, respectively, of a submonolayer of copper on the gold surface.

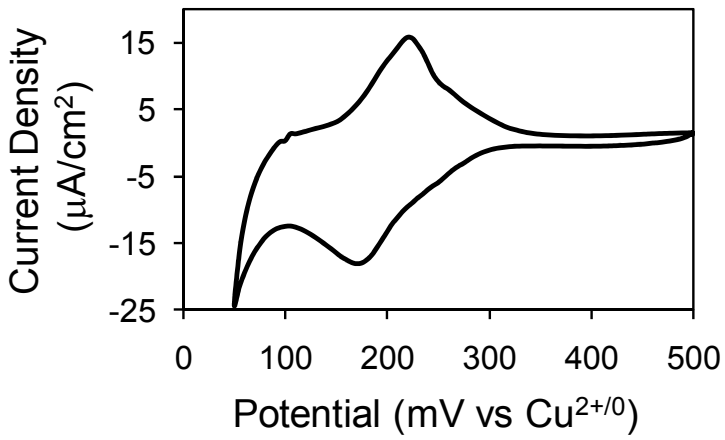

Figure 7.2. Cyclic voltammogram for a polycrystalline gold substrate in 0.1 M H_2SO_4 and 1.0 mM $CuSO_4$ (aq). The large peaks at 170 mV and 220 mV on the cathodic and anodic scans, respectively, indicate the deposition and stripping, respectively, of a copper submonolayer. The potential was held at ~100 mV on the reductive scan, and the electrode was removed and found to contain a fractional copper coverage of 0.78 by XPS.

On the cathodic sweep, the potential of the system was held just negative of the UPD peak (~100 mV), and the sample was removed from solution under constant potential. The presence of copper on the gold surface was confirmed through the Cu $2p_{3/2}$ and $2p_{1/2}$ peaks at 932 and 952 eV, respectively, in the XPS spectrum (Figure 3). The fractional coverage of the Cu adlayer (ϕ_{ad}) on the gold surface was calculated to be 0.78 ± 0.04 from integration of the Cu $2p_{3/2}$ and Au $4f_{7/2}$ peaks and the following equation: [27,28]

$$\phi_{ad} = \left\{ \left(\frac{I_{Au}}{I_{ad}} \right) \left(\frac{I_{ad}^{o}}{I_{Au}^{o}} \right) \left[1 - \exp\left(\frac{-a_{ad}}{\lambda_{ad(KE-ad)} \cos\Theta} \right) \right] + \left[1 - \exp\left(\frac{-a_{ad}}{\lambda_{ad(KE-Au)} \cos\Theta} \right) \right] \right\}^{-1} \qquad (7\text{-}1)$$

where I_{Au} and I_{ad} are the attenuated photoelectron intensities, I_{Au}^{o} and I_{ad}^{o} are the unattenuated intensities for bulk samples and the ratio of I_{ad}^{o} to I_{Au}^{o} is estimated using the ratio of their respective sensitivity factors, a_{ad} is the diameter of the adatom, Θ is the

angle of the detector with respect to the surface normal, $\lambda_{ad(KE\text{-}ad)}$ and $\lambda_{ad(KE\text{-}Au)}$ are the inelastic mean free paths through the adlayer for electrons with kinetic energy from the adlayer and the gold substrate, respectively.

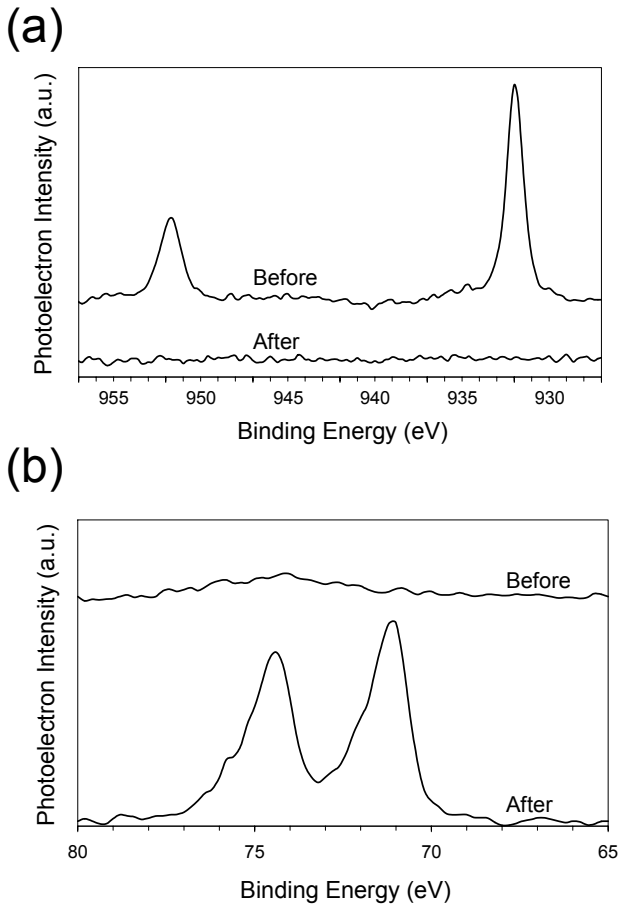

Figure 7.3. XPS spectra of gold substrates containing a copper submonolayer before and after exchange with platinum. (a) Cu (2p) region; (b) Pt (4f) region. The spectra have been offset vertically for clarity.

Copper-coated samples were immediately placed in a solution of 1.0 mM K_2PtCl_4 in 0.1 M H_2SO_4 (aq) for 5 min where the underpotentially deposited Cu layer was stoichiometrically exchanged with Pt. XPS spectra obtained after exposure to the Pt solution (Figure 7.3) show the complete diminution of Cu $2p_{3/2}$ and $2p_{1/2}$ peaks and the introduction of the Pt $4f_{7/2}$ and $4f_{5/2}$ peaks at 71 and 75 eV, respectively.[29,30] From

integrated XPS intensities for Pt $4f_{7/2}$ and Au $4f_{7/2}$ and Eq 7-1, we calculated the coverage of Pt on the gold surface as 1.06 ± 0.10, suggesting slightly more than a monolayer of Pt on the gold surface. The replacement of copper with platinum has been previously demonstrated to occur at a 1:1 stoichiometry.[17] Assuming a 1:1 exchange, the original 0.78 coverage of copper would equate to a coverage of 0.92 ± 0.05 for Pt due to its larger atomic diameter, which is in relative agreement with XPS in that an approximate monolayer of Pt is on the gold surface. The monolayer Pt coverage corresponds to a cathode catalyst loading of 0.5 μg/cm^2, which represents a reduction by three orders of magnitude when compared to conventional MEA cathode loadings of 0.5 mg/cm^2.[19]

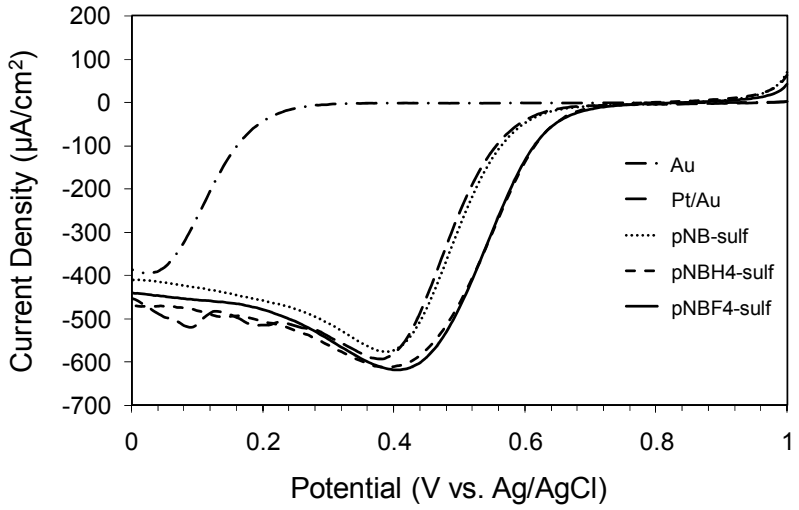

Figure 7.4. Voltammetric scans for oxygen reduction in O_2-saturated, 0.1 M H_2SO_4 (aq) for Au, Pt/Au, and the films indicated that were grown from Pt/Au.

Evaluation of ORR catalytic activity for this Pt/Au surface was monitored through cyclic voltammetry from 1,000 to 0 mV vs. Ag/AgCl/saturated KCl in O_2-saturated 0.1 M H_2SO_4(aq) (Figure 7.4). Consistent with previous reports,[14] the planar gold substrate

exhibits poor ORR catalytic activity (400 μA/cm^2, $E_{1/2}$ = 135 mV vs. Ag/AgCl). The addition of a submonolayer of platinum on the planar gold substrate increases the half-wave potential from 135 mV to 470 mV and increases the maximum current density (~600 μA/cm^2), consistent with the superior catalytic properties in oxygen reduction for Pt versus Au.

Modification of Pt/Au Electrodes

The exceptionally low Pt loadings and good performance hold promise for the efficient design of catalytic interfaces. Nonetheless, for interfaces in proton exchange membrane fuel cells, the modification of the electrode surface to tailor interfacial hydrophobicity and limit flooding while maintaining facile proton transport is essential for optimal performance. Here, we have investigated the effects of the surface-initiated growth of a proton-conducting polymer film from the Pt/Au interface on the catalytic performance of the Pt layer. Figure 7.5 shows the steps in the surface modification. After deposition of the Pt monolayer, the electrode is exposed to 4-mercaptobutanol to generate a 2-D sheet of hydroxyl functionality for further surface reactions (Figure 7.5a). In this process, the selection of 4-mercaptobutanol (HSC_4OH) is motivated by the fact that it forms a thin SAM that imparts little resistance against ion transfer but is sufficiently oriented to provide many hydroxyl groups for attachment of the norbornenyl diacid chloride in the next step. The use of shorter (2-mercaptoethanol) or longer (6-mercaptohexanol or 11-mercaptoundecanol) hydroxyl-terminated thiols resulted in decreased effectiveness. Figure 7.6 shows cyclic voltammograms for the oxygen

reduction reaction at a Pt/Au surface that was modified with HSC_4OH. Immediately after modification with HSC_4OH, the current and half wave potential of the reduction wave

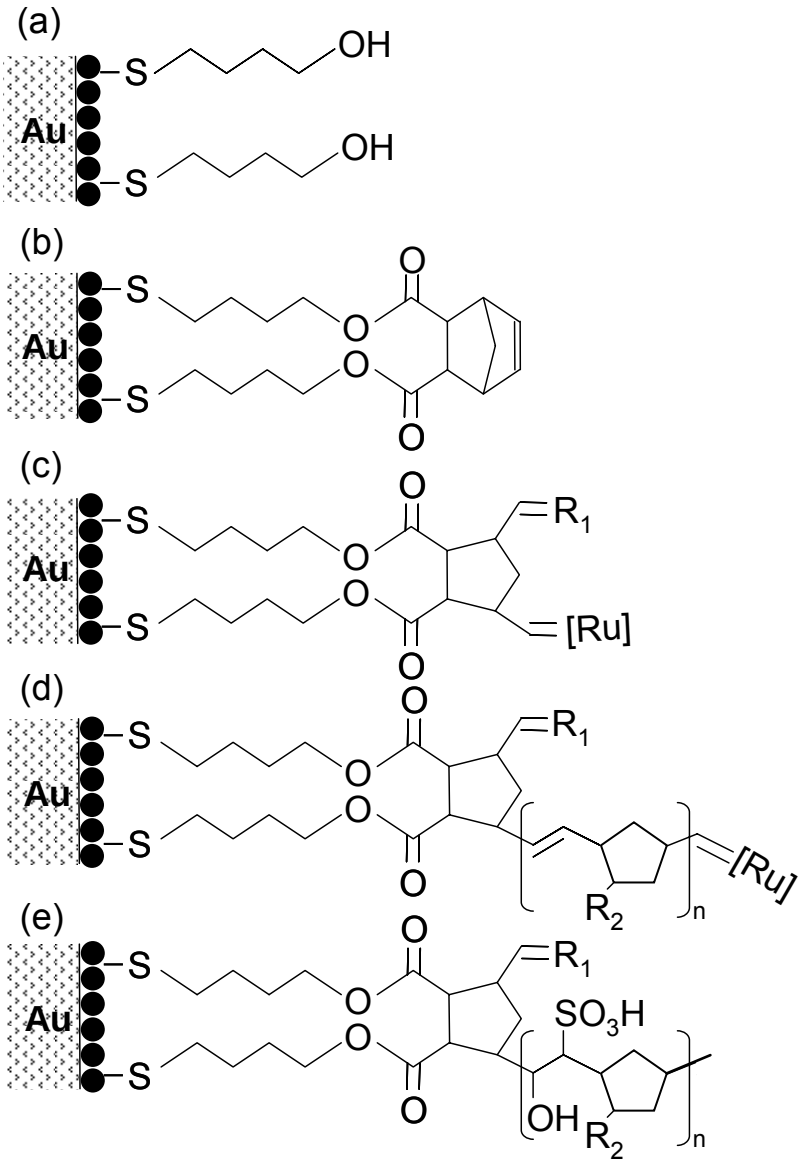

Figure 7.5. Process for preparing pNB (R_2 = H), pNBH4 (R_2 = -$(CH_2)_3CH_3$), and pNBF4 (R_2 = -$(CF_2)_3CF_3$) on Pt/Au substrates and the subsequent sulfonation of these films to achieve the hydroxyl sulfonate product. A self-assembled monolayer derived from HSC_4OH (a) is exposed to a norbornenyl diacidchloride (b) and Grubbs (I) or (II) catalyst, denoted as [Ru] (c) before exposure to the monomers to grow a surface-initiated polymer film of pNB, pNBH4, or pNBF4 (d) and subsequent sulfonation of the films in acetyl sulfate (e).

decrease from 600 μA/cm^2 and 470 mV, respectively (Figure 7.4), to 425 μA/cm^2 and 415 mV, respectively (Figure 7.6), but upon continued cycling, these values steadily improve. This behavior suggests that the SAM interferes with the catalytic performance of the Pt/Au electrode but is either partially or completely removed from the surface upon electrochemical cycling, as SAMs prepared from short-chained thiols have poor stability against electrochemical cycling.[24]

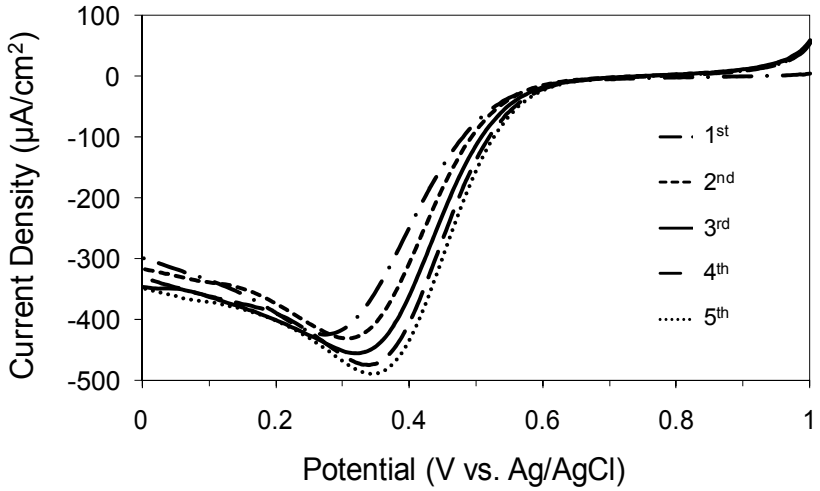

Figure 7.6. Voltammetric scans for oxygen reduction in oxygen-saturated, 0.1 M H_2SO_4(aq) for HOC_4S/Pt/Au. Shown are the 1st, 2nd, 3rd, 4th, and 5th scans. The improvement for each scan is due to the gradual removal of the SAM from the electrode to expose additional Pt sites for enhanced oxygen reduction.

To test if the SAM was still present after cycling, we exposed it to the proceding reagents (vide infra) for polymer initiation and growth and discovered that no polymer could be grown from the surface. Thus, the SAM is removed from the surface upon electrochemical cycling for the oxygen reduction reaction. Although we did not observe an electrochemical signal for the reduction of the thiolate from the Pt/Au surface, the large, broad reductive wave for oxygen reduction at the Pt/Au surface likely obscures the

reductive desorption of the thiolate. In addition, the thiolate could be removed by competitive interactions between O_2 and the Pt/Au surface. Under oxygenated conditions, bound thiolates can be converted to sulfonates[31] that bind weakly to Au, and presumably Pt/Au surfaces, and may be easily desorbed from the surface even at the low reducing potentials required for oxygen reduction. Nonetheless, this observation of SAM desorption is only detrimental to our processing if the polymer chains attached to the SAM are also removed (vide infra).

As a second step toward Pt/Au electrode functionalization, the hydroxyl-terminated monolayer was exposed to norbornenyl diacidchloride to generate ester-linked norobornenyl groups on the surface (Figure 7.5b). We have previously reported that ~90% of the norbornenyl groups are bound to the underlying SAM through both arms or two ester linkages.[2] These norbornenyl groups enable attachment of a suitable catalyst, such as Grubbs first- (I) or second-generation (II) catalysts (Figure 7.5c). Here, we use Grubbs (I) for growth of polynorbornene (pNB) or poly(butylnorbornene) (pNBH4) films but found Grubbs (II) to be much more effective for growth of poly(perfluorobutylnorbornene) (pNBF4) films. NBF4 could not be polymerized by a surface-anchored Grubbs (I) but grew rapidly when exposed to Grubbs (II)-modified surfaces. In contrast, NB and NBH4 grew to similar extents with Grubbs (I) or (II). The larger cross-section of the fluorocarbon group may sterically prevent close approach of NBF4 to the Ru active site of the Grubbs (I) catalyst. The Grubbs (II) catalyst is reported to provide more efficient polymerization of many functionalized norbornenes than the Grubbs (I) catalyst.[32]

The catalyst-coated surfaces were then exposed to a solution of NB, NBH4, or NBF4 for 15 min to grow hydrophobic polymer films from the surface (Figure 7.5d), followed by acetyl sulfate for 1-10 min to convert chain unsaturation along the backbone to a hydroxyl sulfonate product (Figure 7.5e). We have recently described the IR spectra for pNB and pNBH4 before[33] and after[2] sulfonation so that, here, we focus on the spectra for pNBF4 (Figure 7.7).

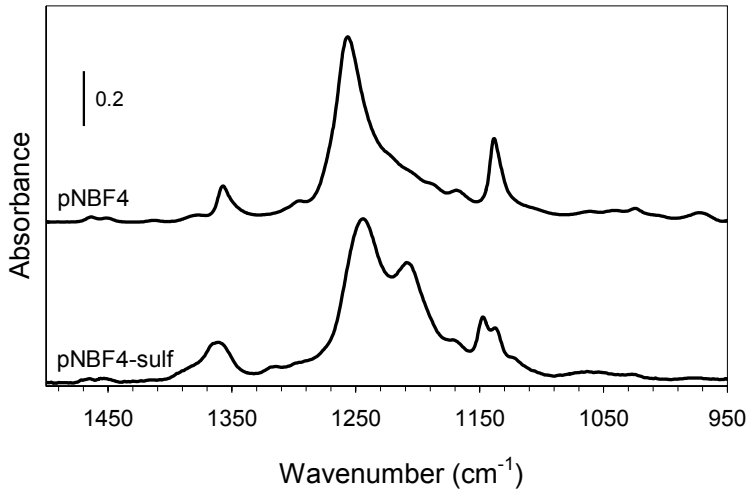

Figure 7.7. Reflectance-absorption infrared spectra for a ~140 nm pNBF4 film before and after sulfonation for 24 h.

Before sulfonation, the IR spectrum for pNBF4 exhibits peaks of absorbance for perpendicular C-F stretching modes at 1260 and 1138 cm^{-1}, as well as a peak for axial C-F stretching at 1360 cm^{-1}. The small peak at 968 cm^{-1} is due to trans C=CH out of plane bending, representing the olefin functionality along the backbone. After exposure to acetyl sulfate for 24 h, the small peak at 968 cm^{-1} due to olefin functionality disappears to indicate nearly complete conversion of the film to the hydroxylsulfonate product as shown schematically in Figure 7.5(e). The peak for the asymmetric stretching for

deprotonated SO_3 species appears at 1208 cm^{-1} and those for the asymmetric and symmetric stretching for protonated SO_3 species appear at 1363 and 1146 cm^{-1}, respectively. These peaks are shifted to slightly different wavenumbers in comparison to our previously reported values for sulfonated pNBH4 films,[2] which likely reflects the different microenvironment for these sulfonate groups in the different films. We do note that achieving this level of sulfonation for the pNBF4 film required 24 h exposure to 1.0 M acetyl sulfate in dichloromethane, much longer than the 1 min required for the sulfonation of pNB and pNBH4 films, as reported previously.

Table 7.1. Advancing Water Contact Angles of pNB, pNBH4, and pNBF4 Before and After Sulfonation.

	Before	After
Film	θ_A (°)	θ_A (°)
pNB	105 ± 1	79 ± 2
pNBH4	106 ± 2	92 ± 1
pNBF4	110 ± 2	86 ± 3

Prior to sulfonation, these polymer films are hydrophobic, yielding high water contact angles (Table 7.1), and they expectedly quench oxygen reduction activity due to their thickness and poor proton transfer properties. Upon sulfonation, the wettability increases for each film, as supported by decreases in the advancing water contact angles by 26°, 14°, and 24° for sulfonated forms of pNB, pNBH4, and pNBF4, respectively, as shown in Table 7.1. As a dense $-SO_3^-$ surface would be wet by water, the contact angles after sulfonation are consistent with surfaces that contain $-SO_3^-$ groups as well as other hydrophobic functionality, including cyclopentane and butyl or perfluorobutyl groups.

Electrochemical Characterization of Polymer Films

Figure 7.8a shows impedance spectra in the form of Bode plots for the three polymers (each ~50 nm thick) before and after sulfonation using 0.1 M H_2SO_4(aq) as a probing medium. These spectra have been fit with the equivalent circuit model shown in Figure 7.8b, which has time constants for the polymer film and the polymer/metal interface.[34] Before sulfonation, the spectrum for each film is consistent with predominately capacitive behavior where the conductive electrolyte is separated from the electrode by the polymer dielectric, which is modeled as a constant phase element (CPE_f) in Figure 7.8b to allow for film inhomogeneity.[35,36] These films exhibit a dense, hydrophobic barrier against the penetration of ions to provide a large resistance (R_f) against proton transfer, and the relative magnitude of the impedance for each film scales inversely with the CPE_f value of the films. In these cases, the film impedance dominates the spectrum so that the time constant for interfacial impedance is insignificant. CPE_f values (Table 7.2) decrease in the order of pNB > pNBH4 > pNBF4 for these films of similar thickness, suggesting that the fluorocarbon and hydrocarbon groups are imparting a lower dielectric constant to the film. The exponent for the CPE_f term (α_f) ranges from 0.928 for pNBF4 to 0.948 for pNB, indicating some deviation from a perfect capacitor ($\alpha_f = 1$), which may be due to the thinness that contributes some mild inhomogeneity to these films. Sulfonation of the chain unsaturation by acetyl sulfate (Figure 7.5e) provides dramatic changes to the impedance spectra, which indicate that the interfacial impedance becomes the dominant component in the circuit (Figure 7.8b) due to a greatly diminished polymer film resistance. The spectra for sulfonated films of pNBH4 and pNBF4 now

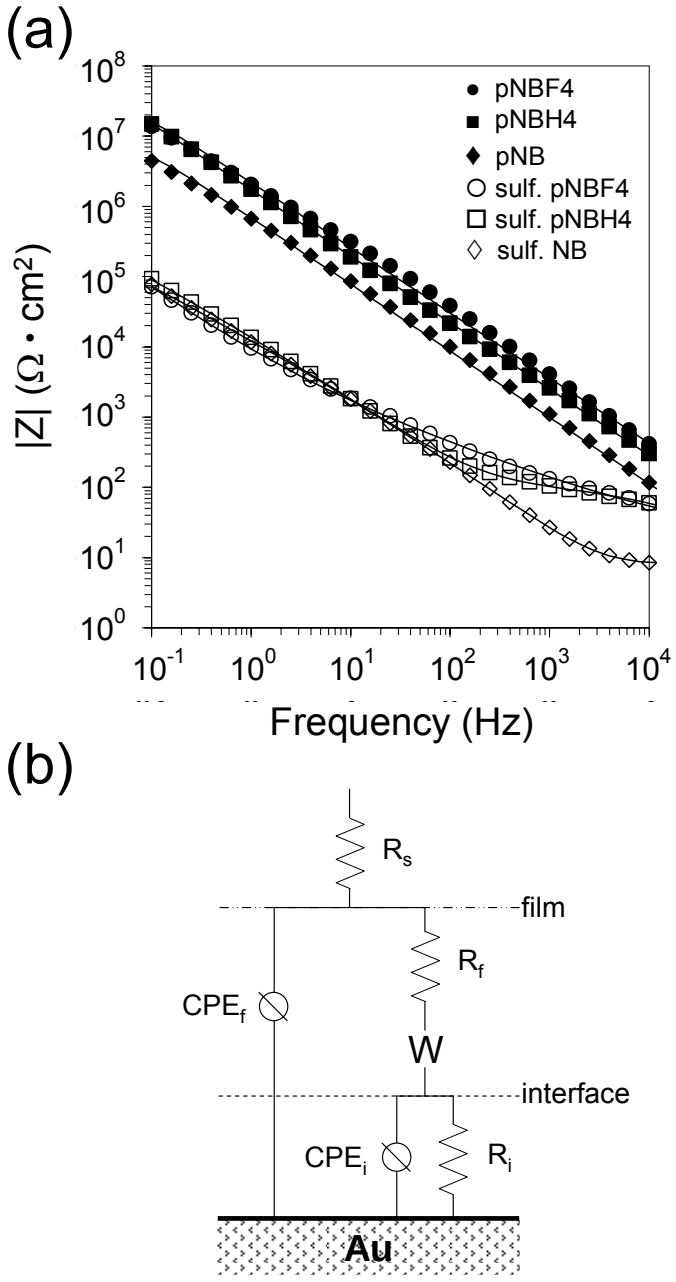

Figure 7.8. (a) Electrochemical impedance spectra in N_2-saturated, 0.1 M H_2SO_4 (aq) for ~50 nm films of pNB, pNBH4, and pNBF4 on Au before and after sulfonation. (b) Equivalent circuit model used to fit the impedance spectra and determine solution resistance (R_s), polymer film resistance (R_f), Warburg impedance (W), and interfacial resistance (R_i), in addition to constant phase elements for the polymer film (CPE_f) and the organic/metal interface (CPE_i).

show two time constants, including a resistive plateau at high frequencies that is due to the resistance of the film against proton transfer. The spectrum for sulfonated pNB does not show this second time constant because its resistance against proton transfer is sufficiently low that it cannot be distinguished from the solution resistance. We attribute the differences in resistances to the hydrophobic structuring that the side chains provide for sulfonated pNBH4 and pNBF4 films that limit the flux of protons to the electrode. At low to intermediate frequencies, the impedance spectra for all sulfonated films are nearly superimposable, reflecting the underlying SAM that binds all three polymers. In fact, $\alpha_i = 1$ for these interfaces, indicating ideal interfacial capacitors.

Table 7.2. Impedance Properties of Polymer Films Before and After Sulfonation

Film	R_f ($\Omega \cdot cm^2$)	CPE_f ($\mu S \cdot s^{\alpha} / cm^2$)	α_f	Warburg ($\mu S \cdot s^{-1/2} / cm^2$)	CPE_i ($\mu S \cdot s^{\alpha} / cm^2$)	α_i
pNB	1.0×10^7	254	0.948			
pNBH4	1.2×10^8	102	0.946			
pNBF4	3.7×10^7	83	0.928			
pNB-sulf	8			12000	5	1
pNBH4-sulf	88			453	7	1
pNBF4-sulf	24			102	26	1

The performance of the interfacial modifications on the Pt/Au electrode are revealed by examining the oxygen reduction reaction (Figure 7.4). All films improved substantially with cycling similar to the Au/Pt/SC_4OH monolayer, consistent with a similar desorption of the short-chain thiolates bound to the Pt/Au surface. Importantly, characterization of the polymer films after cycling revealed no changes in thickness or composition, indicating thiolates that tethered polymer were not lost from the interface. The loss of the short-chain thiolates and the preservation of the polymer-attached

thiolates are consistent with the additional stability of the longer chained adsorbates against reductive desorption[24] and importantly, provides a unique approach to "clean" the interface and eliminate the large fraction of adsorbates that do not bind ionomer but can block Pt sites. We observed the interfacial capacitance to increase by ~50% after the cycling, which again, is consistent with the removal of the short-chain thiolates.

To demonstrate the generality of this approach toward removal of short-chain thiolates at polymer/metal interfaces, Figure 7.9 shows reductive waves for Au/SC_4OH (no Pt), the same SAM after functionalization with norbornenyl diacidchloride, and the resulting surface after growing and sulfonating a ~50 nm film of pNB, all in deaerated, pH 8.3 phosphate buffer (aq). The –SC_4OH SAM is reductively desorbed as indicated by a sharp peak centered at -670 mV. Modification of the hydroxyl SAM by norbornenyl diacid chloride results in a much broader desorption peak, representing the presence of the different species on the surface: unreacted alcohol-terminated adsorbates and norbornene-terminated adsorbates in which the norbornene can be singly or doubly bound to the SAM. Growth of pNB and sulfonation result in a desorption peak that regains its sharpness but is shifted to -865 mV. Importantly, the polymer chains are still anchored to the surface after this desorption, so that the peak represents the selective removal of the short-chained species. Clearly, the presence of the polymer affects the potential required for desorption of these short-chained components but does not preclude their removal. These results on gold electrodes, in comparison with our removal of short chain components during oxygen reduction on Pt/Au electrodes, demonstrates a versatile way of desorbing unnecessary components from the ionomer/metal interface.

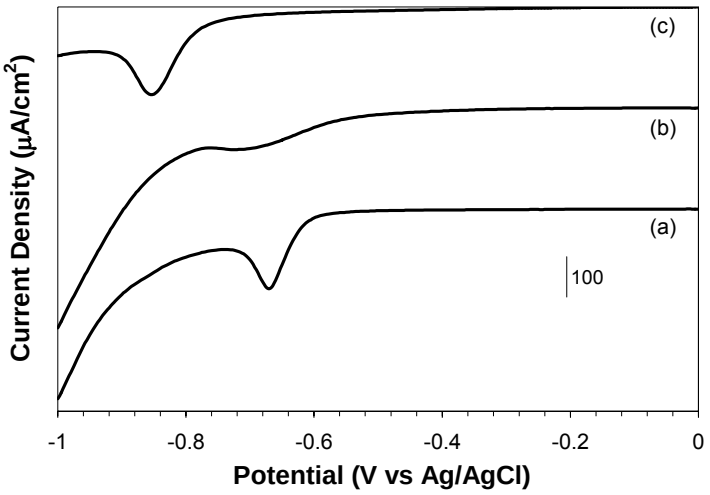

Figure 7.9. Voltammetric scans for the reductive desorption of short-chained thiolates for (a) a HOC_4S/Au SAM, (b) the film from (a) after modification with a norbornenyl diacidchloride, and (c) the surface from (b) after exposure to Grubbs (I) catalyst and a NB solution to grow pNB and the subsequent sulfonation of pNB to prepare a ~50 nm ionomer film. The scan rate was 200 mV/s. The solution consisted of pH 8.3, phosphate buffer (aq).

Given the improvement of all films with cycling, we report in Figure 7.4 the oxygen reduction waves for the films indicated on Pt/Au after a steady state current and potential were reached (at least 10 cycles). All sulfonated polymer films provide similar currents as unmodified Pt/Au, suggesting that the film does not provide a significant barrier against the transport of reactants to the interface beyond that of the aqueous electrolyte. The ionomer-coated films exhibit a more anodic half-wave potential than unmodified Pt/Au that scales with hydrophobicity, with $E_{1/2}$ for Pt/Au (470 mV) < PNB-sulf/Pt/Au (500 mV) < pNBH4-sulf/Pt/Au ≈ pNBF4-sulf/Pt/Au (550 mV). According to the Nernst equation,[37] the more anodic potential for the ionomer-coated electrodes signals a greater concentration of O_2 at the ionomer/electrode interface. We interpret these changes in $E_{1/2}$ as related to the improved partitioning and permeation of O_2 through the hydrophobic domains of the film. Although the pNBF4-sulf and pNBH4-sulf films provide a larger resistance against proton transfer than that of pNB-sulf, the hydrophobic

structuring enables enhanced partitioning of O_2 near the interface to boost half-wave potentials. While the hydrophobic chain length or extent of sulfonation has not been optimized in these studies, the results show that control over interfacial composition through surface-initiated routes can improve the performance of catalytic electrodes.

Conclusions

Through surface-initiated ROMP and subsequent sulfonation, we have demonstrated a bottom-up approach to fabricate ultrathin ionomer films with controlled side-chain hydrophobicity on Pt monolayer-modified Au substrates. The Pt monolayer remains affixed to the substrate and catalytically active during the modification steps. The sulfonated films with hydrophobic side groups (pNBH4-sulf and pNBF4-sulf) exhibit increased resistances against proton transfer but more anodic half-wave potentials for oxygen reduction, consistent with an improved partitioning of O_2 near the polymer/electrode interface. The surface-initiated polymer chains were tethered to the surface via short-chained thiolates. The unreacted short-chain components, those that did not tether polymer, were removed electrochemically without disturbing the polymer film to effectively clean the catalyst surface of these short-chain contaminants.

References

1. Creager, S. E.; Liu, B.; Mei, H.; DesMarteau, D., Electrochemical Grafting of an Aryl Fluorosulfonimide Electrolyte onto Glassy Carbon. *Langmuir* **2006**, 22, 10747-10753.

2. Berron, B. J.; Payne, P. A.; Jennings, G. K., Sulfonation of Surface-Initiated Polynorbornene Films. *Industrial & Engineering Chemistry Research* **2008**, 47, 7707-7714.

3. Kuroki, H.; Yamaguchi, T., Nanoscale Morphological Control of Anode Electrodes by Grafting of Methylsulfonic Acid Groups onto Platinum-Ruthenium-Supported Carbon Blacks. *Journal of the Electrochemical Society* **2006**, 153, A1417-A1423.

4. Carrette, L.; Friedrich, K. A.; Stimming, U., Fuel Cells: Principles, Types, Fuels, and Applications. *ChemPhysChem* **2000**, 1, 162-193.

5. Lister, S.; McLean, G., PEM Fuel Cell Electrodes. *Journal of Power Sources* **2004**, *130*, 61-76.

6. Jennings, G. K.; Brantley, E. L., Physicochemical properties of shurface-initiated polymer films in the modification and processing of materials. *Adv. Mater*. **2004**, 16, 1983-1994.

7. Jordi, M. A.; Seery, T. A. P., Quantitative determination of the chemical composition of silica-poly(norbornene) nanocomposites. *J. Am. Chem. Soc*. **2005**, 127, 4416-4422.

8. Buchmeiser, M. R., Metathesis polymerization to and from surfaces. In Surface-Initiated Polymerization I **2006**; Vol. 197, pp 137-171.

9. Yang, Q.; Wang, L.; Xiang, W. D.; Zhou, J. F.; Tan, Q. H., Preparation of polymer-grafted carbon black nanoparticles by surface-initiated atom transfer radical polymerization. *Journal of Polymer Science Part a-Polymer Chemistry* **2007**, 45, 3451-3459.

10. Huang, W.; Kim, J.-B.; Bruening, M. L.; Baker, G. L., Functionalization of Surfaces by Water-Accelerated Atom-Transfer Radical Polymerization of Hydroxyethyl Methacrylate and Subsequent Derivatization. *Macromolecules* **2002**, 35, 1175-1179.

11. Singh, N.; Wang, J.; Ulbricht, M.; Wickramasinghe, S. R.; Husson, S. M., Surface-Initiated Atom Transfer Radical Polymerization: A New Method for Preparation of Polymeric Membrane Absorbers. *J. Membrane Science* **2008**, 309, 64-72.

12. Rutenberg, I. M.; Scherman, O. A.; Grubbs, R. H.; Jiang, W.; Garfunkel, E.; Bao, Z., Synthesis of Polymer Dielectric Layers for Organic Thin Film Transistors via Surface-Initiated Ring-Opening Metathesis Polymerization. *J. Am. Chem. Soc.* **2004**, 126, 4062-4063.

13. Middelman, E., Improved PEM Fuel Cell Electrodes by Controlled Self-Assembly. *Fuel Cells Bulletin* **2002**, November, 9-12.

14. Kongkanand, A.; Kuwabata, S., Oxygen Reduction at Platinum Monolayer Islands on Au(111). *J. Phys. Chem. B* **2005**, 109, 23190-23195.

15. Zhang, J.; Vukmirovic, M. B.; Xu, Y.; Mavrikakis, M.; Adzic, R. R., Controlling the Catalytic Activity of Platinum-Monolayer Electrocatalysts for Oxygen Reduction with Different Substrates. *Angew. Chem. Int. Ed.* **2005,** 44, 2132-2135.

16. Cha, S. Y.; Lee, W. M., Performance of Proton Exchange Membrane Fuel Cell Electrodes Prepared by the Direct Deposition of Ultrathin Platinum on the Membrane Surface. *J. Electrochem. Soc.* **1999,** 146, 4055-4060

17. Brankovic, S. R.; Wang, J. X.; Adzic, R. R., Metal Monolayer Deposition by Replacement of Metal Adlayers on Electrode Surfaces. *Surface Science* **2001,** 474, L173-L179.

18. Kolb, D. M., Physical and Electrochemical Properties of Metal Monolayers on Metallic Substrates. In *Advances in Electrochemistry and Electrochemical Engineering*, Gerischer, H.; Tobias, C. W., Eds. Wiley: New York, 1978; Vol. 11, pp 125-275.

19. Zeis, R.; Mathur, A.; Fritz, G.; Lee, J.; Erlebacher, J., Platinum-Plated Nanoporous Gold: An Efficient, Low Pt Loading Electrocatalyst for PEM Fuel Cells. *J. Power Sources* **2007,** 165, 65-72.

20. Liu, P.; Ge, X.; Wang, R.; Ma, H.; Ding, Y., Facile fabrication of ultrathin pt overlayers onto nanoporous metal membranes via repeated Cu UPD and in situ redox replacement reaction. *Langmuir* **2009,** 25, 561-567.

21. Friebe, A.; Ulbricht, M., Controlled pore functionalization of poly(ethylene terephthalate) track-etched membranes via surface-initiated atom transfer radical polymerization. *Langmuir* **2007,** 23, 10316-10322.

22. Lau, K. H. A.; Duran, H.; Knoll, W., In situ Characterization of N-Carboxy Anhydride Polymerization in Nanoporous Anodic Alumina. *Journal of Physical Chemistry B* **2009,** 113, 3179-3189.

23. Walczak, M. M.; Alves, C. A.; Lamp, B. D.; Porter, M. D., Electrochemical and X-ray photoelectron spectroscopic evidence for differences in the binding sites of alkanethiolate monolayers chemisorbed at gold. *J. Electroanal. Chem.* **1995,** 396, 103-114.

24. Munakata, H.; Oyamatsu, D.; Kuwabata, S., Effects of w-Functional Groups on pH-Dependent Reductive Desorption of Alkanethiol Self-Assembled Monolayers. *Langmuir* **2004,** 20, 10123-10128.

25. Perez, E.; Laval, J. P.; Bon, M.; Rico, I.; Lattes, A., Synthesis of bicyclo [2· 2· 1] hept-2-enes with mono and disubstituted long perfluorinated chains C_nF_{2n+1} (n = 4,6,8,10) Investigation of association in solution by 19F NMR study of polymerization via a metathetic reaction. *Journal of Fluorine Chemistry* **1988,** 39, 173-196.

26. Tran, Y.; Auroy, P., Synthesis of poly(styrene sulfonate) brushes. *Journal of the American Chemical Society* **2001,** 123, 3644-3654.

27. Jennings, G. K.; Laibinis, P. E., Self-Assembled n-Alkanethiolate Monolayers on Underpotentially Deposited Adlayers of Silver and Copper on Gold. *J. Am. Chem. Soc.* **1997,** 119, 5208-5214.

28. *Practical Surface Analysis: By Auger and X-Ray Photoelectron Spectroscopy*; Briggs, D.; Seah, M. P., Eds.; Wiley: New York, 1983.

29. Manolova, M.; Ivanova, V.; Kolb, D. M.; Boyen, H. G.; Ziemann, P.; Buttner, M.; Romanyuk, A.; Oelhafen, P., Metal deposition onto thiol-covered gold: Platinum on a 4-mercaptopyridine SAM. *Surface Science* **2005,** 590, 146-153.

30. Mason, M. G., Electoronic-Structure of Supported Small Metal-Clusters. *Physical Review B* **1983,** 27, (2), 748-762.

31. Laibinis, P. E.; Whitesides, G. M., Self-Assembled Monolayers of n-Alkanethiolates on Copper are Barrier Films that Protect the Underlying Metal Against Oxidation by Air. *J. Am. Chem. Soc.* **1992,** 114, 9022-9027.

32. Trnka, T. M.; Grubbs, R. H., The Development of L2X2Ru=CHR Olefin Metathesis Catalysts: An Organometallic Success Story. *Ac. Chem. Res.* **2001,** 34, 18-29.

33. Berron, B. J.; Graybill, E. P.; Jennings, G. K., Growth and Structure of Surface-Initiated Poly(n-alkylnorbornene) Films. *Langmuir* **2007,** 23, 11651-11655.

34. Brantley, E. L.; Holmes, T. C.; Jennings, G. K., Modification of Poly(hydroxyethyl methacrylate) Films with Hydrocarbon Side Chains. *J. Phys. Chem. B* **2004,** 108, 16077-16084.

35. *Impedance Spectroscopy: Theory, Experiment, and Applications*; Second ed.; Barsoukov, E.; Macdonald, J. R., Eds.; Wiley-Interscience: Hoboken, N.J., 2005.

36. Smith, M. B.; Tong, J. H.; Genzer, J.; Fischer, D.; Kilpatrick, P. K., Effects of synthetic amphiphilic alpha-helical peptides on the electrochemical and structural properties of supported hybrid bilayers on gold. *Langmuir* **2006,** 22, 1919-1927.

37. Bard, A. J.; Faulkner, L. R. *Electrochemical Methods: Fundamentals and Applications*; Second ed.; Wiley: New York, 2001.

CHAPTER VIII

SURFACE-INITIATED RING-OPENING METATHESIS POLYMERIZATION OF 5-(PERFLUOROHEXYL)NORBORNENE ON CARBON PAPER

Introduction

Surface-initiated polymerization (SIP) is a commonly used method for coating complex, three dimensional substrates with ultrathin polymer films.[1-3] Conformal polymer coatings on irregular surfaces, such as porous supports or fibrous meshes, cannot be obtained using spin-coating or solution-casting methods due to the nature of these techniques in which the polymer is topically applied to substrates. Since the inner dimensions of porous supports are not easily accessible, they are often left bare when using classical coating or casting methods. However, in SIP, a bottom-up approach is used in which the monomer reacts with a surface-tethered initiator or polymerization catalyst, resulting in the growth of a polymer chain from the surface.[4, 5] A wide variety of polymerization techniques such as ionic, living radical, and ring-opening polymerizations are applicable as surface-initiated approaches provided that an appropriate initiator can be anchored to the surface.[1] Thus, desired polymer properties can be imparted to a wide variety of surfaces and geometries by growing thin polymer films from these surfaces. The precise control and tunability of film properties on the molecular scale afforded by SIP methods enables excellent control over film functionality and thickness ranging from a few nm to microns.[6, 7] SIP allows functionalization and modification of a variety of substrates including nanoscale structures and particles,[8-10] pourous supports,[11, 12] and separations media.[13, 14] SIPs are particularly advantageous in coating largely unreactive

surfaces, such as carbon supports, due to the forgiving nature of polymer film growth. For example, Qin et al. demonstrated that only 1 in ~250 carbon sites needs to be catalytically active to grow a complete polymer coating on carbon nanotubes (CNT), whereas 1 in 10 carbons needs to be coated with monolayer modifications to achieve desired functionality.[8]

In this chapter, we discuss the surface-initiated growth of poly(5-(perfluorohexyl)norbornene) (pNBF6) films on carbon paper electrodes. These functionalized electrodes have applications in chemical[15] and biological sensing,[16] separations,[17] or catalysis due to their selectivity in mitigating the transfer of hydropohobic and ionic species upon sulfonation. A bottom-up approach is preferred because presynthesized bulk polymer would be restricted from conformally coating the carbon fibers within the inner dimensions of the carbon paper, leading to underutilized electrochemically active area. We have previously demonstrated surface-initiated growth of poly(5-(perfluoro-n-alkyl)norbornenes (pNBFn) films on planar gold electrodes.[18] These films exhibit rapid growth kinetics with low critical surface energies while providing an effective barrier to the diffusion of aqueous ions.[18] pNBFn films can be converted to ionomer films through exposure to 0.1 M acetyl sulfate solution in dichloromethane reacting the olefin residing in the polymer backbone to yield a sulonate group.[19, 20] Upon sulfonating these films, the ability to transport protons and aqueous ions improves by at least 4 orders of magnitude.[19] Integrating the sulfonated fluoro-ionomer film with a Pt-coated gold electrode enhanced the half-peak potential of oxygen reduction reaction by 17% over that of an unmodified Pt/Au electrode.[19] Here, we employ the surface-initiated ring-opening metathesis polymerization (SI-ROMP) of 5-

(perfluorohexylnorbornene) (NBF6), as a route towards ultrathin fluoro-polymer coatings of carbon paper substrates.

Carbon paper is an attractive substrate as it provides a 3D, high surface area porous electrode at reasonable cost with commercially available comparisons, such as poly(tetrafluoroethylene) (PTFE)-coated carbon paper.[21, 22] PTFE-coated carbon fibers are primarily used as hydrophobic protective coatings and membranes to prevent water build-up while promoting gas diffusion at the electrodes in proton exchange membrane fuel cells.[21] However, these coatings are typically made in high vacuum environments at elevated temperatures using laser ablation techniques or chemical vapor deposition techniques.[23] In comparison, our approach using SI-ROMP of NBF6 to grow fluorocarbon polymer films from carbon fibrous supports is performed under ambient conditions while exhibiting rapid kinetics. Additionally, pNBF6 has the potential of translating to an ionomer film via sulfonation of the olefin residing in the backbone of the polymer chain. Herein, we compare the barrier properties of pNBF6 films and commercial PTFE films on carbon paper against the transport of aqueous ions. The effects of initiator concentration on the extent of pNBF6 film growth are also discussed.

Experimental Procedures

pNBF6 Film Preparation

Carbon paper was exposed to O_2 plasma (Harrick PDC-23G plasma cleaner, low power, 150 mTorr) to yield hydroxyl moieties on the surface depicted in Figure 1(a). The films were immediately placed in a 5 mM solution of trans-3,6-endo-methylene-1,2,3,6-tetrahydrophthaloyl chloride in dichloromethane for 30 min to yield the acylation product

of a surface-tethered norbornenyl group, Figure 1(b).[24] The samples were rinsed in dichloromethane and ethanol and dried in a stream of N_2. The norbornenyl decorated substrates were exposed to a 5 mM solution of Grubbs (II) catalyst in dichloromethane for 10 min to anchor the catalyst to the substrate as seen in Figure 1(c). The monolayers were rinsed with dichloromethane and immediately placed in a monomer solution containing 0.05 M NBF6 in dichloromethane for 10 min to grow pNBFn films, shown in Figure 1(d). Carbon paper samples were typically cut to 1 cm x 4 cm pieces.

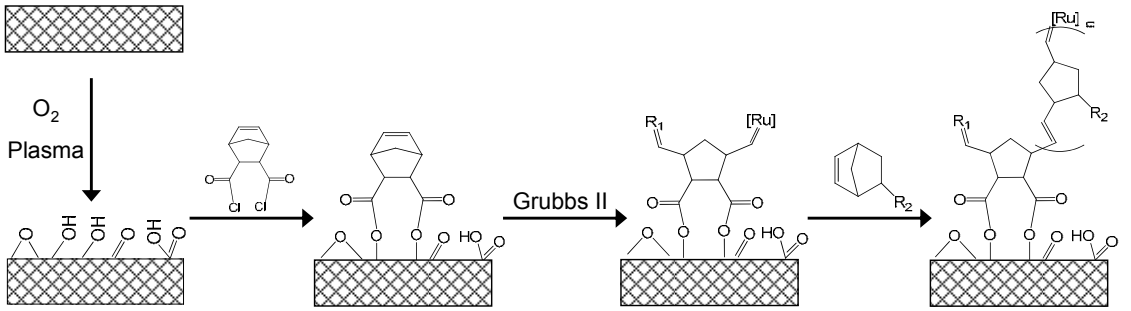

Figure 8.1. SI-ROMP reaction schematic of perfluoro-alkylnorbornenes on carbon paper. A carbon surface is modified with O_2 plasma and initiated using trans-5-norbornene-2,3-dicarbonyl chloride. The initiator is activated by Grubbs 2nd Generation catalyst, denoted as [Ru], and exposed to the NBF6 monomer solution. R2 = $-C_6F_{13}$ and R1 represents CHPh.

Results and Discussion

Films of poly(5-(perfluorohexyl)norbornene) (pNBF6) were grown from O_2-plasma-treated carbon paper utilizing SI-ROMP as depicted in Figure 8.1. The plasma-treated paper was exposed to 1 mM trans-3,6-endo-methylene-1,2,3,6-tetrahydrophthaloyl chloride in dichloromethane (DCM) for 60 min to produce an ester-linked norbornene group on the surface. This tethered norbornene acts as an anchor for the polymerization catalyst, Grubbs 2nd generation catalyst (Grubbs II). The resulting surface was made catalytically active for ROMP by exposure to 5 mM Grubbs 2nd

generation catalyst in DCM for 5-10 min. Subsequent exposure to NBF6 in DCM for 10 min resulted in the growth of partially fluorinated polymer films from the surface.

This polymerization scheme takes advantage of anchoring the initiator (Grubbs II) using a surface-tethered norbornene via acylation of hydroxyl termini. Previously, we utilized self-assembled monolayers of $HS(CH_2)_4OH$ to achieve a hydroxyl terminated surface to bind trans-3,6-endo-methylene-1,2,3,6-tetrahydrophthaloyl chloride to the surface. However, SAMs take advantage of sulfur's affinity for metals such as copper, silver, gold, and platinum and do not bind to non-metal substrates. Thus, for silicon-based substrates like glass, and silicon wafers, a hydroxyl terminus can be achieved by etching the surfaces with a hydrogen peroxide and sulfuric acid solution. To achieve hydroxyl termini on a carbon surface, strong oxidizing agents are necessary as well. Others have achieved oxidation of a carbon substrate via exposure to strong acids such as concentrated sulfuric and nitric acids.[25-27] However, the harsh conditions of the acid treatment can induce heavy erosion of the carbon substrate, while providing only a low yield in surface coverage of hydroxyl moieties. Yields as high as ~45 % are possible; however, the procedures are cumbersome and require at least 24 h exposure to concentrated acids. Exposing carbon fibers to oxygen-rich environments at elevated temperatures also oxidizes the surface; however, this method predominately produces carboxylic acid groups.[26] Here, we chose to utilize an O_2 plasma to oxidize the carbon fibers to achieve hydroxyl termini since the integrity of the carbon fibers can be maintained while generating a reasonable yield of hydroxyl functionality within a few minutes.[28]

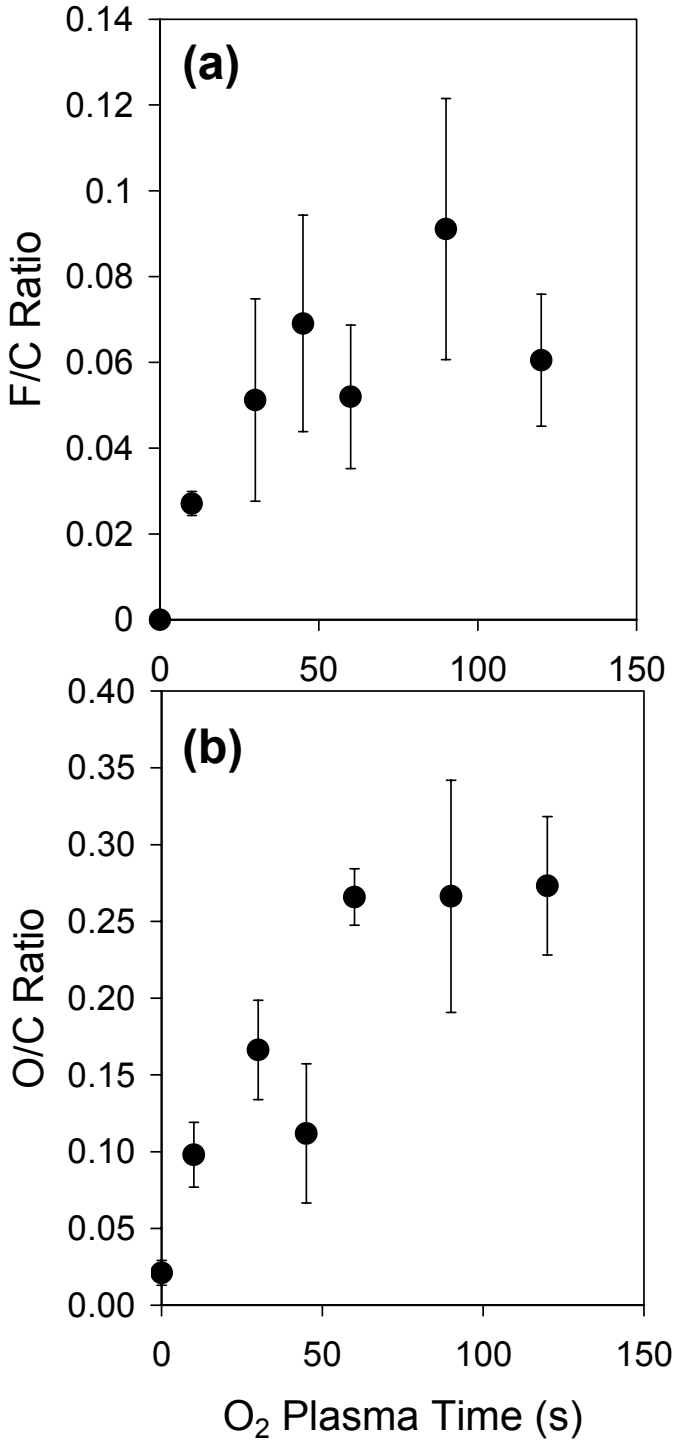

Figure 8.2. The fluorine to carbon ratio, (a), on the surface of fluorine functionalized carbon paper, and oxygen to carbon, (b), ratio on the surface of plasma treated carbon paper as determined via integration of the F(1s), O(1s), and C(1s) peaks in XPS.

Upon exposing the carbon paper to O_2 plasma, not only are –OH functionalities formed, but also a variety chemical moieties with varying degrees of oxidation. Quinones, carbonyls, carboxylic acids, and radicals are formed in conjunction with the preferred hydroxyl functionality.[26] Yuan et al. demonstrated that the degree and type of oxidation of carbon fibers fluctuates depending on the length of exposure to O_2 plasma.[28] They concluded that extended O_2 plasma exposure eroded the carbon surface causing the concentrations of oxidized species to fluctuate cyclically. Thus, extended plasma exposure does not yield more functionalization of the carbon surface. To investigate the optimal plasma exposure time that yields the highest surface concentration of hydroxyl termini for our systems, we characterized the acylation product of pentadecafluorooctanoyl chloride and the O_2-treated carbon paper using XPS. We utilize the fluorinated acid chloride as a tag because of the high intensity of the F(1s) signal in XPS. The attachment mechanism of the fluorinated acid chloride is also directly comparable to the chemistry employed to attach trans-3,6-endo-methylene-1,2,3,6-tetrahydrophthaloyl chloride to the carbon paper surface as an initiator for SI-ROMP of NBF6. Samples that yield a higher F/C count ratio in the XPS spectrum indicate that more hydroxyl moieties were produced during the plasma treatment. As indicated in Figure 2a, short times, < 30 s, are insufficient to saturate the surface with hydroxyl termini, and extended times > 60 s do not provide more acylation product. Indeed, we observed saturation in surface oxidation after 60 s, as indicated by the O/C count ratio shown in Figure 2b.

Scanning electron microscopy (SEM) was used to investigate the coverage of pNBF6 films grown from carbon paper that was exposed to different plasma treatment

times. Figure 8.3(a) displays the micrograph for untreated carbon paper. As can be seen, the surface of the carbon fibers is rough and fibrillar in nature. Upon O_2-plasma exposure excess particles are removed and the ridges become more uniform.[28] As a control, we exposed Grubbs (II)-modified carbon paper, which had no plasma treatment, to 50 mM of NBF6 for 15 min resulting in very little polymer growth on the film, shown in Figure 3(b).

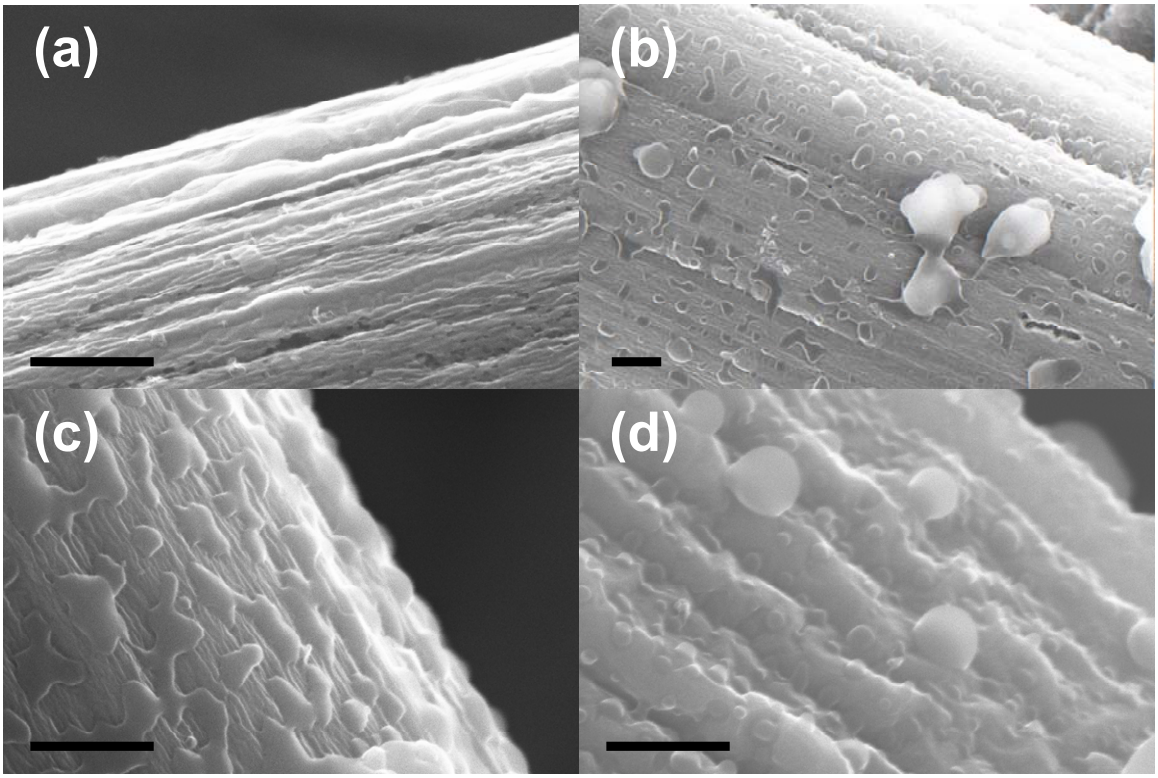

Figure 8.3. Scanning electron micrographs of (a) unmodified carbon paper, (b) pNBF6 grown on unmodified carbon paper, (c) pNBF6 grown on 10 s O_2 plasma treated carbon paper, and (d) pNBF6 grown on 45 s O_2 plasma treated carbon paper. The scale bar indicates 500 nm.

The majority of the polymer aggregates seen in Figure 8.3(b) are due to NBF6 polymerizing in solution and adsorbing onto the carbon fibers. The SEM micrograph of carbon fibers that were plasma-treated for 10 s and exposed to 50 mM NBF6 for 15 min

is shown in Figure 8.3(c), displaying sparse isolated islands of polymer. The smooth regions in the image represent pNBF6 whereas the fibrillar structure is indicative of the carbon fiber surface, also shown in Figure 8.3(a). The resulting sparse polymer film growth is consistent with a lack of initiation sites as indicated by the XPS data. The F/C ratio at 10s in Figure 8.2(a) suggests that the carbon fiber surface has been effectively functionalized but not saturated. Thus, SI-ROMP of NBF6 does occur, just not enough to yield a complete or coherent film. However, carbon fibers that have attained sufficient amounts of –OH groups, yield complete pNBF6 films upon exposure to NBF6 as shown in Figure 8.3(d). This image displays the SEM micrograph of pNBF6 grown on carbon paper that was exposed to O_2 plasma for 45 s. The pNBF6 film exhibits hemispherical structures on the scale of 20-50 nm with some features much larger. These smaller structures are similar to those we previously observed in pNBFn films on planar polycrystalline gold surfaces.[18]

We used RAIRS to confirm the growth and structure of the pNBF6 films. Although carbon substrates would not seem conducive to reflectance mode FTIR, we are not the first to use RAIRS to investigate chemical moieties on carbon fibers. For example, Zhu et al. used RAIRS to verify the presence of oxygen functional groups on the carbon fibers after plasma-treatment.[29] Figure 8.4 displays the fluorocarbon region of the RAIR spectrum for a pNBF6 film grown on carbon paper. The CF_2 stretching modes absorb strongly from 1100-1400 cm^{-1}. Due to the helical structure of fluoroalkyl chains, two types of CF_2 stretching peaks are expected in the IR: those lying along the helical axis ($\nu_{ax}CF_2$, 1300-1400 cm^{-1}) and those oriented perpendicular to the helical axis ($\nu_{pd}CF_2$, 1100-1300 cm^{-1}).[17-19]

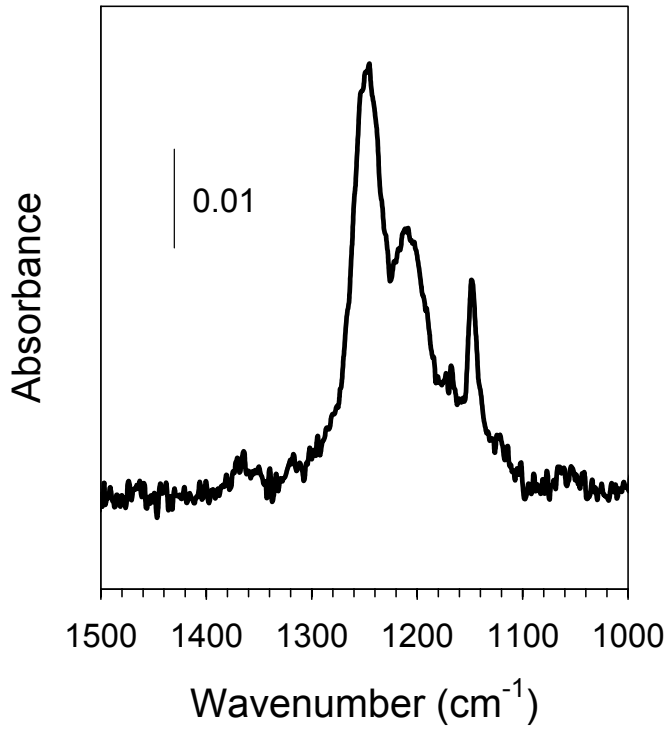

Figure 8.4. Reflectance absorption infrared spectrum of pNBF6 grown on carbon paper.

As expected, the pNBF6 film greatly enhances the hydrophobicity and the oleophobicity of the carbon paper. Table 8.1 summarizes the advancing water contact angles atop the carbon paper after each stage of the polymerization process shown in Figure 8.1. The advancing contact angle for water is well above the ~120° expected for a smooth fluorocarbon surface due to the innate roughness and porosity of the carbon fiber substrate, and is comparable to the PTFE-coated carbon paper. The inflated contact angles can be described using an expression developed by Wenzel[30]:

$$\cos\theta_W = r\cos\theta_s \tag{8-1}$$

where θ_W is the Wenzel contact angle, r is a roughness factor, and θ_s is the contact angle measured on a homogeneous surface. Thus, if a smooth surface yields an

advancing contact angle > 90°, a rough surface of the same composition is expected to have a greater contact angle than the smooth substrate. However, if a smooth surface yields a contact angle < 90°, a roughened surface will yield a contact angle less than the smooth substrate. Using Equation 8-1 and the advancing water contact angles in Table 1, the Wenzel roughness factor can be estimated to be ~1.7.

Table 8.1. Impedance properties and advancing contact angles of unmodified, plasma-treated, Teflon-treated, and pNBF6-coated carbon paper electrodes obtained in 1 mM $K_3Fe(CN)_6$ and 1 mM $K_4Fe(CN)_6$ in 0.1 M Na_2SO_4(aq). θ_A represents the advancing water contact angle atop the samples.

Sample	log (R_f (Ω·cm^2))	CPE_f (mS*s$^{\alpha}$)	α	θ_A
Unmodified	2.8	174	0.703	134 ± 2
Plasma-treated	1.2	108	1	0
Initiator	—	—	—	52 ± 25
Teflon-treated	3.7	17	0.825	145 ± 2
pNBF6-coated	4.0	3.1	0.916	154 ± 4

Hexadecane is a more sensitive probing contact liquid on fluorocarbon surfaces as small changes in fluorocarbon functionality yield large changes in the contact angle. The advancing hexadecane contact angle (θ_{HD}) on smooth -CF_2-, such as PTFE, is expected to be ~50°,[31] while a surface comprised of dense –CF_3 groups yields a θ_{HD} of ~83°.[32] Since these values are less than 90° coupled with the low surface tension of HD and the roughness and porosity of the carbon fibrous mesh network, all samples absorbed the hexadecane droplet upon exposure. The hexadecane droplet was maintained on top of the pNBF6-coated carbon paper for ~10s before the droplet was absorbed, whereas, the droplet was immediately absorbed into untreated, plasma-treated, and PTFE-treated carbon paper.

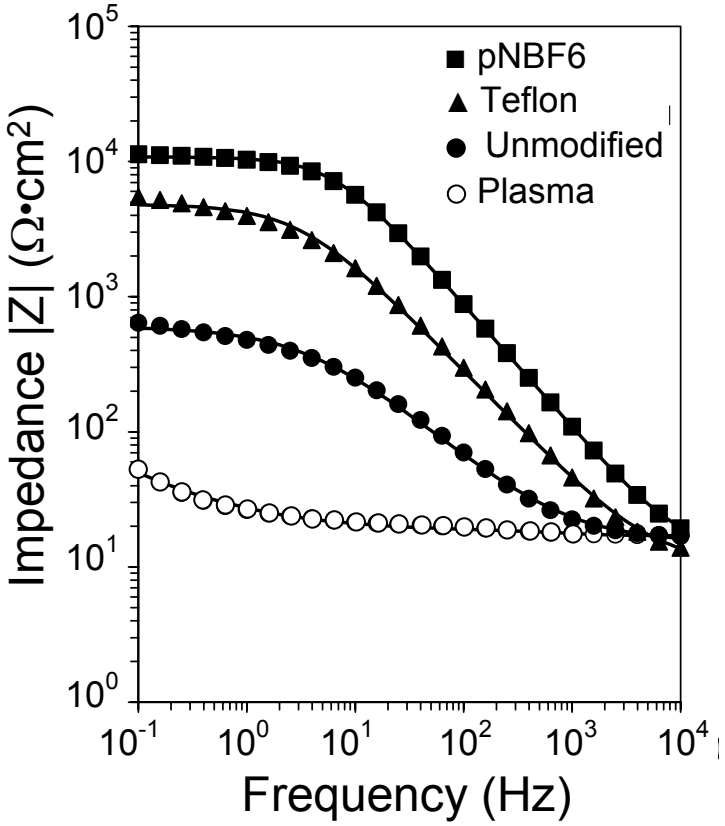

Figure 8.4. Electrochemical impedance spectra obtained in 1 mM $K_3Fe(CN)_6$ and 1 mM $K_4Fe(CN)_6$ in 0.1 M Na_2SO_4(aq) for the indicated films on carbon paper. Solid curves represent fits of the data using appropriate equivalent circuit models depicted in Figure 8.6. The area cited in the figure is geometric area not active surface area of the electrodes.

The pNBF6 film on the carbon paper provides protective coating in an aqueous environment. We used electrochemical impedance spectroscopy to investigate the barrier properties of the pNBF6 films in the presence of $K_3Fe(CN)_6$ and $K_4Fe(CN)_6$ in 0.1 M Na_2SO_4(aq). Representative Bode plots for unmodified carbon paper, plasma-treated carbon paper, pNBF6-coated carbon paper, and commercially available PTFE-coated carbon paper are shown in Figure 8.5. As indicated by the order of magnitude reduction in impedance, O_2-plasma treatment of the carbon paper effectively cleans and oxidizes the surface, creating a double layer of capacitance of 108 $\mu F/cm^2$ at lower frequencies. The pNBF6 film and the Teflon-coated sample exhibit 10^3 improvement beyond the

plasma-treated carbon paper electrode. The increased impedance of these films can be attributed to the enhanced hydrophobicity and protection provided by the fluorocarbon films.

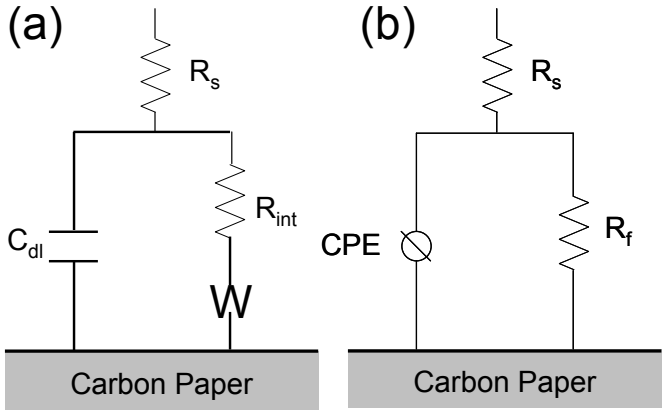

Figure 8.5. Equivalent circuits used to model impedance spectra for films on carbon paper electrodes: (a) mixed kinetic and charge transfer model and (b) the Randles circuit model modified with a constant phase element. The constant phase element allows for film inhomogeneity and the modeling of "leaky" capacitors.

The plasma-treated carbon paper can be modeled using a double layer capacitance in parallel with a Warburg impedance, shown in Figure 8.6a, to account for diffusional limitations at low frequencies. The untreated, Teflon-treated, and pNBF6-coated carbon paper were modeled using a modified Randle's circuit, Figure 8.6b. Capacitors were replaced with constant phase elements (CPE) to allow for film inhomogeneity.[33, 34] The film inhomogeneity may be due to varying film thickness throughout the fibrous network. Since film capacitance is inversely proportional to the thickness of a film, variability in the thickness can result in the film behaving as a "leaky" capacitor. This leakiness is accounted for in the parameter α, where $\alpha = 1$ for a true capacitor. The pNBF6-coated film exhibits a lower capacitance, 3.1 $\mu S \cdot s^{\alpha}$ (where $\alpha = .916$), and higher impedance, 10.8

kΩ, than the Teflon-coated electrode, 17.1 $\mu S \cdot s^{\alpha}$ (where α = .824) and 4.9 kΩ, respectively. Table 8.1 summarizes the film resistances and CPE's extrapolated from the equivalent circuits used to model the EIS spectra.

Although the pNBF6 film and the Teflon® film exhibit similar barrier properties, pNBF6 can be prepared at room temperature in ambient conditions with no specialized equipment beyond O_2-plasma treatment. Teflon coatings are generally prepared using chemical vapor deposition techniques under vacuum. pNBF6 can also be further modified via exposure to acetyl sulfate, resulting in a proton-conducting ionomer film that has utility if proton transport to the carbon paper is desired.[35]

Conclusion

Through surface-initiated ROMP of 5-perfluorohexylnorbornene, we have demonstrated a bottom-up approach to fabricate thin partially fluorinated polymer films on carbon paper electrodes. Exposing the carbon paper to O_2 plasma is a simple, fast method that produces hydroxyl groups on the surface. At least 45 s of plasma exposure is needed to saturate the carbon paper surface with oxidized species, and enables complete, coherent pNBF6 film growth. The pNBF6 films are hydrophobic and provide good impedance to the transfer of aqueous ions, exceeding the performance of commercially available Teflon-treated carbon paper. This protocol should be easily extendable to SI-ROMP of other norbornenyl derivatives as well.

References

1. Jennings, G. K.; Brantley, E. L., Physicochemical Properties of Surface-Initiated Polymer Films in the Modification and Processing of Materials. *Adv. Mater.* **2004,** 16, 1983-1994.

2. Jordi, M. A.; Seery, T. A. P., Quantitative determination of the chemical composition of silica-poly(norbornene) nanocomposites. *J. Am. Chem. Soc.* **2005,** 127, 4416-4422.

3. Yang, Q.; Wang, L.; Xiang, W. D.; Zhou, J. F.; Tan, Q. H., *Journal of Polymer Science Part a-Polymer Chemistry* **2007,** 45, 3451-3459.

4. Buchmeiser, M. R., Metathesis polymerizations to and from surfaces. In *Surface-Initiated Polymerization I*, Springer: Berlin, 2006; Vol. 197, pp 137-171.

5. Advincula, R., Polymer brushes by anionic and cationic surface-initiated polymerization (SIP). *Adv. Polym. Sci.* **2006,** 197, 107-136.

6. Guo, W.; Jennings, G. K., Directed Growth of Polymethylene Films on Atomically Modified Gold Surfaces. *Adv. Mater.* **2003,** 15, 588-591.

7. Rutenberg, I. M.; Scherman, O. A.; Grubbs, R. H.; Jiang, W.; Garfunkel, E.; Bao, Z., Synthesis of Polymer Dielectric Layers for Organic Thin Film Transistors via Surface-Initiated Ring-Opening Metathesis Polymerization. *Journal of the American Chemical Society* **2004,** 126, (13), 4062-4063.

8. Qin, S. H.; Oin, D. Q.; Ford, W. T.; Resasco, D. E.; Herrera, J. E., Polymer brushes on single-walled carbon nanotubes by atom transfer radical polymerization of n-butyl methacrylate. *Journal of the American Chemical Society* **2004,** 126, 170-176.

9. Watson, K. J.; Zhu, J.; Nguyen, S. T.; Mirkin, C. A., Hybrid nanoparticles with block copolymer shell structures. *Journal of the American Chemical Society* **1999,** 121, 462-463.

10. Jordan, R.; West, N.; Ulman, A.; Chou, Y. M.; Nuyken, O., Nanocomposites by surface-initiated living cationic polymerization of 2-oxazolines on functionalized gold nanoparticles. *Macromolecules* **2001,** 34, 1606-1611.

11. Balachandra, A. M.; Baker, G. L.; Bruening, M. L., Preparation of composite membranes by atom transfer radical polymerization initiated from a porous support. *Journal of Membrane Science* **2003,** 227, 1-14.

12. Jung, D. H.; Park, I. J.; Choi, Y. K.; Lee, S. B.; Park, H. S.; Ruhe, J., Perfluorinated polymer monolayers on porous silica for materials with super liquid repellent properties. *Langmuir* **2002,** 18, 6133-6139.

13. Huang, X.; Wirth, M. J., Surface-Initiated Radical Polymerization on Porous Silica. *Anal. Chem.* **1997,** 69, 4577-4580.

14. Buchmeiser, M. R.; Sinner, F.; Mupa, M.; Wurst, K., Ring-Opening Metathesis Polymerization for the Preparation of Surface-Grafted Polymer Supports. *Macromolecules* **2000,** 33, 32-39.

15. Heitzmann, M.; Basaez, L.; Brovelli, F.; Bucher, C.; Limosin, D.; Pereira, E.; Rivas, B. L.; Royal, G.; Saint-Aman, E.; Moutet, J. C., Voltammetric sensing of trace metals at a poly(pyrrole-malonic acid) film modified carbon electrode. *Electroanalysis* **2005,** 17, 1970-1976.

16. Emr, S. A.; Yacynych, A. M., Use of polymer-films in amperometric biosensors. *Electroanalysis* **1995,** 7, 913-923.

17. Moussy, F.; Jakeway, S.; Harrison, D. J.; Rajotte, R. V., In-vitro and in-vivo performance and lifetime of perfluorinated ionomer-coated glucose sensors afer high-temperature curing. *Analytical Chemistry* **1994,** 66, 3882-3888.

18. Faulkner, C. J.; Fischer, R. E.; Jennings, G. K., Surface-initiated polymerization of 5-(perfluoro-n-alkyl)norbornenes from gold substrates. *Macromolecules* **2009**.

19. Berron, B.; Faulkner, C. J.; Fischer, R. E.; Payne, P. A.; Jennings, G. K., Surface-Initiated Growth of Ionomer Films from Pt-Modified Gold Electrodes. *Langmuir* **2009,** 25, 12721-12728.

20. Tran, Y.; Auroy, P., Synthesis of poly(styrene sulfonate) brushes. *Journal of the American Chemical Society* **2001,** 123, 3644-3654.

21. Bevers, D.; Rogers, R.; vonBradke, M., Examination of the influence of PTFE coating on the properties of carbon paper in polymer electrolyte fuel cells. *Journal of Power Sources* **1996,** 63, 193-201.

22. Maheshwari, P. H.; Mathur, R. B., Improved performance of PEM fuel cell using carbon paper electrode prepared with CNT coated carbon fibers. *Electrochimica Acta* **2009,** 54, 7476-7482.

23. Chrisey, D. B.; Pique, A.; McGill, R. A.; Horwitz, J. S.; Ringeisen, B. R.; Bubb, D. M.; Wu, P. K., Laser Deposition of Polymer and Biomaterial Films. *Chemical Reviews* **2003,** 103, 553-576.

24. Berron, B. J.; Payne, P. A.; Jennings, G. K., Sulfonation of Surface-Initiated Polynorbornene Films. *Industrial & Engineering Chemistry Research* **2008,** 47, 7707-7714.

25. Barriere, F.; Downard, A. J., Covalent modification of graphitic carbon substrates by non-electrochemical methods. *J. Solid State Electrochem* **2008,** 12, 1231-1244.

26. Theodoridou, E.; Besenhard, J. O.; Fritz, H. P., Chemically modified carbon-fiber electrodes. 1. Bulk-functionalized carbon-fibers. *Journal of Electroanalytical Chemistry* **1981,** 122, 67-71.

27. Chou, A.; Bocking, T.; Singh, N. K.; Gooding, J. J., Demonstration of the importance of oxygenated species at the ends of carbon nanotubes for their favourable electrochemical properties. *Chemical Communications* **2005**, 842-844.

28. Yuan, L. Y.; Chen, C. S.; Shyu, S. S.; Lai, J. Y., Plasma surface-treatment on carbon-fiber. 1. Morphology and surface-analysis of plasma etched fibers. *Composites Science and Technology* **1992,** 45 1-7.

29. Zhu, Q. Y.; Sun, J. F.; He, C. J.; Zhang, J.; Wang, Q., Influence of plasma treatment on the electroless deposition of copper on carbon fibers. *Journal of Macromolecular Science Part a-Pure and Applied Chemistry* **2006,** 43, 1853-1865.

30. Dorrer, C.; Ruhe, J., Some thoughts on superhydrophobic wetting. *Soft Matter* **2009,** 5, 51-61.

31. Morra, A.; Occhiello, E.; Garbassi, F., Wettability and surface chemistry of irradiated PTFE. *Die Angewandte Makromolekulare Chemie* **1990,** 180, 191-198.

32. Weinstein, R. D.; Moriarty, J.; Cushnie, E.; Colorado, R.; Lee, T. R.; Patel, M.; Alesi, W. R.; Jennings, G. K., Structure, wettability, and electrochemical barrier properties of self-assembled monolayers prepared from partially fluorinated hexadecanethiols. *Journal of Physical Chemistry B* **2003,** 107, 11626-11632.

33. Barsoukov, E.; Macdonald, J. R., *Impedance spectroscopy: theory, experiment, and applications*. Second ed.; Wiley-Interscience: Hoboken, N.J., 2005.

34. Smith, M. B.; Tong, J. H.; Genzer, J.; Fischer, D.; Kilpatrick, P. K., Effects of synthetic amphiphilic alpha-helical peptides on the electrochemical and structural properties of supported hybrid bilayers on gold. *Langmuir* **2006,** 22, 1919-1927.

35. Berron, B.; Faulkner, C. J.; Fischer, R. E.; Payne, P. A.; Jennings, G. K., Surface-Initiated Growth of Ionomer Films from Pt-Modified Gold Electrodes. *Langmuir* **2009**, 25, 12721–12728.

CHAPTER IX

SURFACE-INITIATED RING-OPENING METATHESIS POLYMERIZATION OF POLY(5-PERFLUOROHEXYL)NORBORNENE WITHIN NANOPOROUS GOLD LEAF ELECTRODES

Introduction

The current measured by an electrode scales with its electrochemically active area, thus the fabrication and modification of highly porous conductive substrates is an active area of research. These porous electrodes can be fabricated using casting and etching methods involving colloidal dispersions[1] or block copolymers,[2, 3] the anodization of oxides, such as alumina,[4] and electrochemical acid treatments of silicon.[5] Porous gold electrodes are advantageous for their chemical stability, wide active electrochemical window, and ease of surface modification with thiols and disulfides.[6, 7] However, there are few simple methods available to synthesize nanoporous metallic structures. An exception, is the dealloying of gold/silver leaf alloy reported by Erlebacher et al.[8] to create a thin, ~50-100 nm thick, mesoporous gold substrate. The dealloying process they describe yields highly porous gold substrates, with features on the nanoscale, without the use of prefabricated scaffolds. Their group recently used these porous gold substrates in the assembly of a proton exchange membrane (PEM) fuel cell using Pt-plated nanoporous gold leaf (NPGL) as electrodes and Nafion 113.5 as the PEM.[9] Our group[10] has used an adaptation of Erlebacher's procedure to attach a photo-active protein to nanoporous gold electrodes for the enhancement of biomimetic solar energy conversion. In order to stabilize the thin NPGL, we supported the NPGL on glass and Au-coated silicon

substrates using thiol-terminated silanes and dithiols, respectively, to prepare an adhesive interlayer.

Highly porous architectures, like NPGL, functionalized with thin films have many applications in separations,[11] protective coatings,[12, 13] and catalysis.[14] Thin films range in thicknesses from 1 nm,[15] as in the case of monolayer films, or as thick as a few microns using polymeric films. These films can be discretionary based on molecule size, charge, or chemical affinity, and thus facilitate or block the transport of desired species. Polymer films are prepared using either physical adsorption or chemical attachment. Physical applications of polymer films such as spin-coating[16] and solution-casting[17] provide coherent films of tunable thickness on flat substrates. However, these methods yield incomplete and non-conformal coatings on complex three dimensional substrates such as membranes and porous structures due to the topical application of these techniques. Non-uniformity of the polymer films within the porous support can underutilize an electrode's surface area causing poor transport, barriers properties, or catalysis. To overcome these limitations, bottom-up approaches can be used to coat and functionalize porous architectures. In contrast to spin-coating and drop-casting methods, surface-initiated polymerizations (SIPs) enable the growth of polymer films on flat or irregular geometries while providing a direct chemical attachment to the substrate.[18] In SIP, the monomer reacts with a surface-tethered initiator or polymerization catalyst, resulting in the growth of a polymer chain from the surface. Thus, the surface-initiated polymer film can be tailored to provide desired chemical functionality. Lopez et al. utilized atom transfer radical polymerization (ATRP) of N-isopropyl acrylamide throughout mesoporous silica particles to control the transport of molecular species.

Whereas, Bruening, Baker, and co-workers grew poly(hydroxyethylmethacrylate) (PHEMA) films from porous alumina supports to enhance the performance of CO_2/CH_4 separations.

In this chapter, we describe the coating of NPGL electrodes utilizing surface-initiated ring-opening metathesis polymerization (SI-ROMP) of 5-(perfluorohexyl)norbornene (NBF6). We have previously demonstrated surface-initiated growth of poly(5-(perfluoro-n-alkyl)norbornenes (pNBFn) films on planar gold electrodes.[19] These films exhibit rapid growth kinetics with low critical surface energies while providing an effective barrier to the diffusion of aqueous ions.[19] pNBFn films can be converted to ionomer films through exposure to 0.1 M dichloromethane solution of acetyl sulfate, which reacts with the olefin residing in the polymer backbone to yield a sulonate group.[20, 21]

One of the challenges of investigating the properties of functionalized nanoporous architectures, such as NPGL, is that the inner dimensions of the structure are not readily accessible. Thus, determining the extent and coverage of polymerization throughout highly porous structures is usually reliant upon destructive techniques. However, electrochemical probing of the film provides a non-destructive method to investigate the properties of these systems.

Here, we characterize the pNBF6-coated NPGL electrodes using electrochemical impedance spectroscopy (EIS) in conjunction with scanning electron microscopy (SEM) to determine the extent and coverage of the polymer film. Our approach demonstrates the growth of coherent polymer coatings throughout NPGL electrodes and their subsequent characterization using non-destructive techniques.

Experimental Procedures

Preparation of Nanoporouos Gold Leaf

The nanoporous gold leaf electrodes were fabricated using a technique we previously reported[10] that was adapted from a method developed by Ding et. al.[8] The gold/silver leaf was cut into portions slightly larger than the final desired sample size to allow the NPGL to completely cover the substrate surface. The leaf was then gently placed onto a glass microscope slide, and the slide was slowly dipped into a beaker of concentrated nitric acid causing the leaf to float at the air-acid interface. As the leaf floated freely on the surface of the acid, the glass slide was removed to allow the dealloying to proceed for the desired time. The leaf was then removed from the acid with a glass slide by positioning it beneath the NPGL, and then gently withdrawing it. As the slide was removed, the free-floating leaf adhered smoothly to the surface, and it was then transferred to a beaker of deionized water for rinsing. The leaf was removed from the air-water interface with a pre-cut portion of a glass slide that was pre-modified with 3-mercaptopropyl trimethoxysilane. The free thiols on the terminus of the silane bind the NPGL to the surface, fastening it firmly to the planar glass substrate, shown in Figure 1a. The glass slides were typically cut to 1 cm x 4 cm pieces.

pNBF6 Polymer Preparation

pNBF6 films were grown from the NPGL substrates using the scheme shown in Figure 6.3. NPGL substrates supported on glass slides were placed in a 1.0 mM ethanolic solution of 4-mercapto-1-butanol for at least 1 h to yield a hydroxyl-terminated self-

assembled monolayer (SAM). The films were rinsed in ethanol and dried in a stream of nitrogen. Exposure of the SAM to a 5 mM solution of trans-3,6-endo-methylene-1,2,3,6-tetrahydrophthaloyl chloride in dichloromethane for 30 min yielded the acylation product of a surface-tethered norbornenyl group.[22] The samples were rinsed in ethanol and dried in a stream of N_2. The norbornenyl decorated substrates were exposed to a 5 mM solution of Grubbs (II) catalyst in dichloromethane for 90 min. The monolayers were rinsed with dichloromethane and immediately placed in a monomer solution containing 0.05 M NBF6 in dichloromethane for 10 min to grow pNBFn films.

Electrochemical Impedance Spectroscopy (EIS)

Since the surface area of a NPGL electrode is dependent on the dealloying time during the etching process and decreases as etching time increases, our reported values are on a geometric 1 cm^2 basis, not the electrochemically active surface area of the NPGL electrode. Thus, the reported impedances for the NPGL electrodes are deflated since the amount of current measured from an electrode surface scales with its surface area.

Results and Discussion

Effect of NBF6 Concenctration

Polymer films were grown from NPGL surfaces by utilizing SI-ROMP as depicted in Figure 6.3. A $HO(CH_2)_4S$/Au SAM was treated with trans-3,6-endo-methylene-1,2,3,6-tetrahydrophthaloyl chloride, which is a norbornene with pendant acid chlorides in the 4 and 5 positions, to produce an ester-linked norbornene group on the

surface. The resulting surface was made catalytically active for ROMP by exposure to Grubbs 2nd generation catalyst. Subsequent exposure to a solution of NBF6 in dichloromethane (DCM) for 90 min resulted in the growth of partially fluorinated polymer films from the NPGL surface. The average pore size of NPGL electrodes dealloyed for 4 h is on the order of 50 nm, Figure 9.2(a).

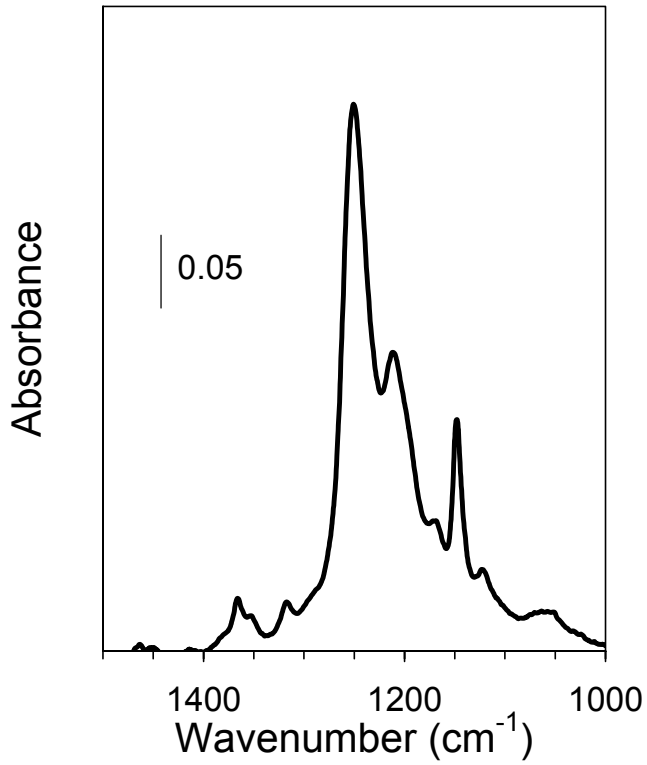

Figure 9.1. Reflectance absorption infrared spectra of pNBF6 grown from a NPGL electrode. -CF_2 groups primarily exhibit two modes of stretching: $\nu_{ax}(CF_2)$ from 1300-1400 cm^{-1} and $\nu_{pd}(CF_2)$ from 1100-1300 cm^{-1}.

We used RAIRS to confirm the growth and structure of the pNBF6 films. Figure 9.1 displays the fluorocarbon region of the RAIR spectrum of a pNBF6 film grown from a NPGL electrode. As can be seen, the pNBF6 film absorbs strongly from 1100-1300

cm^{-1} and weakly from 1300-1400 cm^{-1}, which is attributed to CF_2 stretching perpendicular and parallel, respectively, to the helical axis of the fluorocarbon chain.[17-19]

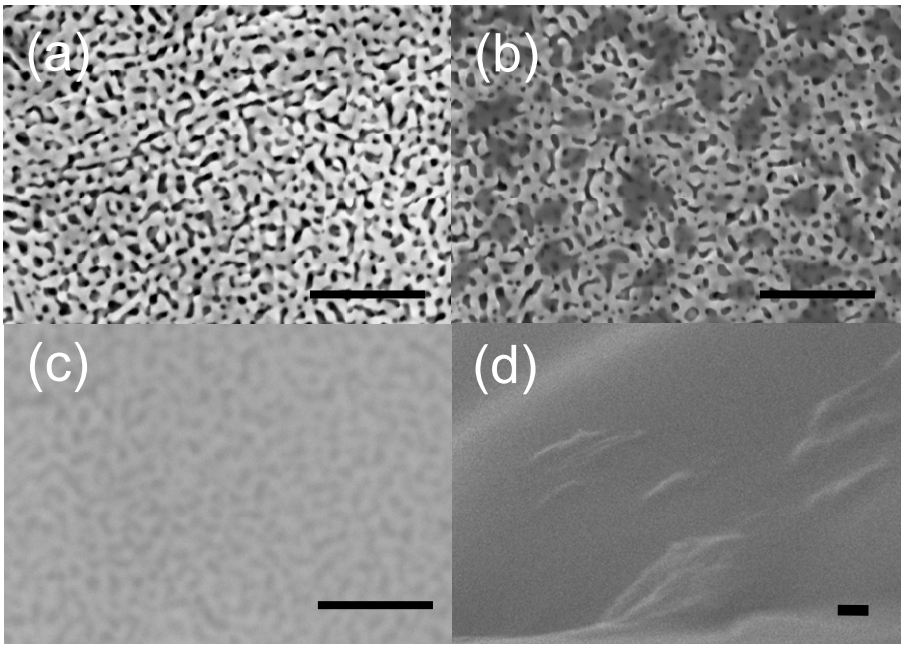

Figure 9.2. Scanning electron micrographs of NPGL electrodes modified with norbornenyl initiator (a) and pNBF6 film grown in 0.025 M (b), 0.05 M (c), and 0.1 M (d) NBF6 solution. The pNBF6 films were grown for 90 min in DCM.

As expected, the pNBF6 film greatly enhances the hydrophobicity and the oleophobicity of the NPGL electrodes. Table 9.1 summarizes the advancing water and hexadecane contact angles atop the pNBF6-coated NPGL electrodes after each stage of the polymerization process shown in Figure 6.3. The average advancing contact angle for water and hexadecane is ~120° and ~ 66°, respectively, which is consistent with dense fluorocarbon films on a porous support. There was no observable difference in the wettability of the modified NPGL electrodes except for electrodes coated with pNBF6 films grown in 5 mM NBF6. These electrodes showed the greatest hysteresis, 76° ± 2°

vs. 30° ± 3° for all other pNBF6 films, between advancing and receding water contact angles, indicating a poorly formed pNBF6 film.

Table 9.1. Wetting properties of pNBF6 films grown on NPGL electrodes.

	Advancing Contact Angle (°)		Receding Contact Angle (°)	
Film	θ_{H2O}	θ_{HD}	θ_{H2O}	θ_{HD}
Initiator	61 ± 4	—	15 ± 1	—
pNBF6	120 ± 3	66 ± 1	90 ± 2	32 ± 1

Previously, we have shown the ability to control pNBFn film growth on planar gold electrodes by varying the concentration of the monomer solution.[19] We demonstrated that we could grow polymer films ranging in thicknesses from ~50 nm to ~ 1 μm using NBFn concentrations ranging from 50 mM – 1 M, respectively. Extending this trend to pNBF6 growth on NPGL electrodes, we should be able to induce sparse, coherent, and superfluous polymer growth on the NPGL support by changing the concentration of NBF6 during polymerization. To investigate the extent of polymerization throughout the NPGL electrode, including the inner dimensions, without destroying the NPGL electrode, we used electrochemical impedance spectroscopy (EIS) to probe the films. EIS is a non-destructive analytical electrochemical technique that probes electrode interfaces with redox species to determine the barrier properties of a surface film. Previously, we investigated the barrier properties of SAMs formed from the adsorption of n-alkanethiols onto a NPGL electrode. SAMs are convenient due to their ease of formation and their formation of dense monolayer films. The n-alkanthiolate SAMs effectively provided a barrier against aqueous ions displaying a trend of decreasing film capacitance with increasing chain length, which is consistent with an

effective increase in film thickness. EIS spectra can be fit with appropriate equivalent circuit models to extract effective film resistances and capacitances. A standard Randle's equivalent circuit was used to model the n-alkanthiolate EIS spectra mentioned above, in which charge transfer through the SAM and electrolyte solution can be modeled using a parallel capacitor (C_i) and resistor (R_i) in series with a solution resistance (R_s). We used a two-time constant equivalent circuit to model the EIS spectra of pNBFn films on planar gold electrodes to account for the polymer film and the polymer/metal interface. For pNBF6 films grown from NPGL electrodes, three distinct domains are possible: 1) the initiator tethered to the NPGL surface, 2) the pNBF6 film within the pores, and 3) the pNBF6 film atop the NPGL electrode.

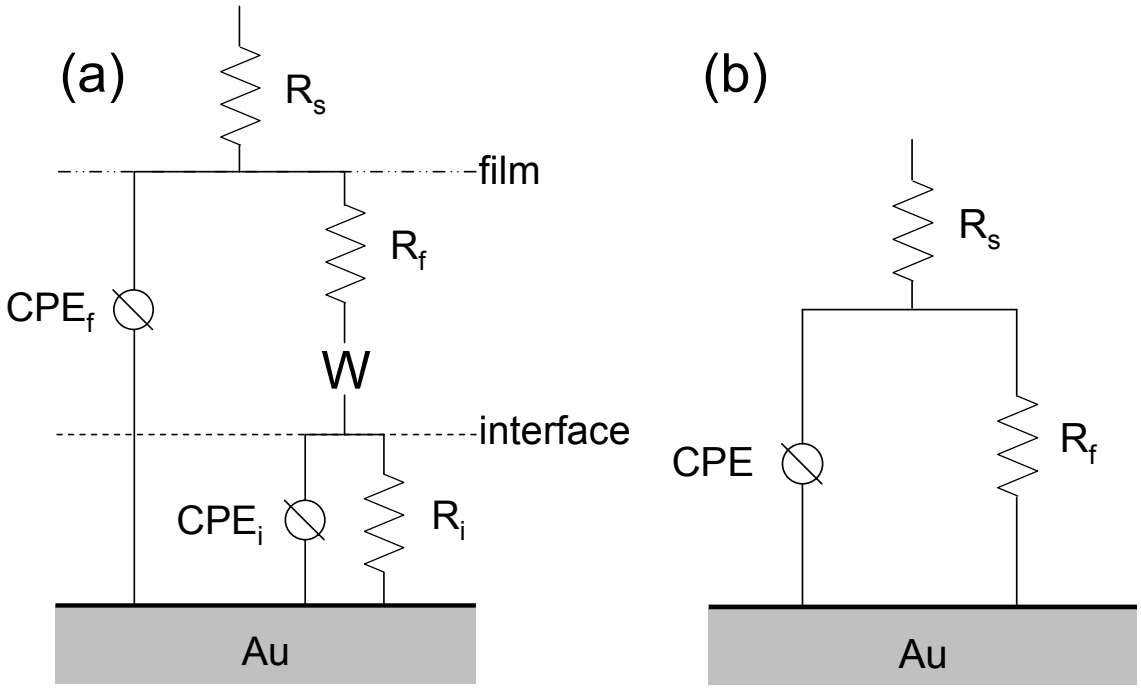

Figure 9.3. Equivalent circuits used to model impedance spectra for polymer films on NGPL: (a) a two time constant model for both the polymer film and organic-metal interface and (b) a modified Randle's circuit.

Thus, a three-time constant equivalent circuit is appropriate to model the EIS spectra of pNBF6 films on NPGL electrodes. However, this model can be simplified to a two-time constant and even a Randle's equivalent circuit under certain conditions. If no superfluous overgrowth of polymer exists on top of the NPGL electrode or if the film impedance does not dominate the interfacial impedance, then the EIS spectra can be modeled using the circuit shown in Figure 9.3(a). In some cases, the film impedance dominates the spectrum so that the time constant for interfacial impedance and bulk (film atop the electrode) pNBF6 is insignificant, thus reducing the model to a Randle's circuit, shown in Figure 9.3(b). To aid in the interpretation of our EIS spectra, we collected scanning electron micrographs as well, displayed in Figure 9.2.

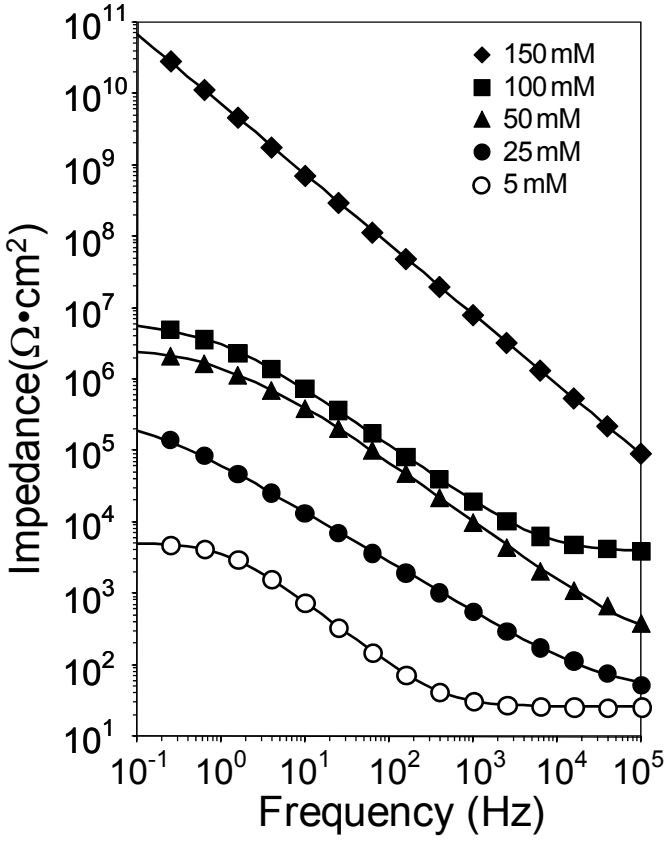

Figure 9.4. Electrochemical impedance spectra obtained in 1 mM $K_3Fe(CN)_6$ and 1 mM $K_4Fe(CN)_6$ in 0.1 M Na_2SO_4(aq) for the pNBF6 films on NPGL, dealloyed for 4 h, prepared by exposure of Grubbs II-

modified surfaces to 5 mM, 25 mM, 50 mM, 100 mM, or 150 mM NBF6 in DCM for 90 min. Solid curves represent fits of the data using appropriate equivalent circuit models.

Figure 9.4 displays EIS spectra of pNFB6 films grown from Grubbs (II) modified NPGL in 5 mM, 25 mM, 50 mM, 100 mM, or 150 mM NBF6 for 90 min on NPGL electrodes. An aqueous solution of 1 mM $K_4Fe(CN)_6 \bullet 3H_2O$, 1 mM $K_3Fe(CN)_6$, and 0.1 M Na_2SO_4 was used to provide redox probes to interrogate the surface. These spectra have been fit with the equivalent circuit models shown in Figure 9.3, and the equivalent film resistances and capacitances are summarized in Table 9.2. As shown in Figure 9.4, the pNBF6 film resistances increase and the film capacitances decrease for increasing monomer concentrations during polymerization. This trend is consistent with polymerizations on 2-D supports in that higher concentrations produce thicker films, as film capacitance is inversely proportional to film thickness.

Table 9.2. Impedance properties of pNB6 films grown from 0.005 M, 0.025 M, 0.05 M, 0.1 M, or 0.15 M monomer solutions for 90 min on NPGL dealloyed for 4 h.

Concentration	log (R_f ($\Omega \cdot cm^2$))	CPE_f ($\mu S * s^{\alpha}$)
5 mM	3.7	32.6
25 mM	5.5	3.94
50 mM	6.4	0.07
100 mM	6.8	0.045
150 mM	11.7	2.25×10^{-5}

pNBF6 prepared in 5 mM monomer solution for 90 min are so thin that its spectrum is comparable to that of the polymerization precursor, shown in Figure 9.5. This indicates that little to no polymer growth occurred in 5 mM NBF6 solution. However, pNBF6 films grown in 25 mM monomer solution provide barrier properties comparable to that derived from a dodecanethiol monolayer,[10] suggesting that an appreciable amount of

polymer growth occurred throughout the NPGL electrode providing an effective barrier to ion transport. The scanning electron micrograph shown in Figure 9.2(b) confirms the pNBF6 film growth in 25 mM monomer solution as the pore sizes are diminished, and also reveals the formation of island polymer domains atop the NPGL electrode. The pores of the NPGL, although slightly smaller due to the pNBF6 film, can still be distinguished clearly. The EIS spectrum of pNBF6 grown in 50 mM NBF6, Figure 9.4, is consistent with a conformal polymer coating. The spectrum can be modeled with a Randle's circuit indicating a solution resistance at high frequencies, film resistance at low frequencies, and film capacitance at moderate frequencies. Randle's equivalent circuits have been used to model complete coatings atop 2-D electrodes. Figure 9.2(c) displays an SEM image of a coherent, complete pNBF6 coating, prepared in 50 mM NBF6, of the NPGL. The pore openings in the NPGL are muted, but are still visible. The EIS spectrum of pNBF6 grown in 100 mM monomer solution, Figure 9.4, is similar to the film grown in 50 mM NBF6; however, a higher impedance at high frequencies, lower capacitance, and higher film resistance are noticeable. The impedance of the pNBF6 film at high frequencies can be attributed to the increased polymer growth on top of the NPGL electrode that further separates the NPGL electrode from the redox probes in the aqueous solution. The added polymer dielectric layer increases the resistance in the circuit and is accounted for as a film resistance in the equivalent circuit. Confirming the additional growth of pNBF6 atop the NPGL electrode, the SEM image shown in Figure 9.2(d) displays an overgrown polymer film that completely covers the porous network of the NPGL. The inner dimensions of the NPGL electrode are still accessible by the redox probes interacting with the NPGL surface, represented as the film resistance in the EIS

spectrum (Figure 9.4, 100 mM). The pNBF6 film grown in 150 mM monomer solution yielded the most unique EIS spectrum. The data can be modeled as a pure capacitor indicating that no redox probes were able to interact with the surface during the time period of the experiment. This suggests superfluous film growth atop the NPGL electrode such that no redox probes were able to penetrate the pNBF6 film. Comparing this spectrum to that of a ~600 nm pNBF6 film grown on a planar gold electrode we previously reported[19], may indicate that the pNBF6 film plugged the pores within the NPGL entrapping air beneath the polymer film. The pNBF6 film on planar gold exhibited Randle's circuit behavior[23] in which the redox couples interacted with the gold substrate at lower frequencies. The barrier properties observed of pNBF6 films on planar gold electrodes coupled with the pure capacitive behavior of pNBF6 grown from NPGL suggests that the pNBF6 film grown on NPGL in 150 mM NBF6 is either ~14 mm thick (estimated based on the inverse relationship to film thickness and film capacitance in EIS), which is inconsistent with pNBF6 polymerization kinetics and visual observations, or contains a layer, such as trapped air, that inhibits charge transfer. Thus, by controlling the concentration of NBF6 during polymerization we are able to tune the polymer film growth throughout the NPGL electrode, ranging from films that provide comparable impedance as SAM films to films that behave as pure capacitors.

Effect of NPGL Pore Size

One of the challenges in growing conformal polymer coatings within small pores is that diffusion limitations can cause excessive growth near the top of the pores that tapers to negligible film growth as pore depth increases. Thus, pores need to be large enough to

enable coherent polymer film growth throughout the structure. We fabricated nanoporous gold leaf electrodes using a similar method previously reported by Erlebacher et al.[8] Concentrated nitric acid was used to selectively leach the silver from a gold/silver leaf; thereby, creating a highly porous gold electrode. The pore size within the NPGL is tunable by controlling the leaf's exposure to nitric acid, with longer exposure to nitric acid longer increasing the average pore size while reducing the surface area of the NPGL.[8, 10] We[10] and Erlebacher et al.[8] previously reported the correlation between the total surface area of the NPGL and nitric acid exposure time. The surface area of a NPGL electrode prepared via 30 min of acid exposure is ~15 fold greater than a planar gold electrode, whereas a NPGL electrode prepared via 24 h of acid exposure is only ~4 fold greater.[10]

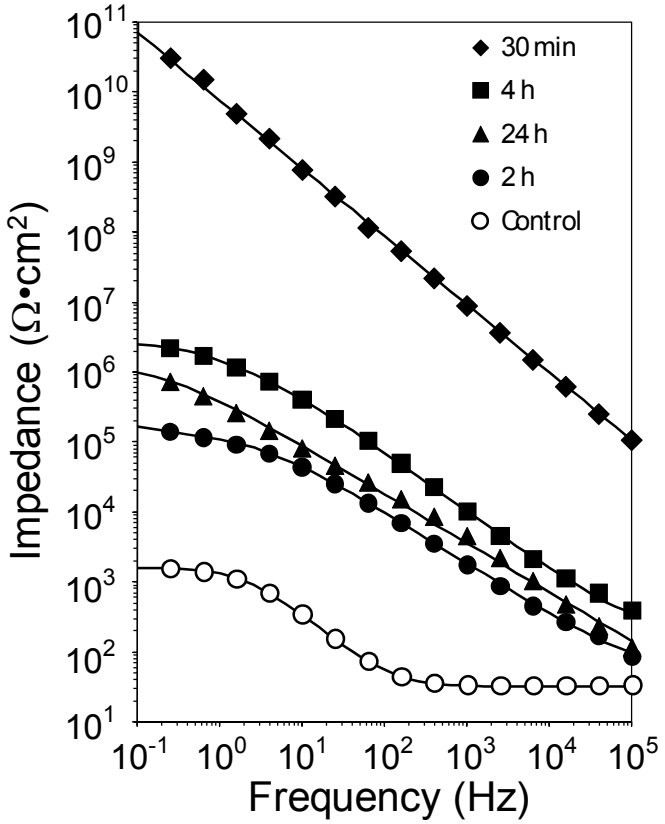

Figure 9.5. Electrochemical impedance spectra obtained in 1 mM $K_3Fe(CN)_6$ and 1 mM $K_4Fe(CN)_6$ in 0.1 M Na_2SO_4(aq) for the pNBF6 films on NPGL dealloyed for the times indicated. The pNBF6 films were prepared by exposure of Grubbs II-modified surfaces to 0.05 M NBF6 in DCM for 90 min. The control spectrum indicates a norbornenyl decorated NPGL electrode. Solid curves represent fits of the data using appropriate equivalent circuit models.

We investigated the pore size in which complete, coherent pNBF6 films within the NPGL can be grown using a span of dealloying times from 30 min – 24 h. Figure 9.5 displays the EIS data of pNBF6 films grown on NPGL electrodes exposed to nitric acid for 30 min, 2 h, 4 h, and 24 h. These spectra have been fit with the equivalent circuit model shown in Figure 9.3, and the equivalent film resistances and capacitances are summarized in Table 9.3. The spectrum for each film is consistent with predominately capacitive behavior where the conductive electrolyte is separated from the electrode by the polymer dielectric, which is modeled as a constant phase element (CPE_f), to allow for film inhomogeneity.[24, 25] All pNBF6 films performed as better protective barriers against

aqueous ions than a monolayer of the polymer initiator, labeled as the control in Figure 6. Interestingly, the pNBF6 film grown on the NPGL with the highest surface area, 30 min acid treatment, exhibits only capacitive behavior, similar to that of pNBF6-coated NPGL grown in 150 mM monomer concentration, indicating that no redox probes were able to reach the NPGL surface within the frequencies measured. A trend is apparent, shown in Figure 9.5, for the remaining dealloying times in which the impedance properties decrease as dealloying times increase. The impedance values shown in Figure 9.5 are based on per geometric area and do not account for active surface area of the electrode. Thus, the higher surface area electrodes, those dealloyed for shorter times, have deflated impedance values. Taking this into account, the impedance values for the pNBF6 film on NPGL that has been dealloyed for two hours is consistent with the trend of lower impedance with increasing dealloying times.

Table 9.3. Impedance properties of pNB6 films grown from 0.05 M monomer solutions for 90 min on NPGL dealloyed for 30 min, 2 h, 4 h, or 24 h.

Time (h)	$\log(R_f\,(\Omega \cdot cm^2))$	CPE_f ($nS*s^{\alpha}$)
0.5	11.8	0.0002
2	5.1	863
4	6.4	69.5
24	6.1	616

Conclusion

Through surface-initiated ROMP of 5-perfluorohexylnorbornene, we have demonstrated a simple bottom-up approach to fabricating thin fluorinated polymer films on nanoporous gold leaf electrodes. The pNBF6 films are hydrophobic and provide good impedance to the transfer of aqueous ions. EIS in conjunction with SEM was used to effectively characterize the extent of polymerization throughout the NPGL electrodes.

We are able to grow incomplete, coherent, and superfluous pNBF6 films on the NPGL electrodes by controlling the monomer concentration during film growth. Polymerizations in NBF6 concentrations greater than 150 mM cap the electrode pores, entrapping air beneath the polymer film. The pore size of the NPGL electrode also impacts the growth of pNBF6 films, such that, if the pores are too small, the pNBF film rapidly caps and plugs the pores of the electrode, entrapping a layer of air beneath the polymer.

References

1. Xia, Y. N.; Gates, B.; Yin, Y. D.; Lu, Y., Monodispersed colloidal spheres: Old materials with new applications. *Advanced Materials* **2000,** 12, 693-713.

2. Chan, V. Z. H.; Hoffman, J.; Lee, V. Y.; Iatrou, H.; Avgeropoulos, A.; Hadjichristidis, N.; Miller, R. D.; Thomas, E. L., Ordered bicontinuous nanoporous and nanorelief ceramic films from self assembling polymer precursors. *Science* **1999,** 286, 1716-1719.

3. Templin, M.; Franck, A.; DuChesne, A.; Leist, H.; Zhang, Y. M.; Ulrich, R.; Schadler, V.; Wiesner, U., Organically modified aluminosilicate mesostructures from block copolymer phases. *Science* **1997,** 278, (5344), 1795-1798.

4. Foss, C. A.; Hornyak, G. L.; Stockert, J. A.; Martin, C. R., Template-synthesized nanoscopoic gold particles: optical spectra and the effects of particle size and shape. *Journal of Physical Chemistry* **1994,** 98, 2963-2971.

5. Levyclement, C.; Lagoubi, A.; Ballutaud, D.; Ozanam, F.; Chazalviel, J. N.; Neumannspallart, M. In *Porous-n-silicon produced by photoelectrochemical etching*, 1993; Elsevier Science Bv: 1993; pp 408-414.

6. Love, J. C.; Estroff, L. A.; Kriebel, J. K.; Nuzzo, R. G.; Whitesides, G. M., Self-Assembled Monolayers of Thiolates on Metals as a Form of Nanotechnology. *Chem. Rev.* **2005,** 105, 1103-1169.

7. Nuzzo, R. G.; Fusco, F. A.; Allara, D. L., Spontaneously Organized Molecular Assemblies. 3. Preparation and Properties of Solution Adsorbed Monolayers of Organic Disulfides on Gold Surfaces. *J. Am. Chem. Soc.* **1987,** 109, 2358-2367.

8. Ding, Y.; Kim, Y. J.; Erlebacher, J., Nanoporous gold leaf: "Ancient technology"/advanced material. *Advanced Materials* **2004,** 16, 1897-1900.

9. Zeis, R.; Mathur, A.; Fritz, G.; Lee, J.; Erlebacher, J., Platinum-plated nanoporous gold: An efficient, low Pt loading electrocatalyst for PEM fuel cells. *Journal of Power Sources* **2007,** 165, 65-72.

10. Ciesielski, P. N.; Scott, A. M.; Faulkner, C. J.; Berron, B. J.; Cliffel, D. E.; Jennings, G. K., Functionalized Nanoporous Gold Leaf Electrode Films for the Immobilization of Photosystem I. *Acs Nano* **2008,** 2, 2465-2472.

11. Balachandra, A. M.; Baker, G. L.; Bruening, M. L., Preparation of composite membranes by atom transfer radical polymerization initiated from a porous support. *Journal of Membrane Science* **2003,** 227, 1-14.

12. Brantley, E. L.; Holmes, T. C.; Jennings, G. K., Modification of Poly(hydroxyethyl methacrylate) Films with Hydrocarbon Side Chains. *J. Phys. Chem. B* **2004,** 108, 16077-16084.

13. Deflorian, F.; Fedrizzi, L.; Bonora, P. L., Impedance study of teh corrosion protection properties of fluoropolymer coatings. *Progress in Organic Coatings* **1993,** 23, 73-88.

14. Souzy, R.; Ameduri, B., Functional fluoropolymers for fuel cell membranes. *Progress in Polymer Science* **2005,** 30, 644-687.

15. Jirage, K. B.; Hulteen, J. C.; Martin, C. R., Effect of thiol chemisorption on the transport properties of gold nanotubule membranes. *Analytical Chemistry* **1999,** 71, 4913-4918.

16. Genzer, J.; Sivaniah, E.; Kramer, E. J.; Wang, J. G.; Xiang, M. L.; Char, K.; Ober, C. K.; Bubeck, R. A.; Fischer, D. A.; Graupe, M.; Colorado, R.; Shmakova, O. E.; Lee, T. R., Molecular orientation of single and two-armed monodendron semifluorinated chains on "soft" and "hard" surfaces studied using NEXAFS. *Macromolecules* **2000,** 33, 6068-6077.

17. Sivakumar, C.; Wen, T. C.; Gopalan, A.; Teng, H., Electroactive conducting blends of poly(o-toluidine) and poly(vinylidene fluoride) and characterisation. *Synthetic Metals* **2003,** 132, 219-226.

18. Jennings, G. K.; Brantley, E. L., Physicochemical Properties of Surface-Initiated Polymer Films in the Modification and Processing of Materials. *Adv. Mater.* **2004,** 16, 1983-1994.

19. Faulkner, C. J.; Fischer, R. E.; Jennings, G. K., Surface-initiated polymerization of 5-(perfluoro-n-alkyl)norbornenes from gold substrates. *Macromolecules* **2009**, *in press.*

20. Berron, B.; Faulkner, C. J.; Fischer, R. E.; Payne, P. A.; Jennings, G. K., Surface-Initiated Growth of Ionomer Films from Pt-Modified Gold Electrodes. *Langmuir* **2009,** 25, 12721-12728.

21. Tran, Y.; Auroy, P., Synthesis of poly(styrene sulfonate) brushes. *Journal of the American Chemical Society* **2001,** 123, 3644-3654.

22. Berron, B. J.; Payne, P. A.; Jennings, G. K., Sulfonation of Surface-Initiated Polynorbornene Films. *Industrial & Engineering Chemistry Research* **2008,** 47, 7707-7714.

23. Jennings, G. K.; Laibinis, P. E., Self-Assembled n-Alkanethiolate Monolayers on Underpotentially Deposited Adlayers of Silver and Copper on Gold. *J. Am. Chem. Soc.* **1997,** 119, 5208-5214.

24. Barsoukov, E.; Macdonald, J. R., *Impedance spectroscopy: theory, experiment, and applications*. Second ed.; Wiley-Interscience: Hoboken, N.J., 2005.

25. Smith, M. B.; Tong, J. H.; Genzer, J.; Fischer, D.; Kilpatrick, P. K., Effects of synthetic amphiphilic alpha-helical peptides on the electrochemical and structural properties of supported hybrid bilayers on gold. *Langmuir* **2006,** 22, 1919-1927.

CHAPTER X

CONCLUSIONS AND FUTURE WORK

Conclusions

In this body of work, we have shown proof-of-concept designs for the development of dense, protein films on electrode surfaces for use in biomimetic solar energy conversion and the bottom-up growth of ionomer films on both 2-D and 3-D electrode architectures for use in proton exchange membrane fuel cells (PEM-FC).

In Chapter IV, we demonstrated that a critically dense monolayer of spinach-derived PSI must be formed on an electrode surface to achieve optimal photocurrents, and we introduced a new method for preparing these dense PSI monolayers that reduces the time required for assembly by ~80 fold in comparison to that for adsorption from solution**.** This method consisted of applying a vacuum above the aqueous PSI solution during assembly to concentrate PSI and precipitate it into a thick layer onto the surface of various self-assembled monolayers or directly onto the electrode surface. Rinsing with water yielded a dense monolayer of PSI that draws ~100 nA/cm^2 of light-induced current from the gold electrode in the presence of appropriate electron transfer mediators.

We extended the method described in Chapter IV to the preparation of multilayer Photosystem I (PSI) films on gold electrodes in Chapter V. Upon concentrating PSI into a thick layer onto the gold electrode surface, we exposed the film to an ethanol bath. The ethanol bath selectively dissolved the surfactant stabilizing the PSI in aqueous solution, leaving a multilayered PSI film on the electrode surface. Using a custom three-electrode

electrochemical cell, the photocurrent response of PSI-modified electrodes was measured upon exposure to light. The multilayered PSI film drew up to ~20 fold more photocurrent than a monolayer PSI film from a gold electrode when coupled with appropriate electron transfer mediators.

In Chapter VI, we introduced a new class of polymers that are able to be grown from gold electrodes using a bottom-up approach which allows for excellent control over film properties. We described the synthesis of 5-(perfluoro-n-alkyl)norbornenes and utilized surface-initiated ring-opening metathesis polymerization (SI-ROMP) of NBFn to grow partially fluorinated polymer films of tunable thicknesses ranging from tens of nanometers to microns on gold substrates. The perfluoroalkyl chains range in length (n) from 4 – 10 carbons, representing 67 – 83% of the molecular weight of the repeat unit. The growth rate of the film depends on the perfluoroalkyl chain length, with longer chains enabling faster surface-initiated growth and greater ultimate thicknesses. These films exhibited hydrophobic and oleophobic surface properties and proved effective barriers to the diffusion of aqueous ions. The critical surface tensions of the films exhibit a minimum for a fluorocarbon chain of 8 (pNBF8) and range from 9 to 19 mN/m. The morphologies of the pNBFn films consisted of densely packed 20-30 nm clusters that differ in the concentration of fluorocarbon chains in the outer few nm of the film.

Sulfonating the pNBFn films and integrating them with a Pt-catalyst enabled the investigation of current production via oxygen reduction reaction. In Chapter VII, we demonstrated proof-of-concept principles for the SI-ROMP of norbornene (NB), 5-butylnorornene (NBH4), and NBF4 from Pt-modified gold substrates and the subsequent sulfonation of olefins along the polymer back-bones to produce ultrathin sulfonated

polymer films. Prior to sulfonation, the films were hydrophobic and exhibited large barriers against ion transport, but sulfonation dramatically reduced the resistance of the films by providing pathways for proton diffusion. Sulfonated films derived from NBF4 and NBH4 yielded more anodic potentials for oxygen reduction than those derived from NB or unfunctionalized electrodes. These improvements are consistent with hydrophobic structuring by the fluorocarbon or hydrocarbon side groups to minimize interfacial flooding and generate pathways for enhanced O_2 permeation near the interface. Importantly, we demonstrated that the sulfonated polymer chains remained anchored to the surface during voltammetry for oxygen reduction whereas short-chain thiolates that do not tether polymer were removed from the substrate. This approach, which we extend to unmodified gold electrodes at neutral pH, presents a method of cleaning the ionomer/electrode interface to remove molecular components that hamper the performance of the electrode.

We extended these polymer films from planar electrodes 3-D, porous electrodes. In Chapters VIII and IX, we described the SI-ROMP of NBF6 on two porous supports: carbon paper and nanoporous gold leaf, respectively. We grew pNBF6 from carbon paper that was pre-treated with O_2 plasma. For our reaction scheme, the growth of the pNBF6 films is dependent on the concentration of hydroxyl groups on the carbon paper substrate. X-ray photoelectron spectroscopy and scanning electron microscopy were used to determine the required time for O_2 plasma exposure to saturate the surface with hydroxyl-termini. Complete, conformal pNBF6 films were grown on carbon paper electrodes exposed to O_2 plasma for at least 45 s. These films exhibit hydrophobic and oleophobic surface properties and provided similar barrier properties to that of Teflon-treated carbon

paper. However, pNBF6 can be prepared at room temperature in ambient conditions with no specialized equipment beyond O_2-plasma treatment. Teflon coatings are generally prepared using chemical vapor deposition techniques under vacuum. pNBF6 can also be further modified via exposure to acetyl sulfate, resulting in a proton-conducting ionomer film that has utility if proton transport to the carbon paper is desired.[1]

Growing pNBF6 from NPGL, we were able to control the thickness and uniformity of the pNBF6 coatings by varying the monomer concentration during film growth. NBF6 concentration ranging from 25-100 mM resulted in conformal growth throughout the nanoporous network, whereas NBF6 concentrations ≥ 150 mM resulted in capping of the porous network. Electrochemical impedance spectroscopy and scanning electron microscopy were used to characterize the uniformity and extent of films within the nanoporous architecture. Purely capacitive behavior was observed for films grown in 150 mM NBF6, suggesting that no redox probes were able to reach the NPGL surface during the experiment, whereas two time constant and Randle's circuit models were used to fit the remaining spectra. The size of the pores throughout the NPGL electrode impacts pNBF6 film growth and can inhibit conformal coating within the pores if too small. pNBF6-coated NPGL electrodes exhibit hydrophobic and oleophobic surface properties and provide effective barriers against the diffusion of aqueous ions.

The work described here presents enabling technologies that may have applications in the development of alternative energy sources. The PSI films have incredible reducing power that can be used in biocatalysis. The pNBFn polymer films can be applied as dielectrics, water- and oil-repellent coatings, and membranes films.

Upon sulfonating these films, the barrier properties changing dramatically, enabling the transport of protons and other ionic species through the film.

Future Work

Fabrication of a PSI-Electrochemical Cell

After gaining fundamental insight on the assembly and performance of PSI films, a progressive step would be to fabricate and test PSI photoelectrochemical proto-type cells. As depicted in Figure 10.1, a PSI electrochemical cell is comprised of a dense PSI film is assembled onto a gold cathode that is opposite a transparent indium tin oxide (ITO)-coated glass anode. A thin layer of dielectric, such as polystyrene (PS), will be used as an insulating layer to separate the gold and ITO electrodes. To prepare such a prototype cell, we will first prepare the PS layer via drop-casting or spin-coating the polymer around the perimeter of a mask as reported by Stange et al.[2] The low energy surfaces created by the PS coatings will prevent PSI deposition and enable us to selectively deposit the PSI onto hydrophilic surfaces such as –OH, -CO_2H, -NH_2, -NHS, and –TPDA terminated SAMs that were previously masked areas of the surface, Figure 10.1.[3, 4] We will then assemble a PSI film using vacuum assembly. During the PSI assembly, we will employ a hydrophobic mediator such as DCIP, which will partition from solution into the PSI film. A thin layer of polymer gel electrolyte will be deposited atop the PSI-filled cathode. We will use polymer gel electrolytes previously used in dye-sensitized Gratzel cells.[5] Polymer gels like poly(vinylidenefluoride-co-hexafluoroproylene) (PVdF-HFP), polyacrylonitrile, and polymethylmethacrylate

enhance the stabilities and lifetimes of the photoelectrochemical cells while maintaining high ionic conductivities ($>10^{-3}$ S/cm)[6] and diffusion coefficients similar to aqueous electrolytes. We will investigate transparent ITO-coated glass as the anode to complete the structure. Stacks of these structures can be created to multiply the current, as long as light can penetrate through the entire stack. We have estimated that a dense 7 μm film of PSI would block out all light, so as long as the combined thicknesses of the PSI/cathodes are below a few micrometers, stacked structures are viable to multiply current.

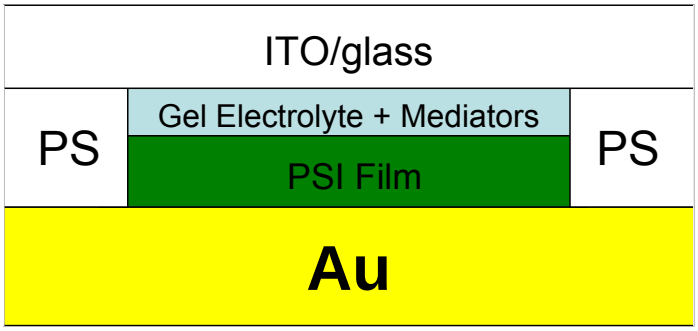

Figure 10.1. Proposed architecture of a PSI photo-electrochemical cell.

Integration of Pt-Catalyst within 3-D supports

As an extension of the proof-of-concept principles demonstrated in Chapter VII and the ability to grow pNBFn films from carbon paper and NPGL electrode supports in Chapters VIII and IX, we can combine these ionomer films with Pt-catalyst within the 3-D porous supports. Figure 10.2 displays a schematic of a prototype cathode assembly. Combining this electrode with a proton exchange membrane, such as Nafion®, would enable the testing of an entire membrane electrode assembly. The use of a bulk membrane is motivated to assess any impedance to proton transfer from the membrane to the porous electrode and the role of interfacial ionomer in facilitating this transfer. We can vary average pore size and porosity of the NPGL electrode, in addition to the

ionomer composition (pNBFn vs. pNBFHn) and thickness to investigate these pertinent interfacial effects on the oxygen reduction reaction and on the overall impedance of the system. Direct incorporation of Pt-catalyst and ionomer onto a carbon paper electrode would provide insight into the interfacial transport properties of the ionomer films as well. Such information could be used to molecularly optimize the interfacial environment within these 3-D electrodes and provide guidelines for the molecular design of interfaces for other geometries and types of fuel cells.

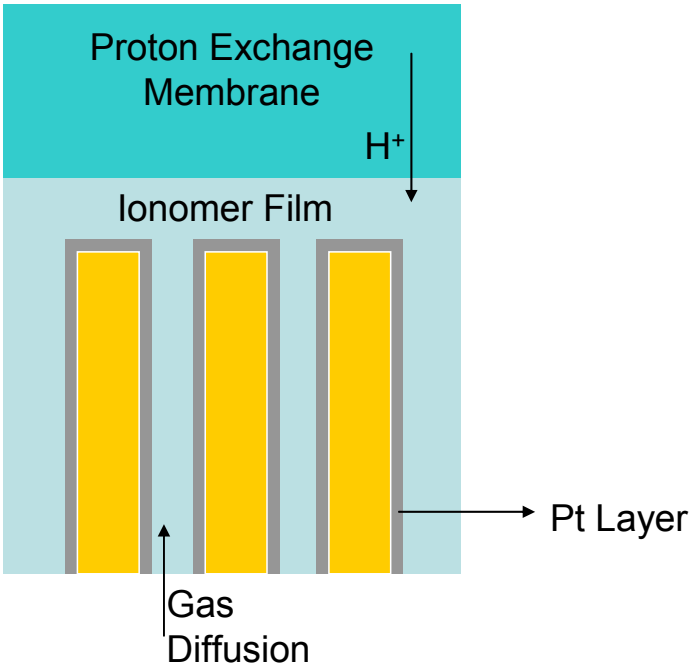

Figure 10.2. Schematic of a membrane electrode assembly using NPGL as a high surface area electrode modified with Pt layers.

References

1. Berron, B.; Faulkner, C. J.; Fischer, R. E.; Payne, P. A.; Jennings, G. K., Surface-Initiated Growth of Ionomer Films from Pt-Modified Gold Electrodes. *Langmuir* **2009**.

2. Stange, T. G.; Mathew, R.; Evans, D. F.; Hendrickson, W. A., STM and AFM of PS Spin-Coated Si Surfaces. *Langmuir* **1992,** 8, 920-926.

3. Ko, B. S.; Babcock, B.; Jennings, G. K.; Tilden, S. G.; Peterson, R. R.; Cliffel, D., Effect of Surface Composition on the Adsorption of Photosystem I onto Alkanethiolate Self-Assembled Monolayers on Gold. *Langmuir* **2004,** 20, (10), 4033-4038.

4. Lee, I.; Lee, J. W.; Greenbaum, E., Biomolecular Electronics: Vectorial Arrays of Photosynthetic Reation Centers. *Phys. Rev. Lett.* **1997,** 79, 3294-3297.

5. Wang, P.; Zakeeruddin, S. M.; Moser, J. E.; Nazeeruddin, M. K.; Sekiguchi, T.; Graetzel, M., A Stable Quasi-solid-state Dye-sensitized Solar Cell with an Amphiphilic Ruthenium Sensitizer and Polymer Gel Electrolyte. *Nature Materials* **2003,** 2, 402-407.

6. Kim, D.-W.; Jeong, Y.-B.; Kim, S.-H.; Lee, D.-Y.; Song, J.-S., Photovoltaic Performance of Dye-Sensitized Solar Cell Assembled with Gel Polymer Electrolyte. *Journal of Power Sources* **2005,** 149, 112-116.